

**Aerosol Jet Printed Devices and Logic Gates for Biosensing Applications**

by

Paul Lavryshyn

A thesis submitted in partial fulfillment of the requirements for the degree of

Master of Science

in

Solid State Electronics

Department of Electrical and Computer Engineering  
University of Alberta

© Paul Lavryshyn, 2023

# Abstract

Flexible electronics in recent years have gained attention due to their application in the medical and biosensing industries. The biosensor market in particular has been expanding significantly, with its market value expected to double by 2028 [1]. Electronic sensors have been widely used as biosensors due to their easy compatibility and interfaceability with electronic measurement and display systems. With the development of flexible electronics, wearable electronics have been demonstrated in the literature as well as sold commercially [2, 3].

This work focuses on building flexible electronic devices using a 3D printing technique known as aerosol jet printing. Both passive and active sensors are demonstrated. The active sensors are based on organic electrochemical transistor (OECT) devices, which are the main electronic devices in this work. Due to the inclusion of an organic semiconductor as part of their structure, these devices are able to be aerosol jet printed, enabling rapid changes to their geometry and characteristics. OECTs also operate at low voltages, compatible with aqueous environments, and are built using biocompatible materials, making them ideal for biosensing applications.

First, a passive temperature sensor is fabricated using a combination of aerosol jet printing and drop-casting techniques. The electrodes as well as a polyimide well to contain the drop-casted sensing material for the sensors are 3D printed. A nanocomposite dispersion of multi-walled carbon nanotubes and a thermoplastic is used as the sensing material. The sensor was found to have a maximum sensitivity of  $237 \Omega/^{\circ}\text{C}$ , with a negative temperature coefficient of  $-0.00134 \text{ K}^{-1}$ , while also displaying extremely high linearity in the range of 20 to  $55^{\circ}\text{C}$ . The device was also tested on

skin to verify correct operation as a biosensor.

Development of logic gate sensors is outlined as well as individual characterization of high-performance PEDOT:PSS-based OECTs. Devices are found to be extremely sensitive with a maximum transconductance value of 117 mS, currently the highest reported value for a planar OECT at the time of writing. Ion sensing, glucose sensing, and the effect of hydrogel treatment on device performance are also explored. The maximum sensitivity reported is 570 mV/dec when sensing NaCl concentration in the range of 1-10 mM, a value nearly 10x higher than the theoretical Nernst limit.

Finally, complimentary logic gates are fabricated using a combination of PEDOT:PSS and gNDI-Br<sub>2</sub> as channel materials. Individual characterizations of each device are outlined as well as the logical operation of the completed NOT gate.

In summary, all devices were fabricated using aerosol jet 3D printing, which was verified as an effective and, in some cases, preferred method of fabrication for specific applications. The devices shown are suitable for sensing temperature, ions, and glucose in a variety of different media such as skin, sweat, saliva, and blood measurements. The fabrication method has also shown to be capable of printing digital logic circuits that may allow for interfacing of the various biosensors outlined in this work.

# Preface

This thesis is the original work of Paul Lavryshyn carried out at the University of Alberta between September 2021 and August 2023. Dr. Manisha Gupta conceptualized the research and initial methodology.

In Chapter 3, all fabrication and characterization work was carried out by Paul Lavryshyn.

In Chapter 4, all fabrication and characterization work was carried out by Paul Lavryshyn. The creation of the PEDOT:PSS recipe present in this chapter as well as in Appendix A.2 was carried out by Jiaxin Fan, as well as creation of the glucose functionalization procedure which is also featured in Appendix A.3. Both procedures were slightly edited by Paul Lavryshyn and Yuchen Shao in order to suit the devices in this chapter. The characterization and optimization of the printing parameters of the polyimide ink present in this chapter as well as in Appendix B.2 was carried out by Paul Lavryshyn and Yuchen Shao.

In Chapter 5, all fabrication and characterization work was carried out by Paul Lavryshyn. The synthesis of the gNDI-Br<sub>2</sub> compound and synthesis and development of the gNDI-Br<sub>2</sub> ink recipe present in this chapter as well as in Appendix A.4 were carried out by Seongdae Kang.

In the Appendices, all work in Sections A.1, A.5, C.1 and C.2 is the original work of Paul Lavryshyn.

# Acknowledgements

First and foremost, I'd like to thank Dr. Manisha Gupta for giving me the opportunity to work in her lab over the last two years. She, along with the rest of the research group members were extremely supportive and I can't thank them enough. I'd like to especially thank Jiaxin Fan for mentoring me over the course of the first year of my program and setting me up for success the rest of the way. Many thanks to all my labmates, Yuchen Shao, Michelle Livojevic, Seongdae Kang, Anoushka Ganguli, Wael Zahr, and yes, even the weird 2D materials people: Andres Alejandro Forero Pico, Junsen Gao, Jyoti Yadav, and Dipanjan Nandi.

I'd like to thank my friends and family for supporting me, especially when I'd be in a foul mood due to my experiments not working out. None of this would have been possible without your support.

I would also like to acknowledge the financial support I've received from various funding agencies. I was fortunate enough to be awarded the Alberta Innovates Graduate Student Scholarship from the Government of Alberta as well as the Alberta Graduate Excellence Scholarship from the University of Alberta. I was also awarded coverage for fabrication and characterization costs through the CMC Microsystems MNT Award. These awards allowed me to more easily conduct the research and relieved mountains of stress, for which I am grateful.

# Table of Contents

<b>1</b>	<b>Introduction</b>	<b>1</b>
1.1	Biosensor Motivations . . . . .	1
1.2	Thesis Objectives . . . . .	5
1.3	Thesis Outline . . . . .	6
<b>2</b>	<b>Background</b>	<b>8</b>
2.1	Organic Semiconductors . . . . .	8
2.1.1	Conduction Mechanism . . . . .	9
2.1.2	Types of Organic Semiconductors . . . . .	13
2.2	Organic Electrochemical Transistors (OECTs) . . . . .	15
2.2.1	Operating Principle . . . . .	16
2.2.2	OECT Materials . . . . .	20
2.2.3	PEDOT:PSS . . . . .	25
2.2.4	gNDI-Br <sub>2</sub> . . . . .	26
2.3	Carbon Nanotubes (CNTs) . . . . .	28
2.3.1	CNT Structure and Properties . . . . .	28
2.3.2	CNT Applications . . . . .	30
2.4	Logic Gates . . . . .	32
2.4.1	Circuit Theory . . . . .	32
2.4.2	Common Uses . . . . .	36
2.5	Fabrication Techniques . . . . .	37
2.5.1	Fabrication Techniques for Organic Semiconductors . . . . .	37
2.5.2	Aerosol Jet 3D Printing . . . . .	38
2.6	Characterization Techniques . . . . .	41
2.6.1	Profilometry . . . . .	41
2.6.2	4-Point Probe . . . . .	42
2.6.3	UV-Vis Spectrophotometry . . . . .	42
2.6.4	Thermogravimetric Analysis . . . . .	43
2.6.5	Scanning Electron Microscope . . . . .	44

2.6.6	Keithley Sourcemeter . . . . .	44
2.7	Hydrogels . . . . .	45
<b>3</b>	<b>Aerosol Jet 3D-Printed Temperature Sensor Based on Multi-Walled Carbon Nanotubes</b>	<b>47</b>
3.1	Introduction . . . . .	47
3.2	Materials and Methods . . . . .	50
3.2.1	Aerosol Jet Printing . . . . .	51
3.2.2	Nanocomposite Dispersion Preparation . . . . .	51
3.2.3	Material and Electrical Characterization . . . . .	52
3.3	Results and Discussion . . . . .	53
3.3.1	Nanocomposite Weight Ratio Optimization . . . . .	53
3.3.2	Nanocomposite Film Characterization . . . . .	60
3.3.3	Skin Temperature Measurement . . . . .	63
3.3.4	Mouse Testing . . . . .	67
3.4	Conclusion . . . . .	68
<b>4</b>	<b>Aerosol Jet 3D-Printed Depletion Mode Logic Gates for Ion Sensing</b>	<b>70</b>
4.1	Introduction . . . . .	70
4.2	Materials and Methods . . . . .	72
4.2.1	Material Preparation . . . . .	72
4.2.2	Aerosol Jet Printing . . . . .	73
4.2.3	Material and Electrical Characterization . . . . .	74
4.3	Logic Gate Theory, Circuit, and Design . . . . .	75
4.3.1	Depletion-mode NOT Gate Operating Principle . . . . .	75
4.3.2	Glucose Sensing Mechanism . . . . .	79
4.4	Results and Discussion . . . . .	82
4.4.1	Individual OECT Characterization . . . . .	82
4.4.2	Ion Sensing Results . . . . .	85
4.4.3	Hydrogel Treatment Results . . . . .	90
4.4.4	Glucose Sensing Results . . . . .	93
4.5	Conclusion . . . . .	96
<b>5</b>	<b>Complementary NOT Gate Based on Aerosol Jet 3D-Printed Organic Electrochemical Transistors</b>	<b>98</b>
5.1	Introduction . . . . .	98
5.2	Materials and Methods . . . . .	100
5.2.1	Material Preparation . . . . .	100

5.2.2	Aerosol Jet Printing . . . . .	100
5.2.3	Electrical Characterization . . . . .	101
5.3	Logic Gate Theory, Circuit, and Design . . . . .	101
5.4	Results and Discussion . . . . .	104
5.4.1	Individual OECT Characterization . . . . .	104
5.4.2	NOT Gate Performance . . . . .	106
5.4.3	Future Optimizations . . . . .	108
5.5	Conclusion . . . . .	109
<b>6</b>	<b>Conclusion</b>	<b>111</b>
6.1	Summary . . . . .	111
6.2	Future Work . . . . .	114
6.2.1	Temperature Sensor . . . . .	114
6.2.2	Depletion-mode Logic Gates . . . . .	114
6.2.3	Complimentary Logic Gates . . . . .	115
6.2.4	Biosensing Platform . . . . .	115
	<b>Bibliography</b>	<b>117</b>
	<b>Appendix A: Recipes and Procedures</b>	<b>131</b>
A.1	Nanocomposite Recipe and Preparation Procedure . . . . .	131
A.2	PEDOT:PSS Ink Recipe and Preparation Procedure . . . . .	132
A.3	gNDI-Br <sub>2</sub> Ink Recipe and Preparation Procedure . . . . .	133
A.4	GOx Functionalization Procedure . . . . .	134
A.5	Short Channel Printing Procedure . . . . .	135
	<b>Appendix B: Ink Characterization</b>	<b>138</b>
B.1	PEDOT:PSS Ink Characterization . . . . .	138
B.2	Polyimide Ink Characterization . . . . .	138
	<b>Appendix C: Ion-Selective Membrane</b>	<b>141</b>
C.1	Recipes and Procedure . . . . .	141
C.2	Results . . . . .	142

# List of Tables

4.1	Summary of sensitivity results for various sensing parameters using a PEDOT:PSS based depletion mode logic inverter. . . . .	97
A.1	Ingredient ratios for the two recipes A and B found in chapters 4 and 5, respectively. Recipe A results in a PEDOT:PSS film with a higher conductivity while recipe B results in a film with lower conductivity. .	133
B.1	The relationship between number of printed layers, thickness, and resistance of printed PEDOT:PSS films. . . . .	138
B.2	The relationship between printed layers and thickness of polyimide films.	138
B.3	Optimized parameters for polyimide ink printing. . . . .	139
C.1	The multiple recipes attempted for the development of an ion-selective membrane. . . . .	142

# List of Figures

1.1	The multiple stages of a biosensor . . . . .	2
2.1	The electronic configuration of ethene resulting in $sp^2$ hybridization. .	10
2.2	(a) HOMO and LUMO levels of ethene, showcasing the $\pi$ bonds and antibonds. (b) Orbital structure of ethene, showing the lone $\pi$ orbital in the vertical axis (from the $2p_z$ orbital) and the $\sigma$ orbitals in the horizontal plane (from the three $sp^2$ orbitals). . . . .	11
2.3	Cross-section of a typical OEET with a test probe used as a gate. The gate voltage is positive and the drain voltage is negative, consistent with a p-type depletion mode device. . . . .	16
2.4	(a) The ionic circuit model of an OEET gate-electrolyte-channel interface. $Q(x)$ indicates the movement of ions through the equivalent series resistance and capacitances. (b) Potential profile of an OEET gate-electrolyte-channel interface. Polarizable materials such as Au induce a larger voltage drop across the gate-electrolyte interface than non-polarizable materials. . . . .	21
2.5	Top-down view of an OEET with a planar gate. The electrolyte is dropped over top of a planar square that is then contacted with a test probe. . . . .	22
2.6	(a) Chemical structure of PEDOT:PSS. (b) Visual representation of interaction between PEDOT and PSS. . . . .	26
2.7	Chemical structure of gNDI-Br <sub>2</sub> . . . . .	27
2.8	(a) The structure of graphene. (b) The structure of various carbon nanotubes. From left to right: single-walled nanotube with configuration (5,5) armchair, multi-walled nanotube (2 walls) with configuration (5,5) armchair, single-walled nanotube with configuration (9,0) zigzag. . . . .	29
2.9	(a) Logic symbol, characteristic equation, and truth table for a NOT gate. (b) Electronic complementary circuit implementation of a NOT gate. . . . .	33

2.10	(a) Switch-level representation of a NOT gate with $V_{in}$ of logic 0. (b) Switch-level representation of a NOT gate with $V_{in}$ of logic 1. (c) The transfer curve of a NOT Gate. . . . .	35
2.11	Integration of logic circuits in high-end computing applications. . . .	37
2.12	Schematic diagram of aerosol flow, gas flow, and deposition in aerosol jet printing. . . . .	39
2.13	The Optomec Aerosol Jet 5X printing system. . . . .	40
3.1	Resistivity of a percolating network versus the concentration of the filler material. As the concentration increases, nodes of the material – in this case carbon nanotubes – begins to form conductive pathways, resulting in a sharp increase in conductivity and decrease in resistivity.	49
3.2	(a) The finished flexible sensor inserted in the PCB connector board via ZIF connectors. (b) (Top) 2D view and dimensions of the 3D printed and drop casted sensor on polyimide substrate. (Bottom) 2D view and dimensions of the connector board. . . . .	50
3.3	FESEM images of the nanocomposite with 10 $\mu\text{m}$ nanotubes at SEBS:MWCNT ratios of (a) 4:1 (b) 5:1 (c) 10:1 (d) 15:1. (e) The relationship between nanocomposite weight ratio and initial resistance and sensitivity. . . .	54
3.4	FESEM images of the nanocomposite with 10 $\mu\text{m}$ nanotubes at a SEBS:MWCNT ratio of 5:1 at (a) x20k magnification and (c) x45k magnification. For comparison, 1.5 $\mu\text{m}$ nanotubes at a SEBS:MWCNT ratio of 5:1 are shown at (b) x20k magnification and (d) x45k magnification. . . . .	57
3.5	Resistance response of an optimized sensor (15:1 nanocomposite ratio) in a controlled environment (hot plate, no movement). The grey line indicates the resistance of the device when the temperature was increased, while the red line indicates the resistance when the temperature was decreased. . . . .	60
3.6	(a) Nanocomposite drop-casts of varying volumes on 5 mil Kapton with a pronounced coffee ring.(b) UV-vis spectra of nanocomposite dropped on glass wafer at various positions of the wafer. The area of the glass wafer from which the nanocomposite sample was taken is indicated by the inside of the circle in (d). (c) Thermogravimetric analysis of the nanocomposite dropped on glass wafer was conducted with the results. (d) The positions (1-4) at which the UV-vis spectra were measured.	62

3.7	(a) The results of the skin temperature measurement. The first and last points are taken roughly 30 seconds before and after the 30-minute-long skin test and indicate the resistance of the device in the ambient room temperature (off-skin). (b) An encapsulated device with a comparatively opaquer circular area at the top sensing area of the device.	64
3.8	The skin temperature repeatability test. The higher points correspond to the sensor reading in ambient air, while the low points correspond to the reading when the sensor was placed on skin. . . . .	65
3.9	Resistance response of a sensor pre and post-encapsulation. The sensitivity has dropped from $237 \Omega/^{\circ}\text{C}$ to $72 \Omega/^{\circ}\text{C}$ , corresponding with a decrease in initial, room-temperature resistance. . . . .	67
3.10	Skin temperature measurements for both a (a) healthy and (b) diabetic mouse. The first and last points are taken roughly 30 seconds before and after the 30-minute-long test and indicate the resistance of the device in the ambient room temperature (off-mouse). . . . .	68
4.1	(a) Circuit schematic of the depletion mode NOT gate. (b) Cross section of a 3D printed OECT device. Not pictured: the in-plane gold gate that would be found in plane with the Au contact but behind the cross section (looking into the page). (c) 2D top-down view of the layout of the NOT gate circuit. . . . .	76
4.2	(a) Resistance representation of the depletion-mode NOT gate with $V_{\text{in}}$ of logical 0. (b) Resistance representation of the depletion-mode gate with $V_{\text{in}}$ of logical 1. (c) The transfer curve of the depletion-mode NOT Gate. . . . .	78
4.3	(a) A hydrogel-treated Q1 of a NOT gate device under test. (b) Q1 of a NOT gate device functionalized with GOx, nafion, and a protective hydrogel of 1xPBS. (c) Fabricated NOT gates printed on 2 mil polyimide substrate without hydrogel treatment or glucose functionalization. (d) Standard testing setup of printed NOT gates with liquid electrolyte dropped on the channels. . . . .	81
4.4	(a) $I_{\text{D}}-V_{\text{D}}$ curves of Q1 of a NOT gate. (b) $I_{\text{D}}-V_{\text{D}}$ curves of Q2 of a NOT gate. . . . .	83
4.5	(a) $I_{\text{D}}-V_{\text{G}}$ and $g_{\text{m}}$ curves of Q1 of a NOT gate. (b) $I_{\text{D}}-V_{\text{G}}$ and $g_{\text{m}}$ curves of Q2 of a NOT gate. . . . .	84
4.6	$\sqrt{I_{\text{D}}}-V_{\text{G}}$ curves indicating the equations for voltage threshold extraction (in blue) for (a) Q1 and (b) Q2 of a NOT gate. . . . .	85

4.7	NOT gate sweeps with a varying NaCl concentration for devices with (a) 2 printed PEDOT layers ( $\sim 250\text{nm}$ ) and (b) 10 printed PEDOT layers ( $\sim 1.25\mu\text{m}$ ).	86
4.8	$I_D$ - $V_D$ curves for (a) thinner ( $\sim 250\text{nm}$ ) channel devices and (b) thicker ( $\sim 1.25\mu\text{m}$ ) channel devices.	86
4.9	Switching voltage vs NaCl concentration curves for (a) thinner ( $\sim 250\text{nm}$ ) channel devices and (b) thicker ( $\sim 1.25\mu\text{m}$ ) channel devices.	87
4.10	NOT gate sweeps with varying concentrations of (a) NaCl, (b) $\text{CaCl}_2$ , (c) KCl, and (d) $\text{MgCl}_2$ .	88
4.11	Sensitivity curves for devices tested with (a) NaCl, (b) $\text{CaCl}_2$ , (c) KCl, and (d) $\text{MgCl}_2$ .	89
4.12	$I_D$ - $V_D$ curves for devices (a) pre-hydrogel treatment and (b) post-hydrogel treatment. $I_D$ - $V_G$ and transconductance curves for devices (c) pre-hydrogel treatment and (d) post-hydrogel treatment.	91
4.13	NOT gate sweeps of an inverter device with NaCl (a) pre-hydrogel treatment and (b) post-hydrogel treatment. Sensitivity curves for NaCl solution for an inverter device (c) pre-hydrogel treatment and (d) post-hydrogel treatment.	93
4.14	$I_D$ - $V_D$ curves for device Q1 with (a) 100 mM glucose and (b) 100 mM NaCl. $I_D$ - $V_G$ and $g_m$ curves for device Q1 with (c) 100 mM glucose and (d) 100 mM NaCl. Voltage extraction demonstrated for device Q1 with (e) 100 mM glucose and (f) 100 mM NaCl.	94
4.15	(a) NOT gate sweeps of a glucose-functionalized inverter device with varying glucose concentration. (b) Sensitivity curve of a glucose-functionalized inverter device.	96
5.1	(a) Circuit schematic of the complementary organic NOT gate. (b) Cross section of the 3D printed inverter. Not pictured: the in-plane gold gates that would be found in plane with the Au contact but behind the cross section (looking into the page). (c) 2D top-down view of the layout of the complementary organic NOT gate circuit.	102
5.2	(a) Photograph of the printed complementary inverter with NDI channel under test. (b) Microscope image of PEDOT:PSS channel with width measured. (c) Microscope image of gNDI- $\text{Br}_2$ channel with length measured.	103
5.3	$I_D$ - $V_D$ curves of printed (a) PEDOT:PSS and (b) gNDI- $\text{Br}_2$ devices.	104

5.4	$I_D$ - $V_G$ and transconductance curves of printed (a) PEDOT:PSS and (b) gNDI-Br <sub>2</sub> devices. . . . .	105
5.5	$I_D$ - $V_G$ curves and voltage extraction of printed (a) PEDOT:PSS and (b) gNDI-Br <sub>2</sub> devices. . . . .	106
5.6	NOT gate sweep of the printed complementary gate. . . . .	107
A.1	Printing design for a channel with gold electrodes. The design has resulted in a printed channel with minimum feature size of 22 $\mu\text{m}$ . The channel length measured in the middle indicates 50 $\mu\text{m}$ . . . . .	137
B.1	FTIR curves of printed polyimide films after annealing at various temperatures for 1 hour and 30 minutes. . . . .	140
C.1	(a) $I_D$ - $V_D$ curves of a regular OECT with NaCl dropped on its channel. (b) $I_D$ - $V_D$ curves of the same OECT with an Na+ ISM dropped over its channel, with NaCl as the electrolyte. (c) $I_D$ - $V_D$ curves of the same OECT with an ISM dropped over its channel, with KCl as the electrolyte. 143	

# Abbreviations

**4PP** 4-point probe.

**AFM** Atomic force microscopy.

**Alq3** Tris(8-hydroxyquinoline)aluminum(III).

**BBL** Poly(benzimidazobenzophenanthroline).

**CHIT** Chitosan.

**CMOS** Complimentary metal-oxide-semiconductor.

**CNT** Carbon nanotube.

**DBSA** dodecylbenzene sulfonic acid.

**DPP-DTT** Poly[3,6-bis(5-thiophen-2-yl)-2,5-bis(2-octyldodecyl)pyrrolo[3,4-c]  
-pyrrole1,4(2H,5H)-dione-2,2'-diyl-alt-thieno[3,2-b]thiophen-2,5-diyl].

**DTBDT-C6** dithieno[2,3-d;2',3'-d']benzo[1,2-b;4,5-b']dithiophene.

**EG** Ethylene glycol.

**FET** Field-effect transistor.

**FFC** Flat-flex cable.

**FTIR** Fourier Transform Infrared.

**GND** Ground.

**GOPS** (3-glycidyloxypropyl) trimethoxysilane.

**GOx** Glucose oxidase.

**HOMO** Highest occupied molecular orbital.

**IoT** Internet of Things.

**ISFET** Ion-sensitive field-effect transistor.

**LUMO** Lowest unoccupied molecular orbital.

**MOSFET** Metal-oxide-semiconductor field-effect transistor.

**MWCNT** Multi-walled carbon nanotube.

**NDI** naphthalenediimide.

**NTC** Negative temperature coefficient.

**OEET** Organic electrochemical transistor.

**OFET** Organic field-effect transistor.

**OLED** Organic light-emitting diode.

**OMIEC** Organic mixed ionic-electronic conductor.

**OPV** Organic photovoltaic.

**OSC** Organic semiconductor.

**OTFT** Organic thin-film transistor.

**p(G2T-TT)** poly(2-(3,3'-bis(2-(2-(2-methoxyethoxy)ethoxy)ethoxy)-[2,2'-bithiophen]-5-yl)thieno[3,2-b]thiophene).

**p(gNDI-T2)** thiophene-2,6-dibromonaphthalene-1,4,5,8-tetracarboxylic diimide.

**P3HT** Poly(3-hexylthiophene).

**PANI** Polyaniline.

**PBS** Phosphate buffer solution.

**PCB** Printed circuit board.

**PDN** Pull-down network.

**PDPP3T** poly[2,5-bis(2-hexyldecyl)-2,3,5,6-tetrahydro-3,6-dioxopyrrolo  
-[3,4-c]pyrrole-1,4-diyl- alt -[2,2':5',2''-terthiophene]-5,5''-diyl.

**PEDOT:PSS** poly(3,4-ethylenedioxythiophene) polystyrene sulfonate.

**PEEK** Poly ether ether ketone.

**PEG** poly(ethylene glycol).

**PET** polyethylene terephthalate.

**PI** Polyimide.

**PLQY** Photoluminescence quantum yield.

**PPy** Polypyrrole.

**PUN** Pull-up network.

**PVA** poly(vinyl alcohol).

**RTL** Register transfer level.

**SEBS** poly(styrene-b-(ethylene-co-butylene)-b-styrene).

**SEM** Scanning electron microscope.

**SWCNT** Single-walled carbon nanotube.

**TGA** Thermogravimetric analysis.

**UV-Vis** Ultraviolet-visible.

**ZIF** Zero-insertion force.

# Chapter 1

## Introduction

### 1.1 Biosensor Motivations

Biosensors are an invaluable tool in the medical industry which can improve diagnostic accuracy and quality of life. However, due to their interdisciplinary nature, it is difficult to produce biosensing devices that meet multiple crucial criteria [2]. These include, but are not limited to, accuracy, robustness, reproducibility, repeatability, ease of fabrication, accuracy, and comfort. This thesis includes multiple biosensing devices and will analyze these characteristics for each device. Biosensing is a popular topic in academia due to the need for optimization of these numerous aspects. It also requires a wide area of expertise due to the multiple stages involved in a typical biosensor. As illustrated in Figure 1.1, a biosensor must have some kind of analyte to target - this requires specialized knowledge of how to optimally collect this analyte, the typical concentration of the analyte in the medium collected (and thus the limit of detection requirements), and how the information collected can be useful. Next, a biosensor must have a bioreceptor that directly interacts with the analyte to make it suitable for transducer stage, which involves conversion of the biological or chemical signal to a usable electrical signal. Finally, there is a signal processing stage, which involves circuit components and data processing to ensure readable and accurate data. To design a robust biosensor that can encompass all these components, a wide range of knowledge is required that includes biology, biochemistry, materials and electrical

engineering. This thesis will mainly focus on the latter two biosensor stages which draws mostly on electrical engineering knowledge, but will also reference the first two stages since full biosensor devices were developed.

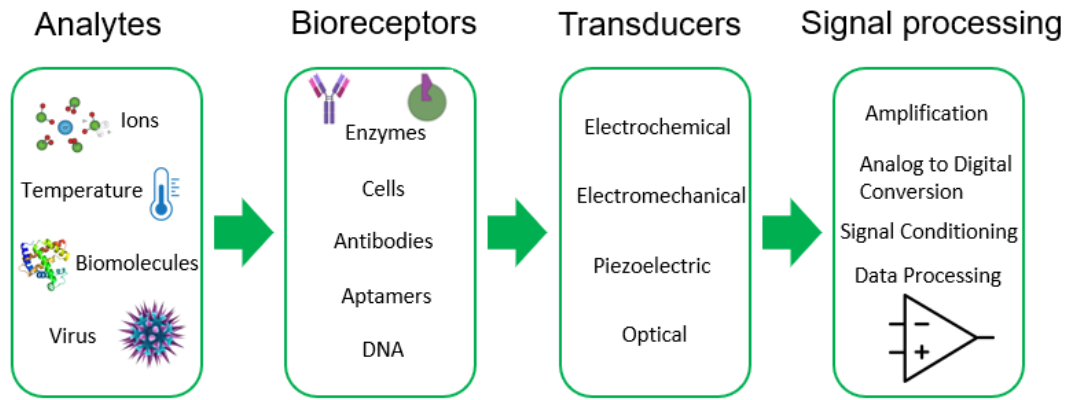


Figure 1.1: The multiple stages of a biosensor

In any sensor, the final readout is always an electrical signal [3]. Regardless of whether a device is optical, thermal, piezoelectric, or electrochemical in nature, the signal is always, in one way or another, converted to an electrical signal for readout electronics or data processing. Because of this, it is extremely convenient to directly use sensors that can easily interface with the readout electronics, such as electrochemical, piezoelectric, or potentiometric sensors [4, 5]. Other biosensor types, such as an optical sensor, may require larger systems and cannot process analytes while collecting them (i.e, Raman spectroscopy and Fourier Transform Infrared (FTIR) spectroscopy based systems) [6, 7]. This thesis will feature both passive and active electronic sensors that can be directly plugged into measurement circuits while simultaneously measuring an analyte on skin. The ability to directly place a biosensor on skin to collect an analyte is a desirable quality in a biosensor - skin sensing is non invasive and allows the collection of body fluids for used for sensing such as sweat and blood.

To achieve this kind of biosensor, flexible electronics have become increasingly

popular [8, 9]. From a consumer standpoint, wearable electronics have become commonplace with the emergence of devices such as smartwatches and smart glasses. From a research standpoint, the effort to optimize the integration of electronic devices such as transistors on flexible substrates has been well documented [10–12]. However, traditional transistors are inorganic, with the vast majority using silicon as the main semiconducting material. Inorganic semiconductors exhibit much higher crystallinity and carrier mobility than their organic counterparts, at the expense of rigidity, making them unsuitable for flexible devices [13]. This work will focus on organic semiconductors and highlight their advantages over inorganic semiconductors for biosensing applications, as well as their limitations. Regardless of the type of semiconductor used, however, the general operating principle of a transistor remains the same. Field-effect transistors (FETs) are 3 terminal devices in which the current between two of the terminals - the source and the drain - is controlled by the third terminal, called the gate. The most common example of this is the metal-oxide-semiconductor FET (MOSFET), which is inorganic. The organic counterparts to this device include organic field-effect transistors (OFETs), organic thin film transistors (OTFTs), and organic electrochemical transistors (OECTs) [14–16]. OECTs differ from OFETs and OTFTs in that they include an electrolyte as part of their structure. This makes them suitable for use in aqueous environments and for collecting analytes in aqueous media. OECTs also operate at much lower voltages than OFETs, making them ideal for miniaturization and signal processing. This work includes electronic circuits built using OECTs.

In general, OECT sensors are built using a single OECT transistor device, with the main analysis done through measurement of the current level through it. In recent years, there have been efforts to design OECT biosensing circuits that directly output a voltage rather than a current. One way to do this is through logic gates [17, 18]. Logic gates are electronic circuits that implement a boolean function - that is, they output a high or low voltage (a "1" or a "0") based on the input or specific combination

of inputs. Larger logic circuits are then created using logic gates, which implement a more complex logical function or algorithm. As multiple logic circuits are connected together, devices such as computer processors can be developed. However, logic gates have rarely been used for biosensing purposes [18]. The most simple logic gate is the NOT gate, also called an inverter, which takes a 1 or 0 at the input and outputs a 0 or 1, respectively. The ability for a sensing device to output a voltage rather than a current greatly reduces the signal conditioning requirements, which reduces the cost and footprint of the circuit. In this work, two different kinds of OECT NOT gates are designed, fabricated, and tested, each with their own advantages and disadvantages.

Another crucial difference between organic and inorganic semiconductors is in the fabrication method, which is a main focus in this thesis. Inorganic semiconductors generally use silicon as the channel material, which requires a complex process for fabricating transistors. A typical process flow for a MOSFET involves procurement of silicon wafers, oxide growth, lithography, etching, and pattern transfer steps, ion implantation, and metallization [19]. All this must occur in a controlled clean-room environment and incurs a high cost. An organic device, on the other hand, has a variety of options to choose from for deposition of the active channel material, such as spin-coating, screen-printing, and even simple drop-casting. Organic devices are inherently solution-processable and as a result have more flexibility with fabrication methods. Typically, a fabricated MOS device requires intricate design and layout of a photomask. Photomasks are placed on a substrate already covered in a photoresist and shield certain sections of the substrate from ultraviolet light. The photoresist is then developed and the pattern of the design is able to be transferred to the substrate through etching or lift-off. The photomask for this process is typically a chrome pattern-covered glass substrate and must be produced specifically for one design. This is because devices typically made using this process have extremely small features. For example, the smallest feature sizes in available commercial devices have reached 3 nm at the time of writing [20]. In contrast, organic devices that are used for

biosensing purposes do not need to be this small - in fact, it is counterproductive to use small channel sizes in these kinds of devices due to the need for a minimum number of functional groups per unit area. Because of this, finding cheaper alternatives to traditional device fabrication methods is highly desirable. In this work, aerosol jet 3D printing is used as a primary method of fabrication for the biosensors demonstrated. Instead of a photomask, a simple computer-aided design (CAD) file is required which may be edited freely without the need and cost of manufacturing the mask. 3D printing also allows for the deposition of multiple materials using the same method. This contrasts with traditional device fabrication, which requires different steps for channel material, electrodes, and gate dielectrics and adds complexity and cost to the final device [19]. The final designs included in this work are the result of hundreds of design changes that were only possible due to the low cost of aerosol jet printing. This demonstrates the high potential of 3D printing as a viable and affordable option for biosensor fabrication.

## 1.2 Thesis Objectives

The goal of this thesis is to build and optimize various biosensors using aerosol jet 3D printing with an emphasis on real-world application. To achieve this, OECTs are chosen as the main active sensor transducer due to their mechanical flexibility, low operating voltages, biocompatibility, and compatibility with aqueous environments [16]. Since a major focus of the thesis is realization of convenient and easy-to-use biosensors, OECTs are placed in a logic gate configuration to take advantage of simpler signal conditioning requirements. Much of the work is focused on optimizing logic gate operation through transistor matching, circuit configuration and channel material type, and the results are shown in the form of ion sensing performance and sensitivity. Additionally, a chapter is included which does not use OECTs as the main transducer, rather, carbon nanotubes (CNTs) are used in the form of a passive resistive temperature sensor. The work aims to demonstrate that all these biosensors

can be fabricated together using aerosol jet printing such that future work can focus on printing all these optimized sensors on one substrate to be interfaced with each other. To achieve this, various materials are tested, optimized, and used to build the sensors using primarily aerosol jet printing. Devices then need to be tested to ensure optimal biosensing performance. In an effort to optimize device performance, various device geometries need to be attempted which is made easier by the method of fabrication. The work also aims to demonstrate that aerosol jet printing is an excellent choice for organic semiconductor-based devices (biosensor or otherwise) and biosensors in general (non-OECT based passive sensors).

### **1.3 Thesis Outline**

This thesis includes 6 chapters which are outlined below.

Chapter 1 is a brief overview of the motivations of biosensors, the current problems and how this thesis addresses these through design and fabrication.

Chapter 2 is a background chapter which first addresses the theory and working principles of organic semiconductors and specifically OECTs. The structure, properties and applications of carbon nanotubes are then discussed. Although carbon nanotubes may be semiconducting in nature, they are purely used as resistive sensors in this work. A section on logic gate theory and common uses is included. Finally, fabrication and characterization techniques that are prevalent in this thesis are outlined.

Chapter 3 outlines the carbon nanotube-based resistive temperature sensor. Material selection, characterization, and optimization are demonstrated as well as sensor design, fabrication, and optimization. Heating tests are shown as well as skin temperature sensing.

Chapter 4 outlines logic gates made using a single p-type organic channel material in OECTs. Preparation of the semiconductor is shown as well as aerosol jet printing parameters. Design and layout of the logic gate circuit is outlined. Individual

transistor and circuit electrical measurements are made and analyzed for ion sensing performance. The effect of dropping a hydrogel on the devices is also explored. Functionalization of the OECT device for selective glucose testing is outlined with results demonstrated.

Chapter 5 outlines logic gates made using both a p-type and n-type material in OECTs. Preparation of the n-type semiconductor is shown in addition to the materials used in the previous chapter. Both types of transistors are characterized with differences outlined. The chapter is meant to outline the advantages of complementary logic gates and highlight the difficulty of achieving organic complementary gates.

Chapter 6 is the summary and conclusion, with future work outlined.

Appendix A shows the recipes and procedures for creation of the nanocomposite and PEDOT:PSS and NDI inks, and the procedure for the glucose functionalization of the OECT devices.

Appendix B shows the characterization data of the PEDOT:PSS and polyimide inks.

Appendix C outlines the results from the failed ion-selective membrane experiments along with the recipes used to obtain these results.

# Chapter 2

## Background

### 2.1 Organic Semiconductors

Organic semiconductors (OSCs) have gained many applications since their discovery in 1948 [21]. Organic light emitting diodes (OLEDs) are the most successful implementation of OSC technology and are commonly used in commercial high-resolution electronic displays due to their highly efficient luminescence [22]. Due to their high absorption coefficients, organic semiconductors have been used as an alternative to silicon in organic photovoltaic cells (OPVs) [23]. Organic Field-Effect Transistor (OFET) devices have also been developed [14]. A variation of the OFET called the organic electrochemical transistor (OECT) has gained popularity as an excellent option for biosensing, and is a major component of this thesis. In contrast with OLEDs and OPVs, organic transistor devices suffer from poorer performance than their inorganic counterparts in terms of traditional application (mobility, switching speed) [13]. The reason for this is outlined in this section with an explanation of the conduction mechanism and various types of organic semiconductor materials. Though organic FET-style devices are not close to the performance of heavily optimized modern metal-oxide-semiconductor FETs (MOSFETs), their solution-processability and ease of fabrication opens the door to various niche end uses such as biosensing.

### 2.1.1 Conduction Mechanism

To understand the differences in performance between organic and inorganic semiconductor devices, one must understand the differences in conduction mechanism, which arises from the structural differences. In an inorganic semiconductor structure, such as silicon, the well-ordered crystalline lattice allows for charge transport to occur in the form of band transport [24]. In such a lattice, a conduction and a valence band form due to the Pauli Exclusion Principle, which states that no two electrons in an atom can have the exact same quantum number [25]. This implies that only two electrons may occupy a single orbital, and they must have opposite spins. Thus, when atoms are brought close together, like in a crystalline lattice, the energy levels must be split in order to accommodate all the electrons. As a result, bands arise which dictate the conduction in the semiconductor based on the voltages applied, which bend the bands in various ways and allowing or blocking charge flow. The valence band is lower in energy and filled with electrons, while the conduction band is at a higher energy and generally unoccupied. Since the bands are continuous, current flows freely as long as the materials and their band levels are matched properly. Additionally, if a crystalline lattice has excess electrons, these make up the majority carriers for conduction and is known as n-type doping. In contrast, if it has excess holes, this is known as p-type doping. Being able to tune the conduction easily in this way is a major advantage of inorganic semiconductors.

The conduction mechanism for organic semiconductors, however, is known as hopping [24]. In contrast to band transport, it is inter-molecular and occurs due to molecular orbitals. When atomic orbitals are brought together, they can overlap and undergo a process called orbital hybridization and form molecular orbitals. The simplest and most common types of hybridization present in most molecules are categorized by the ways in which the s and p orbitals combine. These types are sp,  $sp^2$ , and  $sp^3$  hybridization, which correspond to linear, trigonal-planar, and tetra-

hedral configurations, respectively. For organic semiconductors,  $sp^2$  hybridization of the carbon chain is used to explain conduction. Here, ethene is used as an example of  $sp^2$  hybridization. As ethene has a ground state electronic configuration of  $1s^2 2s^2 2p^1 2p^1$ , it undergoes  $sp^2$  hybridization and forms 3  $sp^2$  orbitals with one unchanged  $2p_z$  orbital. This is illustrated in Figure 2.1. It is due to these  $2p_z$  orbitals that  $\pi$  and  $\pi^*$  orbitals (bonding and anti-bonding) are formed which make up the basis of conduction for organic materials.

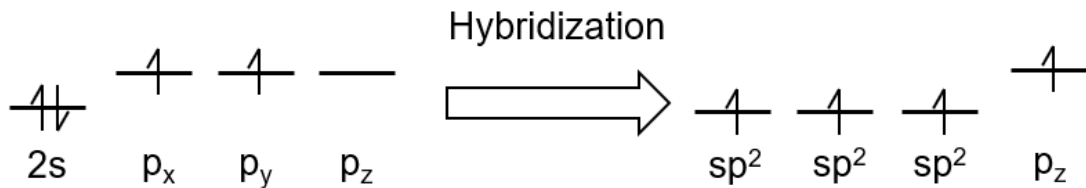


Figure 2.1: The electronic configuration of ethene resulting in  $sp^2$  hybridization.

The overlap of hybridized orbitals leads to the formation of strong  $\sigma$  bonds, while the unhybridized bonds lead to weaker  $\pi$  bonds. Both of these kind of bonds are covalent and describe the contribution of electronic structure to the conduction. If a molecule contains alternating single and double or triple bonds, the electrons from the  $\pi$  bonds are delocalized. This means that the electrons are shared over multiple atoms. This alternation is called conjugation and organic semiconductors that exhibit this are commonly referred to as  $\pi$ -conjugated polymers [26, 27]. The interactions between  $\pi$  bonds is called  $\pi$ - $\pi$  stacking and is an important measure of the charge transport properties. By modifying the  $\pi$ - $\pi$  stacking, the crystallinity, conductivity, and flexibility of the material can all be modified and tuned. In general, the more crystalline a material is, the higher its conductivity, but the lower the flexibility, so careful tradeoffs must be made according to application [24].

In general,  $\sigma$  bonds are strong enough that the electrons do not delocalize and thus do not contribute to conduction as much as  $\pi$  bonds [28]. This is due to the larger

energy gap between occupied bonding orbitals and unoccupied anti-bonding orbitals. As previously discussed, the unhybridized p orbitals overlap to form molecular orbitals - however, they may overlap in-phase or out-of-phase. In-phase overlapping leads to a regular  $\pi$  bond which is at a lower energy than a  $\pi^*$  anti-bond formed from out-of-phase overlapping. Analogously to the valence and conduction bands in inorganic semiconductors, the  $\pi$  and  $\pi^*$  are generally occupied and unoccupied, respectively. These are referred to as the highest occupied molecular orbital (HOMO) and lowest unoccupied molecular orbital (LUMO). Figure 2.2 shows the HOMO and LUMO levels of ethene as well as the bonding and anti-bonding combinations of the  $\pi$  orbital. As the number of atoms in the molecule increases, the number of bonding and anti-bonding interactions increases as well. The filling of these orbitals with electrons dictates at which levels and energies the HOMO and LUMO will be and thus the charge transport properties.

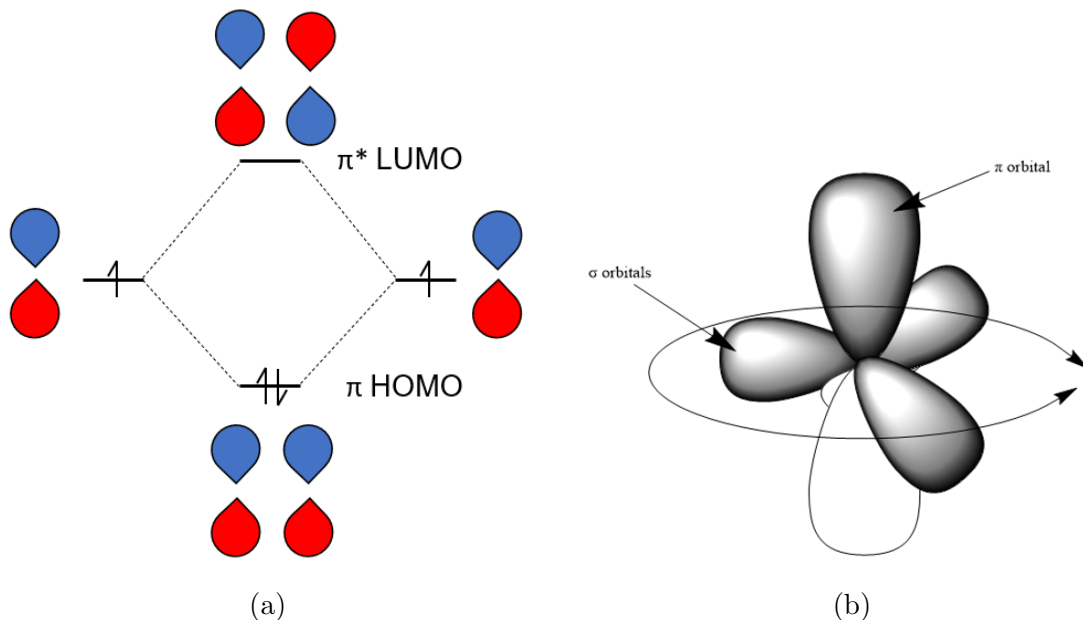


Figure 2.2: (a) HOMO and LUMO levels of ethene, showcasing the  $\pi$  bonds and antibonds. (b) Orbital structure of ethene, showing the lone  $\pi$  orbital in the vertical axis (from the  $2p_z$  orbital) and the  $\sigma$  orbitals in the horizontal plane (from the three  $sp^2$  orbitals).

Hopping occurs when carriers jump from one of these states to another. The difference between band transport and hopping conduction is that the transport is intra-molecular in band transport and inter-molecular in hopping conduction. The electrons move along the polymer chain and hop between the  $\pi$  orbitals of adjacent chains [24]. The quality of this conduction method is objectively poorer and thus less useful from an electronics standpoint. Typically, any organic material will conduct due to both transport mechanisms to some degree. However, the more crystalline a material is, the more band transport begins to dominate the conduction. In the literature, there are great efforts to increase the crystallinity of organic semiconductor materials in order to increase the conductivity [29–31]. Since organic materials are solution-processable, this has been done by attaching various functional groups to the molecule to increase the packing. Various deposition methods have also been tested in order to study their effects on crystallinity [32]. It is generally agreed upon that the conduction mechanism is the biggest roadblock to the widespread adoption of high-speed organic transistor devices [24, 29].

Organic semiconductors can also be doped, although not as easily as inorganic materials [33, 34]. To increase the number of charge carriers, either an n-type or p-type dopant may be added to the matrix (generally in solution). However, these dopants must have specific HOMO or LUMO levels and have a high molar mass to avoid instability issues. Single-atom halogens and metals have been used as dopants, but have proved to be an unreliable method, with instability issues arising from the small molecular weight dopant’s tendency to diffuse easily. For a p-type dopant, the LUMO level must be near the HOMO level of the matrix. Electrons may jump from the matrix to the dopant LUMO level, leaving behind a hole and creating p-type carriers. Likewise, the HOMO level must be near the LUMO level of the matrix for an n-type dopant. Thus, an electron can be injected from the dopant into the matrix and create excess n-type carriers.

## 2.1.2 Types of Organic Semiconductors

Organic semiconductors can either be small molecule, oligomeric, or polymeric compounds. These can be further divided into two types of semiconductor, n-type and p-type, which dictate the majority carrier in the material (electron or hole, respectively). Unfortunately, n-type organic semiconductors are much rarer than their p-type counterparts [35]. This is because the  $\pi$  orbitals are inherently more conducive to hole transport due to the need for the bonding orbitals needing to overlap rather than the antibonding orbitals as is the case for n-type transport. N-type organic semiconductors also experience problems with oxidation due to electron traps that impede n-type transport [36]. Thus, progress in organic electronic applications where both p-type and n-type materials are required, such as complementary logic gates or organic p-n junctions, has been lagging.

There have been numerous small molecule organic semiconductors reported along with devices built using them. Pentacene, a p-type small molecule organic semiconductor, has been used extensively in OFETs due to its relatively high mobility. Mobilities as high as  $58 \text{ cm}^2/\text{V}^*\text{s}$  have been reported for this molecule [37]. Tris(8-hydroxyquinoline)aluminum(III), or  $\text{Alq}_3$ , has been widely used as an electron-transporting layer in OLEDs due to its high fluorescence [38, 39]. However, as an n-type small molecule, its poor mobility makes it unsuitable for transistor applications. Fullerenes such as  $\text{C}_{60}$ , also affectionately referred to as the buckyball for its resemblance to a soccer ball, is an n-type small molecule that has been used as the channel material in OFETs [40]. Anthopoulos et al. demonstrated ambipolar charge transport in a  $\text{C}_{70}$  methanofullerene, with electron mobility approximately equal to  $1 \times 10^{-3} \text{ cm}^2/\text{V}^*\text{s}$  and hole mobility approximately equal to  $2 \times 10^{-5} \text{ cm}^2/\text{V}^*\text{s}$  [40]. This demonstrates the advantage inorganic semiconductors have over organics - for reference, the electron mobility of silicon is of the order of  $1000 \text{ cm}^2/\text{V}^*\text{s}$  at 300K [41].

Some examples of oligomeric organic semiconductors include  $\alpha$ -sexithiophene (T6) and oligofluorenes. Sexithiophene-based p-type OFETs have been demonstrated by growing via polycrystalline films by Horowitz et al [42]. Spirobifluorene, a p-type amorphous organic semiconductor, has been used as a blue light emitter in OLEDs due to its high photoluminescence quantum yield (PLQY) [43]. However, oligomeric compounds are not used as often as polymeric compounds due to the latter's higher stability. Organic semiconductors inherently are more unstable in ambient environment conditions than inorganics due to their higher reactivity with oxygen and water vapour. Polymeric compounds gain a higher stability by accumulating a greater number of repeating units than oligomers, increasing the number of interchain interactions [44].

Polymeric organic semiconductors have been extensively used for various electronic applications. Poly(3-hexylthiophene) (P3HT) is a p-type polymer that has been used in OFETs [45]. Poly[3,6-bis(5-thiophen-2-yl)-2,5-bis(2-octyldodecyl)pyrrolo[3,4-c]pyrrole1,4(2H,5H)-dione-2,2'-diyl-alt-thieno[3,2-b]thiophen-2,5-diyl] (DPP-DTT) has been used in p-type FETs due to its high mobility, and has also been used as the donor material in bulk photovoltaic devices [46, 47]. Polyaniline (PANI) is another p-type polymer that is popular for pH sensing. Poly(benzimidazobenzophenanthroline) (BBL) is an n-type polymer that has shown promise as an OFET channel material [48].

An important class of conducting polymers is the organic mixed ionic-electronic conductor (OMIEC). These polymers are able to interact with ions in surrounding media to change their structure and properties [49]. They have been used in applications where inducing charge in the material itself is crucial, such as batteries and supercapacitors [50, 51]. A popular application for OMIECs that has been gaining traction in recent years is in OECTs, which are able to transduce ionic charges in surrounding electrolyte into electrical signals [52]. Although its first applications were not as an OMIEC, the p-type conducting polymer poly(3,4-ethylenedioxythiophene)

polystyrene sulfonate (PEDOT:PSS) is the most widely used channel material for OECTs and is one of the highest performing p-type semiconductors in terms of transconductance [53–55]. Small molecule naphthalene diimide-based polymers such as p(gNDI-gT2) have been used as n-type channels for OECTs as well [56]. This thesis demonstrates OECT devices built with PEDOT:PSS and an n-type OMIEC, gNDI-Br<sub>2</sub>. They are examined more in depth in Section 2.2.

## 2.2 Organic Electrochemical Transistors (OECTs)

In this thesis, the transistor device that is used for sensing is the organic electrochemical transistor (OECT). To understand how an OECT operates, it is important to highlight the differences between OECTs, regular OFETs, and inorganic MOSFETs. OFETs have a similar structure to traditional MOSFETs in that they have three terminals: source, drain, and gate. They both have a thin dielectric layer that makes use of the field-effect through application of a gate voltage to generate a current between source and drain. The main difference between organic and inorganic FETs is the channel material and the mode that they operate in. Since MOSFETs include doped wells underneath their drain and source contacts, the channel created due to the gate voltage must be made according to the carrier that must be present between these wells. For example, for an n-type enhancement mode MOSFET, the wells must be n-type and the substrate material must be p-type to generate an n-channel between the wells for electron transport. On the other hand, the majority of OFETs operate in accumulation mode, that is, they accumulate majority carriers [14]. Since OFETs do not include doped wells as part of their structure, and most organic semiconductors are p-type, a negative gate voltage is generally applied to generate an accumulation of majority carriers (holes) near the semiconductor-dielectric interface, creating a channel. Current then flows if a bias exists between source and drain. However, due to poor conduction of organic semiconductors, OFETs operate at high voltages which does not make them useful for biosensing applications. High voltage

operation requires more sophisticated and bulkier circuitry, which is disadvantageous for applications where biosensors must be miniaturized, such as wearable electronics. Typical gate and drain voltages for OFETs are on the order of tens of volts, which also may be unsafe for wearable electronics applications. On the other hand, OECTs operate at comparatively much lower voltages due to their structure and working principle which are outlined in the next section [18].

### 2.2.1 Operating Principle

Like other transistor devices, OECTs include a source, drain, and gate terminal, with the gate terminal modulating the current between source and drain. The main difference between OECTs and other FET devices is the inclusion of an electrolyte as part of its structure in the place of the traditional dielectric layer. Additionally, the semiconducting channel material is an organic mixed ionic-electronic conductor (OMIEC). The structure is shown in Figure 2.3.

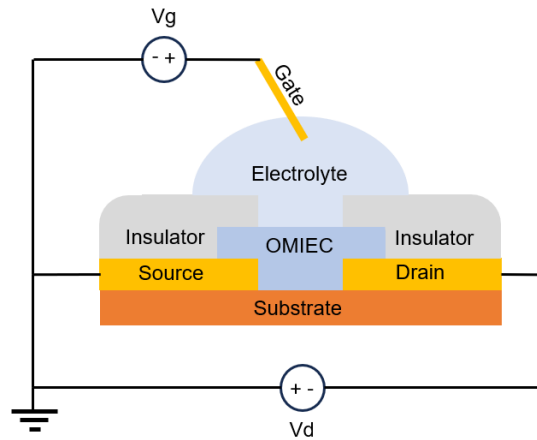


Figure 2.3: Cross-section of a typical OECT with a test probe used as a gate. The gate voltage is positive and the drain voltage is negative, consistent with a p-type depletion mode device.

Because of the inclusion of an electrolyte and OMIEC, an OECT is more complex than a regular OFET. The underlying physics behind a p-type depletion mode OECT can be described by the Bernard’s model. The device can be modelled as both an electronic and ionic circuit [52].

The electronic circuit consists of a resistance between the source and the drain which is the p-type semiconductor that transports holes. This relationship is simply Ohm's law, which relates voltage, current, and resistance. The resistance itself is non-linear with changing bias conditions as is the case for transistor devices. For regular OFET or MOSFET devices, this non-linearity comes from the gate bias forming a channel with increasing or decreasing gate voltage which changes the channel's resistance (from OFF state to ON state or vice versa). As discussed previously, an OECT uses an OMIEC as its channel material. An OMIEC undergoes a chemical reaction with ions which changes its structure and thus its conductivity. When a gate bias is applied to an OECT gate, ions from the electrolyte are driven into the OMIEC film, changing its conductivity non-linearly. In the case of PEDOT:PSS, the main p-type OMIEC used in this work, the semiconductor becomes less conductive when cations are driven into the film. Thus, it is quite simple to model the electronic circuit very similarly to a regular p-type depletion mode device. There are two regimes of operation, the linear and saturation regimes, which describe the drain-to-source current as a function of the drain voltage.

$$I_D = \frac{Wd}{L} \mu C^* (V_T - V_G + \frac{V_D}{2}) V_D \quad (2.1)$$

$$I_{D,SAT} = \frac{Wd}{2L} \mu C^* (V_T - V_G)^2 \quad (2.2)$$

Equations 2.1 and 2.2 describe the current through the device in the linear and saturation regimes, respectively, where  $I_D$  is the drain-to-source current (usually negative as the conventional current flows from source to drain) (A),  $W$ ,  $L$ , and  $d$  are the channel width, length, and thickness (cm),  $\mu$  is the mobility of the semiconductor carriers ( $\text{cm}^2/\text{V}^*\text{s}$ ), and  $C^*$  is the volumetric capacitance ( $\text{F}/\text{cm}^3$ ).  $V_T$ ,  $V_G$ , and  $V_D$  represent threshold, gate, and drain voltages, respectively (V). Because the saturation regime is defined as the point at which  $V_D = V_G - V_T$ , Equation 2.1 can be rewritten

as Equation 2.2, with the constant saturation current represented by  $I_{D,SAT}$ . It should be noted that there is one key difference in the equations between the equation for a traditional MOSFET and an OECT - the OECT equation contains the thickness of the channel whereas the MOSFET equation does not. This is due to the inclusion of the volumetric capacitance in an OECT device channel rather than the capacitance of the oxide in a MOSFET. Since it is volumetric, a thickness (in cm) value is required. The volumetric capacitance,  $C^*$ , is a material property that depends on the channel material.

Some important characteristics which can be extracted from OECT performance curves are the transconductance, voltage threshold, and mobility. The transconductance is defined as the change in drain current over the change in gate voltage. Taking the derivative of Equation 2.2 with respect to gate voltage, we can express transconductance as follows:

$$g_m = \frac{Wd}{L} \mu C^* (V_T - V_G) \quad (2.3)$$

where  $g_m$  represents the transconductance in Siemens and the rest of the symbols have their usual meanings. Experimentally, this value can also be extracted by simply taking the absolute change in current and dividing it by the gate voltage step size. Since transconductance is a direct measure of current change, it can be used as a good indicator of device sensitivity [18, 57]. In many sensing applications, current change is measured in response to a change in electrolyte concentration [58]. Since different electrolyte concentrations change the effective gate voltage of the device, a high transconductance indicates a large change in current with a small change in gate voltage, indicating a more useful device.

Voltage threshold is another important characteristic that indicates at which gate voltage a device turns on. Rearranging Equation 2.2, we can obtain the following expression:

$$\sqrt{I_{D,SAT}} = -\sqrt{\frac{Wd}{2L}\mu C^*V_G} + \sqrt{\frac{Wd}{2L}\mu C^*V_T} \quad (2.4)$$

where the symbols have their usual meanings. This equation implies that the voltage threshold can be extracted by plotting the square root of the drain current against the gate voltage (with the graph being plotted for a certain drain voltage). The slope of the linear part of the curve is then extrapolated to the x axis and the voltage threshold is taken as the x intercept. The voltage threshold is important when it comes to determining the operating voltage ranges for a device. This becomes a crucial characterization step for circuit applications, where device threshold matching is imperative for the optimal performance of the circuit [59]. Rearranging the slope in Equation 2.4, we can also extract the saturation mobility of the semiconductor:

$$\mu^{sat} = 2slope^2 \frac{L}{WC^*} \quad (2.5)$$

where  $\mu^{sat}$  is the saturation mobility ( $\text{cm}^2/\text{V}^*\text{s}$ ), slope is the slope of the linear portion of the curve when plotting Equation 2.4, and the rest of the symbols have their usual meanings. Mobility is an important characteristic when it comes to determining the speed of a transistor. For the purposes of this thesis, mobility is not extracted as it is not required for our sensing application. For OECTs in general, a consequence of the ionic circuit is that the ionic mobility is a more limiting factor than the carrier mobility. Additionally, to isolate the mobility, the volumetric capacitance  $C^*$  must also be determined by measuring gate currents and making approximations based on estimated injected charges. For these reasons, in general, the product of the two,  $\mu C^*$ , is normally used [60].

The ionic circuit consists of the gate, electrolyte, and channel, and is described mainly by the movement of the electrolytic ions between these components. In the ionic circuit model, the components between the gate and the channel are modelled

by a resistor and capacitor in series [52]. The resistance is due to the intrinsic resistivity of the electrolyte, while the capacitance is an equivalent capacitance describing two capacitors in series: the capacitance at the gate/electrolyte interface, and the capacitance at the electrolyte/channel interface. These interfaces are called the electrolytic double layer (EDL). The model is illustrated in Figure 2.4 (a). The equivalent capacitance is expressed below in Equation 2.6:

$$\frac{1}{C_{EQ}} = \frac{1}{C_{GE}} + \frac{1}{C_{CE}} \quad (2.6)$$

where  $C_{EQ}$  is the equivalent capacitance (F),  $C_{GE}$  is the gate-electrolyte capacitance (F), and  $C_{CE}$  is the channel-electrolyte capacitance (F).

## 2.2.2 OEET Materials

### Gate Materials

Like the electrode material, the gate material for OEETs can be any conductive metal, such as gold (Au), silver/silver chloride (Ag/AgCl), platinum (Pt), or copper (Cu) [18, 57]. However, depending on the polarizability of the material, the voltage profile across the electrolytic double layer will change. Polarizability is defined as the measure of a material's ability to acquire an electric dipole moment when exposed to an electric field. Due to this dipole moment, a capacitance is induced at the gate/electrolyte interface. With more polarizable materials such as Au and Pt, this capacitance will be larger and will induce a larger voltage drop across the EDL. With a non-polarizable material such as Ag/AgCl, the voltage drop is negligible because of the low  $C_{GE}$ . This difference is illustrated in Figure 2.4 (b).

The voltage drop across a polarizable material results in different characteristics for a finished device. Most notably for this work, the threshold voltage is mainly impacted. In this work's OEETs, gold was used as the material for both the electrodes and the gate. Prior to optimization, the devices were built using silver electrodes with

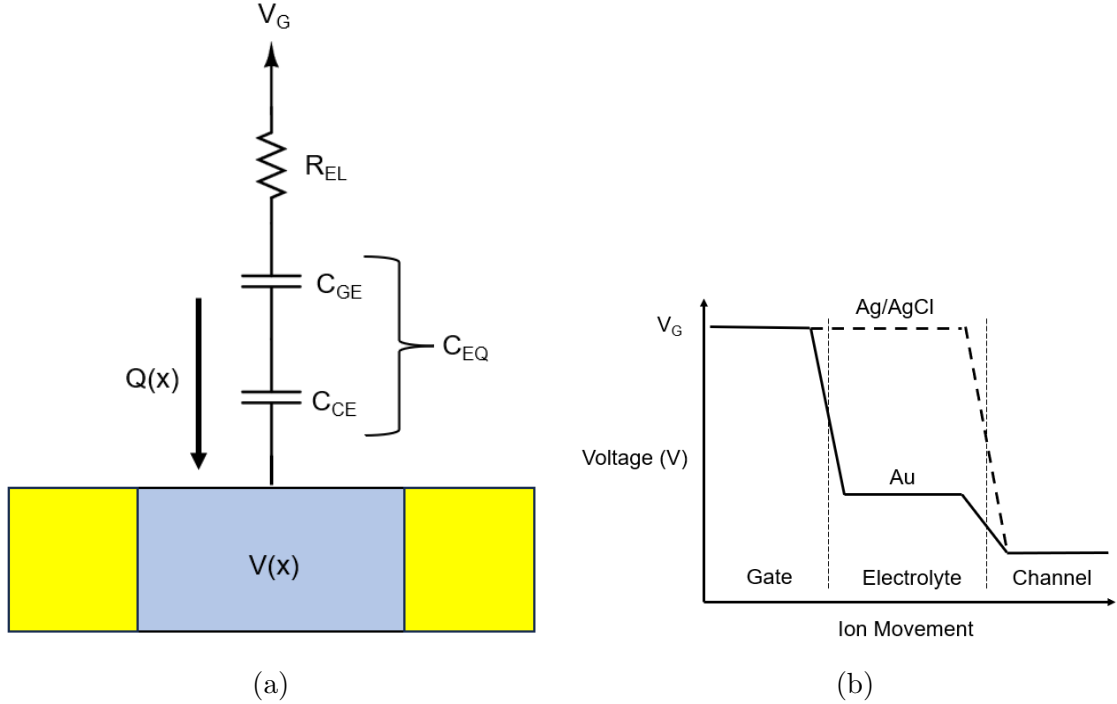


Figure 2.4: (a) The ionic circuit model of an OECT gate-electrolyte-channel interface.  $Q(x)$  indicates the movement of ions through the equivalent series resistance and capacitances. (b) Potential profile of an OECT gate-electrolyte-channel interface. Polarizable materials such as Au induce a larger voltage drop across the gate-electrolyte interface than non-polarizable materials.

an Ag/AgCl probe being used for the gate. Due to the polarizability of the Au gate, the effective gate voltage at the electrolyte was lowered. As a result, a higher gate voltage at the source was required to drive the same amount of ions into the channel to turn it off. This translated into a higher voltage threshold which changed the operating points of the device.

There are two main kinds of gate configurations for an OECT. In some designs, a gate probe is directly inserted into the electrolyte from above the device [18]. The electrolyte is only covering the channel and the gate probe is directly connected to the measurement device, usually a sourcemeter. In other devices, a planar gate is included in the design that is separated from the channel by a fixed distance [58]. When the electrolyte is dropped, it is required that the electrolyte is covering both the channel and gate in order to create the ionic circuit shown in Figure 2.4 (a). The gate probe

that is used to measure the device is usually landed on a contact pad connected to the larger gate and is typically made of the same material as the rest of the measurement probes (usually tungsten). This layout is shown in Figure 2.5. The area of the planar gate has also been shown to have an effect on the threshold voltage. As the area of the planar gate increases, the voltage drop at the gate-electrolyte decreases [1]. As a result, the effective gate voltage is not degraded as much as for a smaller gate and ultimately decreases the threshold voltage.

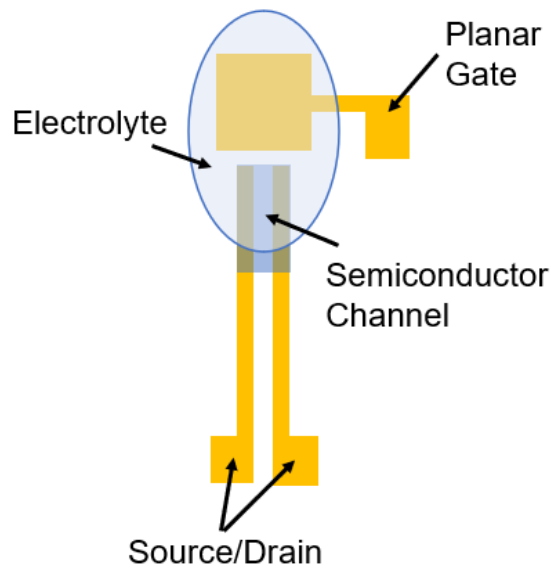


Figure 2.5: Top-down view of an OEET with a planar gate. The electrolyte is dropped over top of a planar square that is then contacted with a test probe.

### Substrate Materials

OEETs can be fabricated on a variety of substrates. Inorganic transistors, such as silicon, are fabricated on silicon wafer substrates due to the traditional process flow; silicon wafers can be doped, etched, and thermal oxide can be easily grown on them. Batch processability is also a major consideration - wafers can be easily stacked and mass production is feasible [61]. OEETs can also be fabricated on silicon substrate; the electrode and gate materials may be sputtered on the wafer after a

photolithography step. This allows for much smaller channel lengths and feature sizes than other additive techniques. For example, the current smallest feature size in commercial computer chips is 3 nm at the time of this writing [20]. In this thesis, 3D printing is used as the main additive fabrication technique for device electrodes - this results in a minimum channel size of approximately 20  $\mu\text{m}$ . For devices fabricated on wafer substrate, electrode tracks are deposited using traditional methods and organic semiconductor is then deposited on top using additive fabrication techniques, such as spin-coating.

Despite the advantage of small feature sizes and a time-tested process, devices made on wafer substrate are rigid and cannot be conveniently used in biosensor applications where conformity with a physiological environment, such as skin, is required. This is why many OECTs are fabricated on flexible substrates, such as polyimide (PI) or polyethylene terephthalate (PET) [18, 57, 58]. These are the two main flexible polymer substrates used in device fabrication, although in recent years, other substrates such as textiles have been studied for the purposes of patient comfort in the area of biosensing. Another advantage of these substrates is biocompatibility, which is important for medical and ethics approval of biosensor devices.

### **Channel Materials**

As previously discussed, the channel material of OECTs is a subset of organic semiconductors called organic mixed ionic-electronic conductors (OMIECs). These are a special class of ion-permeable organic semiconductor that chemically react with ions to tune their conductivity. An organic semiconductor can either be p-doped, called the oxidized state (loss of an electron), or n-doped, called the reduced state (gain of an electron) [1]. An OMIEC can be easily oxidized or reduced by the permeation of ions from an electrolyte by an applied voltage. A positive voltage would result in cations in the electrolyte being driven into the OMIEC film, and a negative voltage would drive in anions. Depending on the material, either of these can initiate an

ionic reaction and set the conditions for transistor-like behavior [49]. Based on the OMIEC material, the devices made can either be in accumulation mode or depletion mode - that is, the transistor behavior arises from the accumulation or depletion of majority carriers in the transistor channel due to the gate voltage, which modulates the current.

In the literature, there are various examples of OMIECs being used in OECT channels. The most popular material used in OECTs is poly(3,4-ethylenedioxythiophene) polystyrene sulfonate (PEDOT:PSS). This is a p-type material that operates in depletion mode when used in OECTs. This material is outlined in greater detail in Section 2.2.3 as it is used extensively in this work. Other examples of p-type OMIECs include polypyrrole (PPy) and poly(2-(3,3'-bis(2-(2-(2-methoxyethoxy)ethoxy)ethoxy)-[2,2'-bithiophen]-5-yl)thieno[3,2-b]thiophene) (p(g2T-TT)), which operate in the accumulation mode [62, 63]. For both of these materials, a negative gate voltage is applied which causes anions to oxidize the material, accumulating majority carriers (holes) and inducing current if there exists a bias between source and drain.

There also exist n-type OMIECs; however, as with all organic semiconductors, their development has been hindered by poor stability and degradation [57]. Despite being organic compounds that should readily react with water and oxygen, the reason that p-type organic semiconductors are not impacted in the same way is that the degradation issues associated with n-type materials occur because of water and oxygen-generated electron traps that specifically impede n-type conduction, rather than a chemical instability [36]. Some examples of popular n-type OECT channel materials include poly(benzimidazobenzophenanthroline) (BBL) and p(gNDI-gT2), which is a copolymer of thiophene and 2,6-dibromonaphthalene-1,4,5,8-tetracarboxylic diimide-co-monomers. BBL is an n-type accumulation mode device - that is, a positive gate voltage is applied and the film is reduced resulting in a higher concentration of electrons and thus current. It is widely studied in the literature because of its high conductivity for an n-type device [48]. p(gNDI-gT2) is an ambipolar material, mean-

ing that it can be doped with both cations and anions, resulting in both p-type and n-type transport [56]. When a positive gate voltage is applied, a p(gNDI-gT2)-based OECT functions as an n-type accumulation mode device. When a negative gate voltage is applied, it functions as a p-type accumulation mode device. This thesis includes n-type OECTs fabricated with the channel material gNDI-Br<sub>2</sub>, which is outlined in greater detail in Section 2.2.4.

### 2.2.3 PEDOT:PSS

The main p-type OMIEC used in OECTs in this work is poly(3,4-ethylenedioxythiophene) polystyrene sulfonate, or PEDOT:PSS. It consists of the polymer PEDOT and a dopant, PSS. The structure is shown in Figure 2.6 (a). Not only is PEDOT:PSS used as an OMIEC, its conductivity is high enough that it is used as a conductive polymer for a variety of applications such as organic solar cells, contact electrodes, supercapacitors and fuel cells [53]. It also possesses good chemical and electrical stability in air, making it an excellent candidate for mass production of devices for these applications [58]. All these features make PEDOT:PSS arguably the most popular p-type organic semiconductor. In this work, PEDOT:PSS is used as an OECT channel material due to its stability, solubility in water, solution-processability, and extremely high transconductance. The redox reaction is shown below in Equation 2.7:



where  $M^+$  is any metal cation found in the device's electrolyte, and  $e^-$  is an electron. As shown in Figure 2.6 (b), on the PSS chains, there exist  $SO_3^-$  groups that bond with the thiophene groups on the PEDOT chain, oxidizing it and facilitating hole conduction by knocking an electron off of the chain. When a positive gate voltage is applied, metal cations are driven into the film, drawing the PSS away from the PEDOT. The PEDOT is then reduced with the free electron, lowering the conduc-

tivity. In an OECT application, this translates to a p-type depletion mode device with a positive voltage threshold. The device is normally on and as the gate voltage increases, it shuts off.

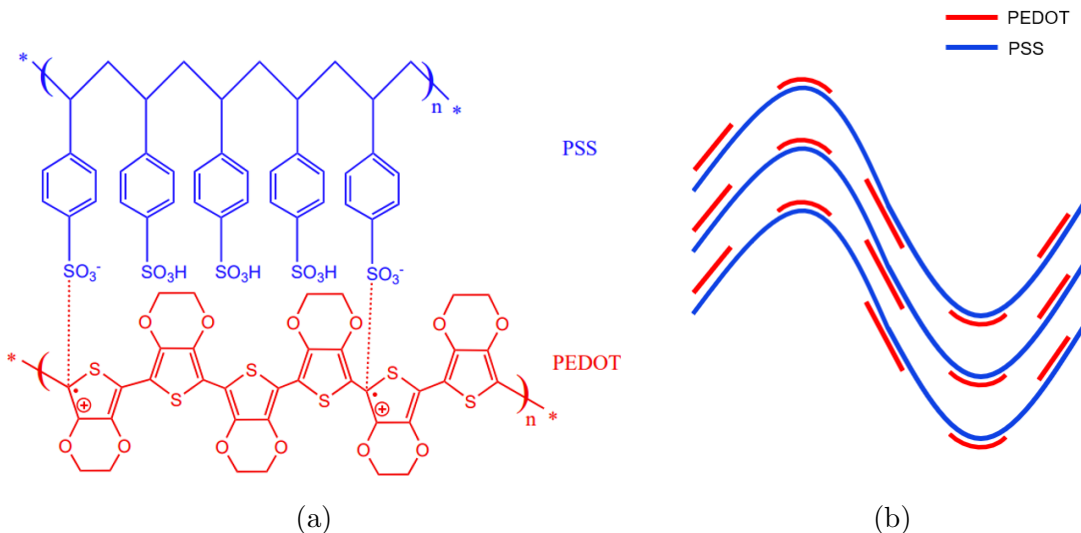


Figure 2.6: (a) Chemical structure of PEDOT:PSS. (b) Visual representation of interaction between PEDOT and PSS.

### 2.2.4 gNDI-Br<sub>2</sub>

The n-type OMIEC used in OECTs in this work is a naphthalenediimide (NDI)-based small molecule, gNDI-Br<sub>2</sub>. In this work, the synthesis of the NDI compound and synthesis and development of the NDI ink recipe was carried out by Seongdae Kang of the author's research group. NDI-based n-type conducting polymers have been used for a variety of applications such as organic solar cells and OECTs [56, 57, 64]. As mentioned in Section 2.2.2, another NDI-based polymer, p(gNDI-gT2), is an ambipolar n-type semiconductor that has been used in OECTs and has demonstrated both n and p-type transport. In this work, gNDI-Br<sub>2</sub> was used strictly as an n-type material in the accumulation mode. Its structure is shown in Figure 2.7.

The gNDI-Br<sub>2</sub> molecule consists of core naphthalene rings, ethylene glycol sidechains, and carboxylic oxygen atoms. The core naphthalene rings result in strong  $\pi$ - $\pi$  interac-

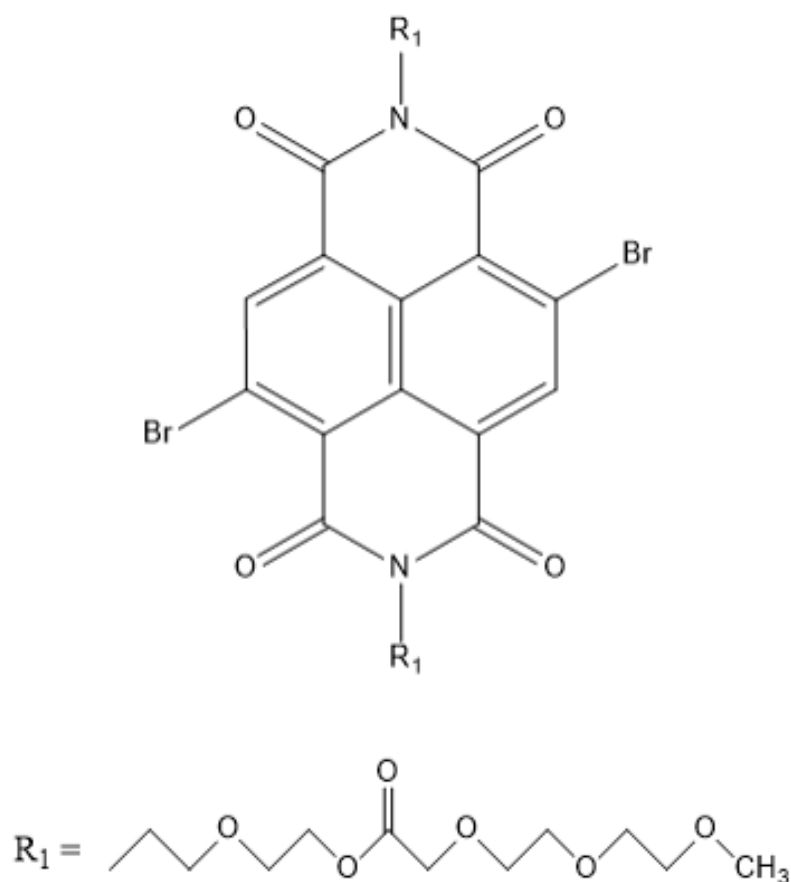


Figure 2.7: Chemical structure of gNDI-Br<sub>2</sub>.

tions between molecules, increasing crystallinity and enhancing conductivity [57]. The ethylene glycol sidechains also enhance conductivity while also giving the molecule the ability to dissolve in a variety of solvents, which is crucial for fabrication and widespread adoption of any organic semiconductor. The oxygen atoms are used as sites for coupling with metallic cations, which is the basis of the redox reaction for this OMIEC. The full reaction is shown below in Equation 2.8:



where the symbols have their usual meanings. As a positive gate voltage is applied, the metal cations are driven into the channel and are coupled with two of the carboxylic

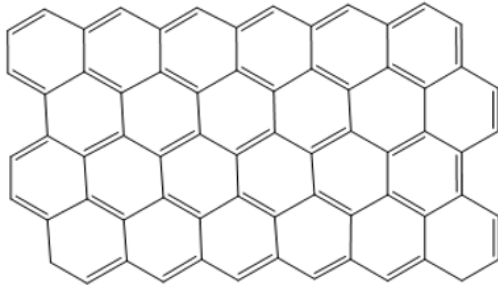
oxygen atoms found at opposing sides of the core NDI molecule. As this reaction occurs, two electrons are freed from the core and contribute to the current. Thus, the device acts as an n-type accumulation mode OECT. The device is normally off and as the gate voltage increases, it turns on.

## 2.3 Carbon Nanotubes (CNTs)

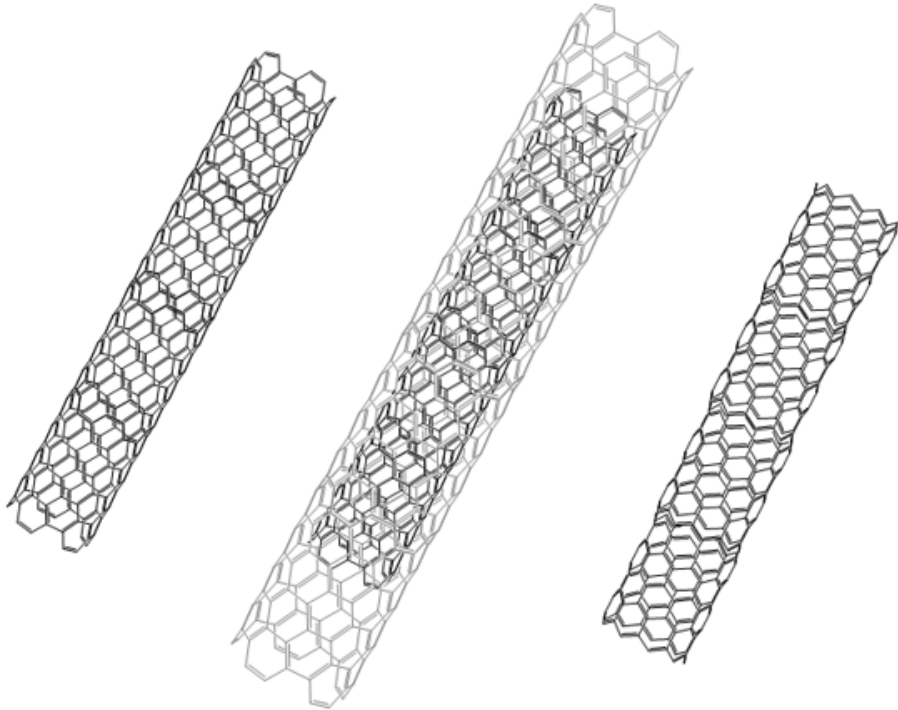
### 2.3.1 CNT Structure and Properties

Carbon nanotubes (CNTs) have gained considerable attention in recent years due to their excellent mechanical and electrical properties. Carbon nanotubes have been used in mechanical contexts as a reinforcement material - the Young's modulus of single-walled carbon nanotubes has been measured up to 1.8 Tpa [65]. For reference, steel has a Young's modulus of approximately 210 GPa [65]. CNTs also have excellent conductivity, reaching  $10^7$  S/m for pure individual tubes [66]. Also, copper has one of the best conductivities on the order of  $10^7$  S/m, and hence is widely used in electrical wiring. The structure of various carbon nanotubes is illustrated in Figure 2.8 (b). At their essence, carbon nanotubes are sheets of graphene "rolled" into tube-like structures. Graphene is a 2D material - that is, it is a single monolayer of carbon atoms bonded in a hexagonal honeycomb lattice [67]. This is in contrast to graphite, which is a 3D bulk material with multiple carbon sheets. The structure of graphene is illustrated in Figure 2.8 (a).

As shown in Figure 2.8 (b), CNTs can have various configurations. Firstly, CNTs are divided into two categories: single-walled and multi-walled [65]. Single-walled CNTs (SWCNTs) consist of a single rolled tube of graphene, usually with a diameter ranging up to approximately 2 nm. Multi-walled CNTs (MWCNTs) contain multiple SWCNTs stacked inside each other (concentric tubes). Their diameters range depending on the number of walls, but may reach up to 100 nm. For both SWCNT and MWCNTs, lengths are in the  $\mu\text{m}$  range, usually around 10  $\mu\text{m}$ . Electronically,



(a)



(b)

Figure 2.8: (a) The structure of graphene. (b) The structure of various carbon nanotubes. From left to right: single-walled nanotube with configuration (5,5) armchair, multi-walled nanotube (2 walls) with configuration (5,5) armchair, single-walled nanotube with configuration (9,0) zigzag.

MWCNTs exhibit metallic characteristics and conduction while SWCNTs can be either metallic or semiconducting depending on their chirality [66]. Chirality is the main indicator of electronic properties in CNTs and describes the lattice structure of the "unrolled" graphene sheet [68]. The chiral vector,  $\vec{C}$ , is described below in Equation 2.8:

$$\vec{C} = na_1 + ma_2 \quad (2.9)$$

where  $n$  and  $m$  are integers called the chiral indices, and  $a_1$  and  $a_2$  are the base cell vectors of graphene. The diameter of the tube,  $D$ , can also be related to these quantities:

$$D = \frac{C}{\pi} = \frac{a_0}{\pi} \sqrt{n^2 + nm + m^2} \quad (2.10)$$

where  $C$  is the magnitude of vector  $\vec{C}$ ,  $a_0$  is a base cell vector of graphene, and the rest of the symbols have their usual meanings. There are three subsets of CNTs based on the combination of chiral indices [69]. These describe the orientation of the rolling of the CNT. In cases where  $m = n$ , an armchair nanotube is formed. A SWCNT with configuration (5,5) armchair is shown in Figure 2.8 (b). A zigzag nanotube occurs in the case where  $n = 0$  and  $m \neq n$ . This is illustrated in Figure 2.8 (b) with a configuration of (9,0) zigzag. All other combinations, that is, where  $m, n \neq 0$  and  $m \neq n$ , result in chiral nanotubes, which are varying degrees of rolling between the two extremes illustrated in Figure 2.8 (b). In terms of conductivity, armchair nanotubes exhibit metallic properties whereas zigzag and chiral nanotubes exhibit semiconducting properties. Synthesis techniques for all configurations of CNTs include the arc-discharge method, laser ablation, and chemical vapor deposition [65]. CNTs are then purified by various methods such as acid reflux, sonication, and air oxidation [70].

### 2.3.2 CNT Applications

Because of their superior mechanical and electrical properties outlined in the previous section, CNTs have been used in a variety of context including emerging industries such as the biosensing industry. Due to their high Young's modulus, which implies a high strain-to-stress ratio, and their high strength-to-weight ratio, CNTs have been used as reinforcement materials in construction contexts (cement reinforment) and

even ballistic materials [71, 72]. Because of the nanostructure nature of their composition, CNTs have been used in targetted drug delivery systems where nanotubes containing drugs are guided to various organs via magnets and splits upon entry into the cell [70].

In electronic applications, CNTs have been used as biosensors due to their reactivity towards various compounds. For example, they have been used in gas sensors owing to their reactivity towards  $\text{NO}_2$  and  $\text{NH}_3$  gas [73, 74]. They have also been used as a functionalization layer in various electronic biosensors because of reactivity towards specific compounds, enhancing conduction [75]. Most notably, however, they have been used as a channel material in FET devices [74, 76, 77]. Because only SWCNT have semiconducting properties, only SWCNTs have been demonstrated as the channel material. Forel et. al demonstrated logical inverters geared towards gas sensing using pristine SWCNTs [77]. Shulaker et al. demonstrated 3D integration of carbon nanotube FETS (CNFETs) by stacking layers of CNFET sensors, CNFET logic, and traditional silicon logic on a single chip [76]. CNFETs have shown promise as an alternative to traditional silicon CMOS devices by having demonstrating an energy-delay product on an order of magnitude higher [76]. The energy-delay product is an important measure of efficiency in digital circuits - a lower product results in lower power consumption and heat dissipation, prolonging the life of a chip and lowering costs for computing-intensive operations.

CNTs have also been used in passive electronics biosensors as a sensing material [78]. In this work, MWCNTs were used as the sensing material for a resistive temperature sensor, which is outlined in Chapter 3. In these types of devices, rather than the electron or hole type transport changing with applied bias, the structure of the CNT network changes in response to stimuli which can cause dramatic change in the conductivity, which is an easily quantifiable characteristic for electronic sensors.

## 2.4 Logic Gates

Logic gates are functional blocks that take one or multiple binary inputs and output a single binary output. In general, these are implemented in electronic circuits using integrated chips to achieve some kind of computing function [76]. However, they have also been implemented with mechanical, pneumatic, and even quantum-mechanical devices, because at their core they are devices that implement a mathematical Boolean function [79–81]. They may be used to implement larger computing algorithms and more complex Boolean algebra. This thesis focuses on the electronic implementation of logic gates. Because of this, it is important to understand the theory behind logic gate circuits.

### 2.4.1 Circuit Theory

As mentioned previously, logic gates implement specific Boolean functions. The most basic logic gate functions are NOT, AND, and OR. In the case of NOT gates, the input is simply inverted at the output, that is, a binary input value of 1 would be a 0 at the output and vice versa. In the case of the AND gate, input combinations of 00, 01, 10, and 11 would result in outputs of 0, 0, 0, and 1, respectively. OR gates are the opposite - the same input combinations would result in outputs of 0, 1, 1, and 1, respectively. These gates can be stacked together to make more complex gates such as NAND, NOR, XOR, and XNOR gates. It is worth noting that NAND and NOR gates are only more complex when representing them with logical symbols (AND/OR followed by a NOT gate). In reality, they require less transistors to implement electronically, which is why they are used more often in circuits. These gates can then be stacked together to create more complex logic blocks such as multiplexers, binary decoders, and data registers. For the purposes of this thesis, the logical and electronic circuit theory of the NOT gate will be examined in detail as it is explicitly used. NOT gates take an input and output its complement - they invert it, which is why they are also

referred to as inverters. Truth tables are tables that outline the logical combinations of inputs for logic gates and their outputs. The simple truth table for a NOT gate is shown in Figure 2.9 (a), along with its logic gate symbol and characteristic equation. Because logic gates are generally built as electronic circuits, the inputs and outputs are referred to both as X and Y (mathematically), and as  $V_{in}$  and  $V_{out}$ , because the output of electronic logic gates is always a voltage.

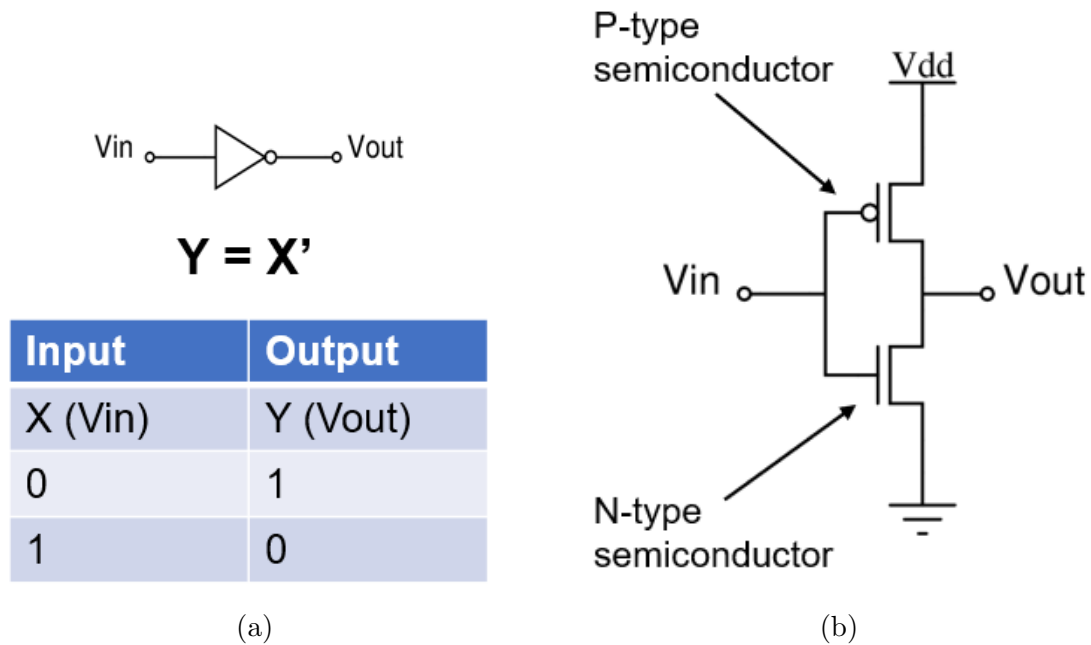


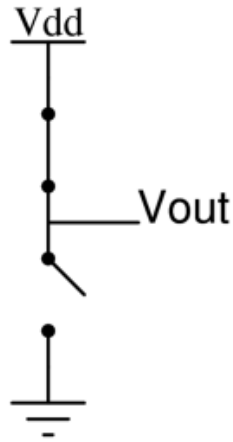
Figure 2.9: (a) Logic symbol, characteristic equation, and truth table for a NOT gate. (b) Electronic complementary circuit implementation of a NOT gate.

To implement NOT gates electronically, complementary metal-oxide-semiconductor (CMOS) technology is employed. As discussed in Section 2.1, semiconductors can either be p-type or n-type. CMOS logic gates use transistor devices with both p-type and n-type semiconductors as the channel material. If one device is turned on by an input voltage, the other is off, and vice versa, hence the "complementary" label. In CMOS gates, there is always a pull-up network (PUN) and pull-down network (PDN). The PUN consists of p-type devices while the PDN consists of n-type devices. The voltage output is taken between the two networks. If the PUN is conducting, the output is connected to the positive power supply voltage, and the PDN is disconnected

from the output. If the PDN is conducting, the output is connected to ground (0V), and the PUN is disconnected from the output. Usually, the logic levels for the output are taken as the power supply voltage ( $V_{dd}$ ), and ground (GND). The input voltage also takes these levels, i.e, the voltage equivalent for logic state 1 at the input must be  $V_{dd}$  and be enough to fully turn off the p-type devices (as p-type devices turn off as voltage increases) and fully turn on the n-type devices. The opposite is true for logic state 0 - the voltage must be GND and be enough to keep the n-type devices from conducting (OFF) while allowing the p-type devices to conduct (ON).

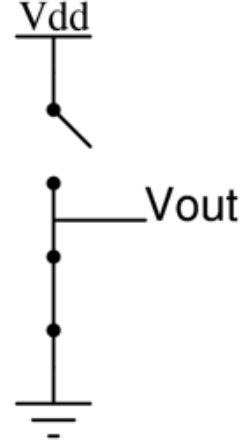
The two logic levels for the NOT gate are shown in Figure 2.10 (a) and (b). Since transistors can be modelled as switches, switch-style schematics can be used to illustrate conduction in CMOS logic circuits. Although the two extremes of  $V_{in}$  are shown in cases 1 and 2, intermediate voltages are possible and inevitable in any circuit, such as during voltage transitions. Sweeping the input voltage from logical 0 to 1 results in an output voltage response from logical 1 to 0, as shown in Figure 2.10 (c). This is an important curve for characterizing fabricated devices and can indicate defects in specific transistors [82].

**Case 1:  $V_{in} = \text{GND (0)}$ ,  
 $V_{out} = V_{dd} (1)$**



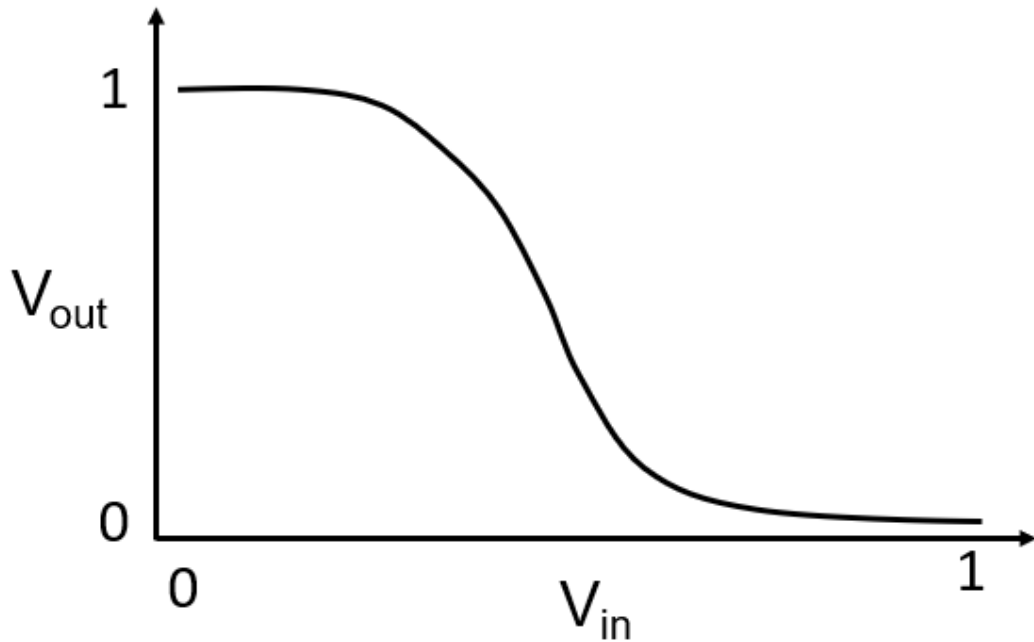
(a)

**Case 2:  $V_{in} = V_{dd} (1)$ ,  
 $V_{out} = \text{GND (0)}$**



(b)

### NOT Gate Transfer Curve



(c)

Figure 2.10: (a) Switch-level representation of a NOT gate with  $V_{in}$  of logic 0. (b) Switch-level representation of a NOT gate with  $V_{in}$  of logic 1. (c) The transfer curve of a NOT Gate.

## 2.4.2 Common Uses

The vast majority of logic gates are used in integrated circuits as part of larger circuits, such as those in microprocessors. The logic flow of these devices is shown in Figure 2.11. From simple transistor layouts and circuits, larger blocks such as multiplexers, adders, and subtractors can be built. These are represented by high level blocks, which is called the register transfer level (RTL). RTL blocks can be connected together to perform higher-end computing operations, such as those in a microprocessor or computer chip. Logic gates can also be individually integrated in discrete chip packages for specific applications, such as in non-integrated circuit design and embedded systems [76].

Logic gates have also been occasionally used in the biosensing industry [18]. As mentioned in Section 2.3.2, SWCNT-based FETs have been used in gas sensing. Forel et al. demonstrated NOT gates based on these devices for the purposes of NO<sub>2</sub> sensing [77]. Majak et al. have also demonstrated OECT-based NOT gates for ion detection [18]. The main advantage of using logic gates for biosensing is the ability to measure a voltage rather than a current, which is the case for most transistor-based biosensors. Measuring voltage requires less complex circuitry and results in more accurate measurement. OECT-based NOT gates have been demonstrated in the literature with varying circuit configurations due to the difficulty in fabricating both p-type and n-type OECTs with well-matched characteristics [16, 83, 84]. However, OECTs have rarely been built both as logic gates and for biosensing end-use. In this thesis, OECT-based NOT gates are used for the detection of various cations in solution as well as glucose measurement. The specific configuration and operation of the NOT gates are explained in more detail in Chapters 4 and 5.

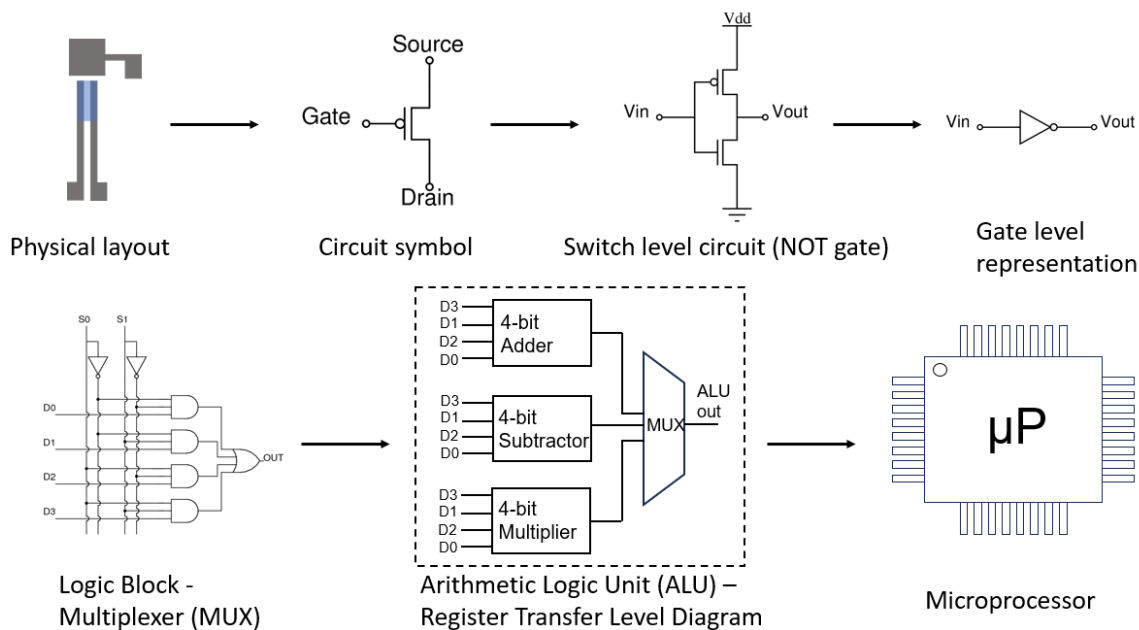


Figure 2.11: Integration of logic circuits in high-end computing applications.

## 2.5 Fabrication Techniques

### 2.5.1 Fabrication Techniques for Organic Semiconductors

A major advantage of organic semiconductors (OSCs) is their solution-processability, which allows them to be deposited by a variety of different methods. As discussed in Section 1.1, the main fabrication method of traditional inorganic FET devices is the photolithography/etching/sputtering process. The silicon wafer already contains the semiconductor - it must simply be selectively doped via ion implantation or diffusion, the pattern for which is transferred by photolithography [61]. This is called a subtractive technique. Typically, this process has also been used for organic FET devices as a means to deposit electrode contacts for the device, with the organic semiconductor deposited via additive techniques [58]. Photolithography has the advantage of nanometer-range feature sizes. Processes typically also use high quality metal (which results in low resistance) and produce highly reproducible results due to a well-optimized, time-tested process. However, it is a time-consuming and costly process, with mask, fabrication, and machine use costs, making constant prototyping

inconvenient.

For the deposition of organic semiconductors themselves, additive deposition techniques are in use. Since organic semiconductors are usually dissolved in solution, it is difficult to deposit them using traditional techniques such as sputtering, where solid metal targets are hit by energized particles. Surface atoms from the solid target are ejected and deposited onto the target substrate. The metal is then selectively removed via pattern transfer technique such as etching or lift-off. Thus, organic semiconductors are deposited using additive techniques, where materials are deposited or stacked one layer at a time. These can be direct-write techniques, meaning the deposition is selective from the start, removing the need for a mask. The most popular techniques include spin-coating, screen-printing, spray-coating, and 3D printing techniques such as inkjet printing, gas injection printing, and aerosol jet printing [18, 58, 85, 86]. 3D printing has become a popular technique due to its low cost and quick prototyping. Rather than laying out a mask and then manufacturing it, all that is needed is a computer-aided design (CAD) file that is converted to a script for the particular printing machine. The 3D printer then uses direct-write techniques to deposit a pattern on a substrate. In this work, aerosol jet printing is used as the main technique for the deposition of contact electrodes, semiconductor channel, and insulating layers. The operating principle is laid out in the next section.

### **2.5.2 Aerosol Jet 3D Printing**

Aerosol jet 3D printing is an additive deposition technique in which a material/ink is first aerosolized, moved through the system by gas, and finally deposited as a thin film on the substrate. Thicknesses are generally in the micron range. Feature sizes are in the tens of microns range, but can be improved upon by the optimization of certain parameters [1, 87]. The operating principle of aerosol jet is shown below in Figure 2.12. First, an ink is loaded into a vial which is inserted into an atomizer device. This atomizer can be either ultrasonic or pneumatic in nature. For an ultrasonic

atomizer, the bottom of the vial must be thin enough for the energy to penetrate the vial and aerosolize the ink. The aerosol is then carried through the system (usually a tube) via carrier gas (usually nitrogen gas) to a deposition head. The deposition head contains an opening for another gas called the sheath gas. The sheath gas is variable and focuses the aerosol stream depending on the pressure. A higher pressure results in a smaller deposition line. The deposition head also contains the tip, where the aerosol exits. The tip size is also variable and impacts the line width.

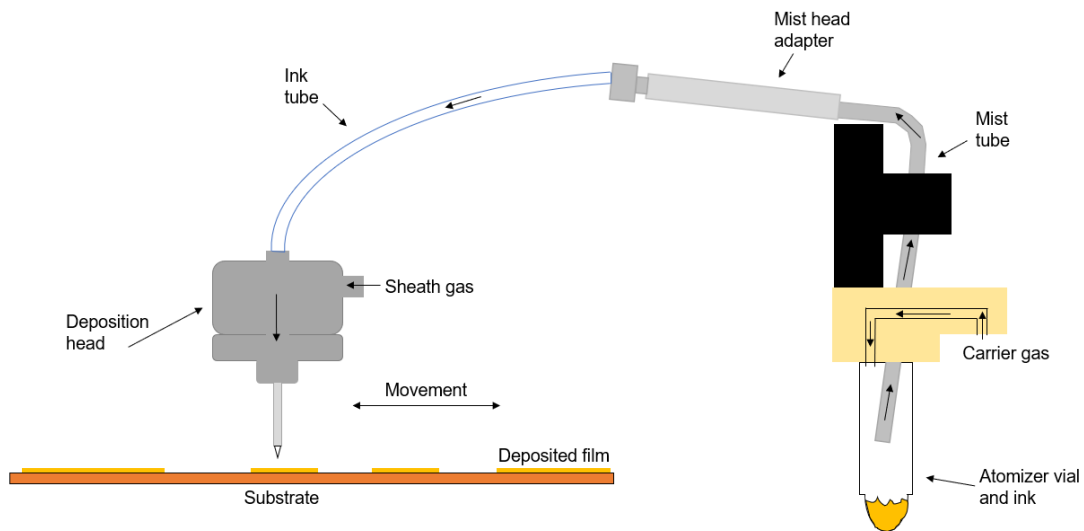


Figure 2.12: Schematic diagram of aerosol flow, gas flow, and deposition in aerosol jet printing.

The devices built in this work by aerosol jet printing were made by an Optomec Aerosol Jet 5X 3D Printer. The system is shown in Figure 2.13. It includes an ultrasonic and a pneumatic atomizer, though only the ultrasonic atomizer was used in this work. The pneumatic atomizer is reserved for inks with viscosities over 10 cps (up to 1000 cps). The system also includes a water bath and chiller, bubbler vial, deposition head with assorted tips (exit hole sizes 150, 200, and 300  $\mu\text{m}$ , and a platen heater capable of being heated to 80°C.

The critical parameters that impact deposition rate and linewidth are carrier and sheath gas pressure, atomizer power, amount of ink in the vial, bath temperature,

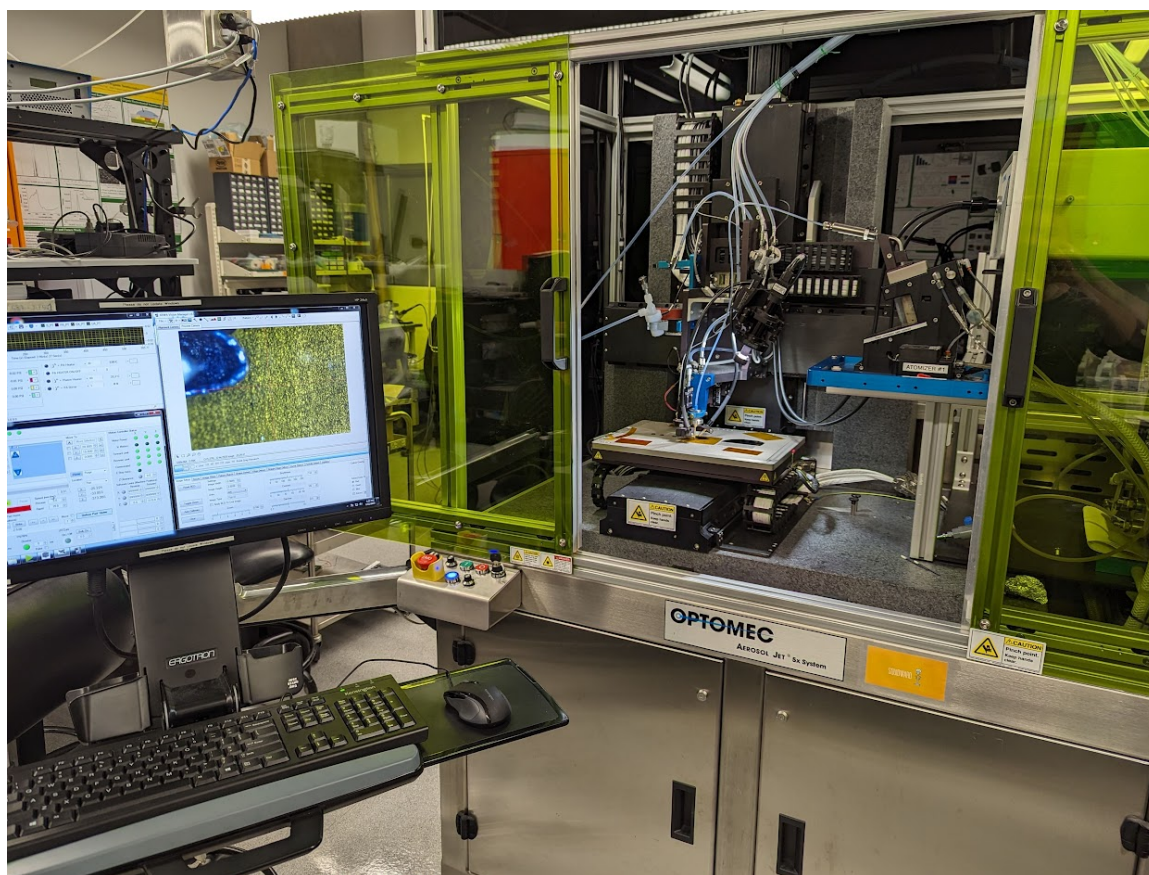


Figure 2.13: The Optomec Aerosol Jet 5X printing system.

bubbler contents, tip size, printing speed, and platen heater temperature. As carrier gas pressure increases, the rate of deposition increases as more aerosol is carried through the system to the exit. Sheath gas focuses the aerosol beam, resulting in a smaller line as pressure increases. Atomizer power also directly correlates with deposition rate. The amount of ink in the vial is usually 1-2 mL. It is crucial to have the exact amount of optimized ink the vial - otherwise, the ink may be too wet when exiting the tip, resulting in overspray and ruining fine features, or there may not be any deposition at all. The bubbler and bath temperature systems serve to add moisture to the aerosol. If it is too dry, a continuous line is difficult to print. The tip size directly influences line width by depositing a thicker line with a greater exit hole diameter. Printing speed also changes the continuity of the line - if speed is too fast, the ink may not have time to form a continuous film. On the other hand, if it

is too slow, the line may experience heavy overspray. The platen temperature also changes the deposition of the film in that a higher temperature may prevent a film from spreading too much in the case that the aerosol is too wet when exiting the tip. With this many parameters, it is obvious that optimization of a new ink or material for printing is not trivial and usually takes multiple prints, even if parameters are outlined in the literature. However, when optimized, aerosol jet printing provides a cost-effective, efficient, and robust fabrication method for structures such as organic semiconductor devices.

## **2.6 Characterization Techniques**

### **2.6.1 Profilometry**

Profilometry is a technique used to measure the surface profile/roughness of a film. It consists of a stylus that is connected to a moving stage, controlled by a computing system with a feedback control system. As the stylus moves on the surface of the sample, the system measures the vertical movement and plots a surface profile accordingly. Thus, it can be used to determine the thickness of the sample by sweeping the stylus from the smooth substrate the sample is found on over the beginning of the film. The height profile sees a clear change and the delta value can be taken as the thickness. In this work, an Alpha-step IQ Profilometer was used to determine the thickness of various thin films. For all the film thickness measured, height measurements were taken at the 4 corners of the film area (assuming a roughly square shape) and averaged to one thickness value. The system is most suited for measuring films with thicknesses in the micron range. For films with thicknesses and roughness profiles in the nanometer range, atomic force microscopy (AFM) is more commonly used.

### 2.6.2 4-Point Probe

A 4-point-probe (4PP) is a device used to measure the sheet and bulk resistivity of a thin film. It consists of four probes equally spaced apart which are spring-loaded to be able to contact the sample and are connected to a sourcemeter. The outer two probes force a current through the sample, while the inner two measure the voltage. This is inherently more accurate than a two probe measurement, where both probes are responsible for both sourcing a current and measuring the voltage to calculate the resistance. This causes inaccuracies due to contact resistance between the probes and the sample. When a 4PP measures the voltage across the two inner probes, this results in a sheet resistivity value. It requires no correction, assuming the thickness of the material is no more than 40% of the distance between two probes [88]. The probes must also be sufficiently far away from the edge of the sample to avoid the need for another correction factor. Using the sheet resistance value, the bulk resistivity of the material can be calculated if the thickness of the sample is known. Consequently, the thickness of the sample can also be determined if the sheet resistance is measured and the bulk resistivity of the material is known (i.e, from a datasheet). In this work, a Lucus Pro4 4000 system was used to measure the sheet resistivity of various 3D printed thin film squares. The bulk resistivity of these materials was then calculated using a thickness value which was measured using the Alpha-step IQ system outlined in the previous section.

### 2.6.3 UV-Vis Spectrophotometry

Ultra-violet-visible (UV-Vis) spectrophotometry is a technique used to measure the absorbance/reflectance spectra of a material. It consists of a light source that passes light through a sample, and a detector that measures the amount of light that has passed through. The light is passed through a diffraction grating to separate the wavelengths of light. The intensity of the transmitted light is then measured as a function of the wavelength. The wavelengths used are from parts of the ultra-violet

and visible light spectra, hence the name. Different materials have different characteristic spectra, with peaks appearing due to the excitation of electrons to higher energy states upon the absorption of photons. Thus, UV-Vis spectrophotometry can be used to identify different materials due to their characteristic spectra. It can also be used to detect changes in the composition of a material after treatment. In this work, a Hitachi U-3900H spectrophotometer was used to measure the absorbance spectra of carbon nanotube nanocomposite films. This was done to verify the uniformity of the films by measuring the same film in multiple locations.

#### **2.6.4 Thermogravimetric Analysis**

Thermogravimetric analysis (TGA) is a process used to identify the numerical weight composition of different elements or compounds in a material. A material is placed in a weighing boat which is calibrated and placed in a heating chamber which is then heated to a specific variable temperature at a variable rate. As the temperature rises, the weight of the boat changes due to specific parts of the material melting at variable rates. The vapour of the material is swept away by a purge gas which can also be changed (i.e nitrogen or air). The weight percentage of each element/compound in the material can be clearly seen in the %weight vs temperature plot, assuming the melting points of the constituents are sufficiently spaced apart. Some materials also only activate their pyrolysis at a certain temperature under a certain environment, such as with an air purging gas, which helps to isolate their weight percentage in the analysis. In this work, a Discovery TGA machine was used to conduct TGA of a carbon nanotube nanocomposite to isolate the weight percentage of carbon nanotubes in the nanocomposite. It includes a furnace in which the heat can be ramped up from 0.1 to 500 °C/min in a linear control. It is equipped with two gas selections (air and nitrogen) and includes a high-temperature platinum weighing boat which can withstand heating up to 1050 °C.

## 2.6.5 Scanning Electron Microscope

A scanning electron microscope (SEM) is a high-resolution microscopy tool used to image surface morphology in the nanometer range. It consists of an electron gun that shoots a beam of electrons towards a sample, magnetic lens to focus and deflect the beam, and various detectors to detect the radiation that is emitted from the sample. The sample emits secondary electrons, backscattered electrons, and X-rays. Secondary electrons (SE) are electrons that are found on the surface of the sample. They are freed by the interaction of the electron beam with the top of the sample, and have low energy. Thus, they are used to create high-resolution images of the topography and surface of the sample. Backscattered electrons (BSE) are electrons from the electron beam that are scattered backwards from the sample after interaction. The electrons interact with the atomic nuclei deep within the sample, but their trajectories change and they are ejected from the sample, preserving their energy. Characteristic fluorescence X-rays are also generated upon the interaction of the electron beam with the sample, which yields elemental composition of the sample [89]. As a result, most SEMs are equipped with a energy-dispersive X-ray (EDX) detector for this analysis. In this work, a Hitachi S-4800 Field-Emission SEM (FESEM) was used to image the carbon nanotube network of a CNT-thermoplastic nanocomposite. An FESEM differs from a regular SEM in the generation of the electron beam. A regular SEM uses thermionic emission to accomplish this, while an FESEM uses a potential gradient and a field-emission gun. The result is that the FESEM generates a more focused beam, which results in a higher resolution and thus higher possible magnifications.

## 2.6.6 Keithley Sourcemeter

The electrical characteristics of the transistor devices in this work were measured by a Keithley 2612B semiconductor parametrizing sourcemeter. The system is capable of applying voltage and current sweeps while measuring voltage and current. The

sweeps the sourcemeter is capable of performing include  $I_D$ - $V_D$ ,  $I_D$ - $V_G$ , and logic gate input/output sweeps. The sourcemeter is controlled by custom Labview programs that are capable of changing the parameters of these sweeps, such as drain and gate voltage, voltage and current step size, and time delay.

## 2.7 Hydrogels

Hydrogels are polymeric network materials that are created by cross-linking polymer chains with any sort of aqueous medium, forming a water-swollen gel material [90, 91]. They may be categorized according to multiple criteria such as method of preparation (i.e homopolymer vs copolymer), the net ionic charge contained in the gel (i.e neutral vs anionic), the physiochemical structural features of the network (i.e amorphous vs semicrystalline), and the secondary forces holding together the networks (i.e. hydrogen bonds and affinity complexes). Hydrogels have been found to be useful in a variety of contexts such as biomedical applications, nanomedicine, and biosensor devices [91–93]. Due to their biocompatibility and compatibility with various materials and substrates, hydrogels have gained attention in recent years, especially in bioelectronics and devices [93]. Other attractive features of hydrogels include high hydrophilicity, high fluid absorption, and excellent elasticity/stretchability. Examples of popular hydrogel mixtures include poly(vinyl alcohol) (PVA), poly(ethylene glycol) PEG, and gelatin hydrogels. In this work, hydrogels have been used in the structure of OECT devices. Hydrogels have been recently been used in OECTs as part of functionalization layers as well as completely replacing the liquid electrolyte layer [83, 94]. The advantage of using hydrogel layers is that they remove the need for dropping a liquid electrolyte on an OECT device in order to test it. They can also absorb a large amount of liquid due to their porous nature [93]. On the other hand, this may also hinder device performance when considering device speed, as ions must permeate through the entirety of the hydrogel before reaching the channel, lowering the speed of operation.

In this work, a gelatin hydrogel was used in combination with ionic solution in order to remove the need for dropping electrolyte on two devices in a logical inverter gate based on OECTs. A gelatin hydrogel was also mixed with 1xPBS solution and used as encapsulation layer in order to immobilize other functionalization layers on an OECT device. The hydrogel prevents the washing away of enzymes required to detect specific molecules which are outlined in Chapter 4. In the case of the encapsulation hydrogel, the layer also improves biocompatibility by acting as a separation layer between the multiple layers of functionalization materials and the liquid that is being sensed. In a real-world application, this would ensure that no unexpected transfer of unwanted materials would occur. For example, functionalization materials would not permeate into a wound when sensing wound fluid.

# Chapter 3

## Aerosol Jet 3D-Printed Temperature Sensor Based on Multi-Walled Carbon Nanotubes

### 3.1 Introduction

In the biosensing industry, there is an increasing need for cheap, flexible temperature sensors. Flexible electronic sensors have become increasingly popular in recent years [8, 9] with the emergence of wearable electronics [2, 3]. Electronic sensors can also be integrated with larger Internet of Things (IoT) systems for faster data analysis and transmission. Flexible sensors allow for easier conformation of the sensing element to the skin, allowing for more efficient sensing parameter transfer and greater patient comfort [3, 95]. Skin temperature sensing is important in many contexts, mainly the medical field. Skin temperature is measured extensively in hospital patients, and can be indicative of various diseases, illnesses, and general inflammation [11, 96]. To be useful, temperature sensors used for these purposes should be small, non-invasive, and comfortable for the patient to wear.

In recent years, carbon nanotubes (CNTs) have been studied extensively by the scientific community due to their excellent mechanical, thermal, and electronic properties [97–99]. In particular, CNTs may act as semiconducting or metallic materials based on their chirality and geometry [100]. CNTs can be either single-walled or

multi-walled, meaning they consist either of one hollow cylinder or multiple cylinders nested within each other. Multi-walled carbon nanotubes (MWCNTs) have been studied as temperature sensors when combined in the form of nanocomposites with various thermoplastics [101, 102]. MWCNTs intrinsically change their resistance based on temperature [103, 104], an effect that is compounded by combining them with a thermoplastic. As these kinds of nanocomposites are heated, they expand and change the orientation of the network by bringing more CNTs into contact with each other, lowering the resistance of the material. Percolation theory has been extensively studied in CNT nanocomposites with low percolation thresholds being achieved due to the network structure and conductivity of CNTs [105, 106]. As shown in Figure 3.1, the initial resistance of a CNT nanocomposite device is determined by its concentration of CNTs in the polymeric matrix. If a device is fabricated with a CNT concentration at or near the percolation threshold, thermal expansion of the nanocomposite film could bring the device in and out of the conducting and insulating regimes, triggering a large resistance change with a small temperature change. Since the percolation threshold is different for each kind of CNT, the optimization of CNT filler concentration is crucial for the development of a working sensor. Mohiuddin and Hoa studied the effect of MWCNT weight ratio in a MWCNT/poly ether ether ketone (PEEK) composite and observed a conductivity change of 7 orders of magnitude when changing CNT concentration from 3 to 4 wt%, with a percolation threshold of approximately 3.54% [107].

Optimization of CNT concentration along with the resistance properties of CNT nanocomposite films have been studied [108, 109], but few full biosensors or biosensing systems have been reported using CNT nanocomposites as the sensing material for temperature sensing. A temperature sensor based on a MWCNT and poly(styrene-*b*-(ethylene-co-butylene)-*b*-styrene) (SEBS) nanocomposite has been demonstrated by Salvo et al. which displays high sensitivity ( $85 \Omega/^{\circ}\text{C}$ ) and linearity ( $R^2 > 0.999$ ) [78]. However, to the best of our knowledge, these kinds of devices have not yet

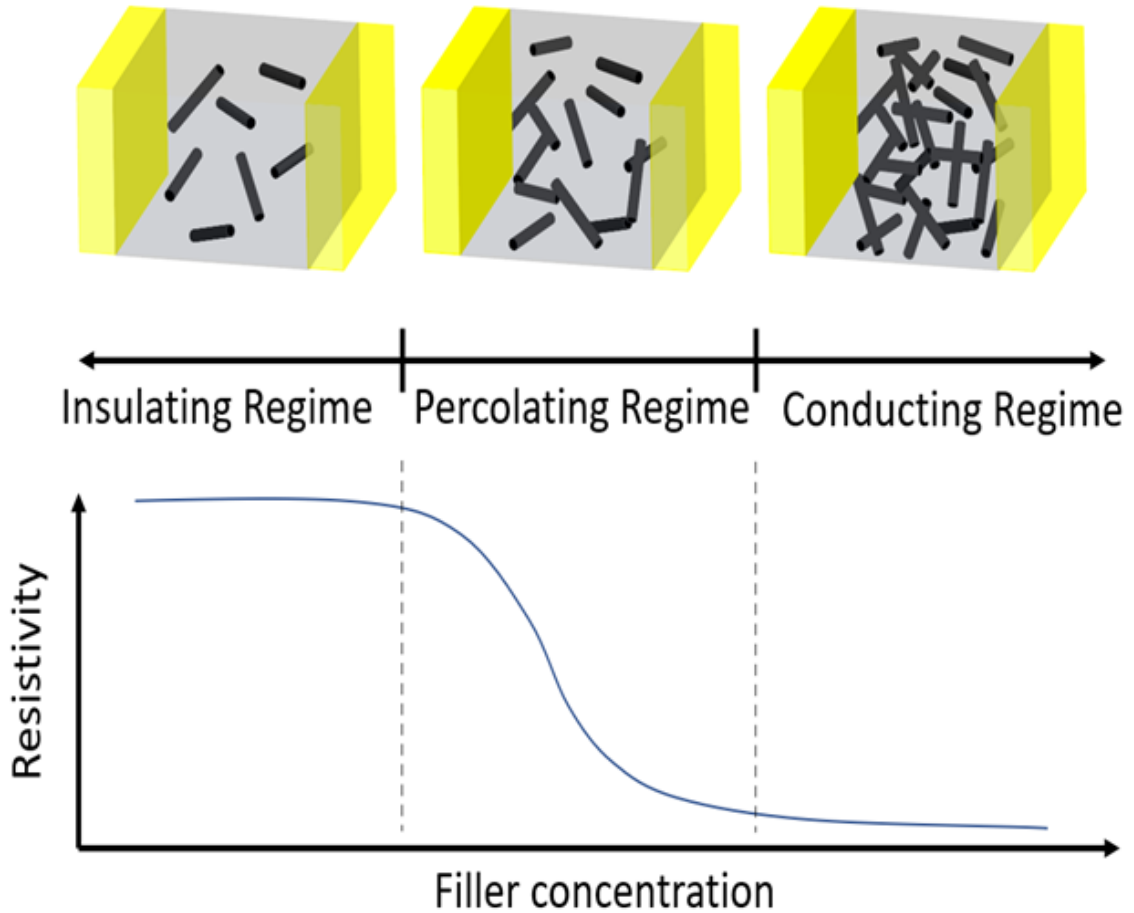


Figure 3.1: Resistivity of a percolating network versus the concentration of the filler material. As the concentration increases, nodes of the material – in this case carbon nanotubes – begins to form conductive pathways, resulting in a sharp increase in conductivity and decrease in resistivity.

been demonstrated for skin measurements. Due to the simplicity of a resistance measurement, these kinds of sensors can be integrated with larger biosensing systems with minimal circuit overhead.

In this work, we demonstrate an aerosol jet 3D-printed temperature sensor based on a MWCNT/SEBS nanocomposite. 3D printing allows for fast prototyping of various designs as well as the ability to easily print electronic devices on flexible substrates. The aim of the work is to realize small, economical, reliable and repeatable sensors that are highly sensitive in the temperature range of 30-40°C for the eventual end use of skin temperature measurement. We believe that this kind of device could be

successfully applied for skin sensing for a variety of medical applications.

## 3.2 Materials and Methods

The sensor was developed on a polyimide (Kapton®) substrate to achieve high flexibility. For biosensing, conformability of a sensor to skin is important for biosensing performance and patient comfort. For these reasons, aerosol jet 3D printing was used to deposit gold electrodes on polyimide. The nanocomposite dispersion was prepared and drop casted onto the electrodes. Finally, a flexible printed circuit board (PCB) was designed as a connector board for interfacing with an external circuit. One side of the connector board was used to insert the polyimide sensor, while the other was used to connect a flat-flex cable (FFC) which led to a measurement circuit. Together, the PCB connector board with the inserted flexible biosensor (Figure 3.2 (a)) provide a robust platform for skin sensing that can be easily attached to any surface while maintaining high performance and accurate results.

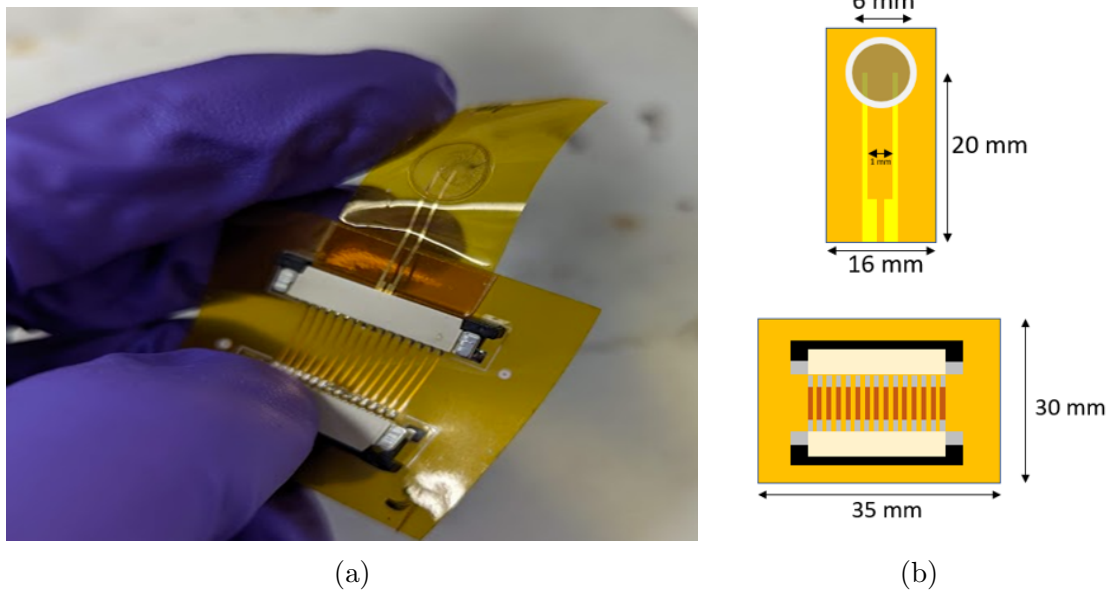


Figure 3.2: (a) The finished flexible sensor inserted in the PCB connector board via ZIF connectors. (b) (Top) 2D view and dimensions of the 3D printed and drop casted sensor on polyimide substrate. (Bottom) 2D view and dimensions of the connector board.

### 3.2.1 Aerosol Jet Printing

An Optomec Aerosol Jet 5X 3D printer was used to deposit gold tracks onto polyimide substrate (thickness 1 mil). Gold nanoparticle ink (UTDOTS, UTDAu40 TE) was loaded into an ultrasonic atomizer and deposited under an N<sub>2</sub> sheath gas flow of 30 ccm and an atomizer gas flow of 25 ccm. The electrodes were spaced apart at a pitch of 1 mm with a trace width of 300  $\mu\text{m}$  (Figure 3.2 (b)). Additionally, the bottom of the sensor was designed to be insertable into a zero-insertion force (ZIF) connector. To achieve this, the gold was printed in a land pattern with the appropriate pitch and length to provide adequate contact with the ZIF connector. The approximate thickness of the deposited gold was 1  $\mu\text{m}$ . After deposition by printing, the gold electrodes were annealed on a hot plate at 280°C for 1 hour.

After gold deposition, polyimide (UTDOTS, PI-AJ) was printed at the top of the sensor in a circular well pattern. Since the nanocomposite dispersion was drop-casted, the well was used to contain the radial spread of the dispersion and to maintain a uniform film for accurate characterization. The polyimide was deposited under an N<sub>2</sub> sheath gas flow of 60 ccm and an atomizer gas flow of 27 ccm. The 500  $\mu\text{m}$  wide walls of the well along with their 6.5  $\mu\text{m}$  thickness contained the nanocomposite effectively to achieve consistent nanocomposite film area (36 mm<sup>2</sup>) and thickness measurements ( $\sim$ 0.7  $\mu\text{m}$ ). After polyimide deposition, the substrate was annealed once again on a hot plate at 130°C for 1 hour and 30 minutes.

### 3.2.2 Nanocomposite Dispersion Preparation

Nanocomposite dispersions were prepared and drop casted onto the substrates with printed gold and polyimide. The nanocomposite was not printed mainly due to the difficulty in printing the dispersion. Characterizing an ink for aerosol jet printing and optimizing its printing parameters is a time-consuming process if not bought as an ink explicitly made for aerosol-jet printing. There are carbon nanotube inks available which have been reported in the literature with printing parameters [110, 111], but

none that have included any sort of thermoplastic in their composition. Additionally, the multi-walled carbon nanotubes (MWCNT) used had an average length of 10  $\mu\text{m}$ , which is greater than the average size of an aerosol droplet for our printer (1  $\mu\text{m}$ ). This would result in lower and non-uniform deposition as the carrier gas would not be able to push enough aerosolized ink through the deposition head.

The nanocomposite dispersion was obtained by dissolving poly(styrene-*b*-(ethylene-co-butylene)-*b*-styrene) (SEBS) bought from Sigma-Aldrich (200565-250G) in toluene and then adding the MWCNTs (Sigma-Aldrich, 698849-1G). The MWCNTs had an average length of 10  $\mu\text{m}$  with an average outer diameter of 12 nm. The mixture was sonicated for 1 hour under a power of 110W and frequency 40 kHz. The resulting dispersion was then centrifuged for 30 minutes at 4000 rpm as carbon nanotubes tend to agglomerate in dispersion if left for prolonged periods of time. To avoid further agglomeration, non-uniformity and evaporation of the dispersion, drop-casting was done directly after centrifugation. New dispersion was always created prior to drop-casting, with old dispersion having been discarded if not immediately used. For each 36  $\text{mm}^2$  polyimide well, 6  $\mu\text{L}$  of nanocomposite was drop-casted and left to dry for 1 hour. The substrate was annealed in an oven at 150°C for 4 hours, as this treatment improves linearity which was reported previously by Calisi et. al [112].

### **3.2.3 Material and Electrical Characterization**

Temperature sensing experiments were carried out using a hot plate with a temperature control of 0.1°C. Devices were inserted into a ZIF connector soldered onto a flexible connector board and taped down to the hot plate to ensure maximum heat transfer. A second on-board ZIF connector was used to connect an FFC cable which led to the measurement device (either a Fluke 289 digital multimeter or a Keithley 4200 Semiconductor Characterization System). Temperature was then swept in increments of 5°C from room temperature to 55°C and vice versa. Resistance was recorded 3 minutes after each temperature was reached to ensure adequate response time of

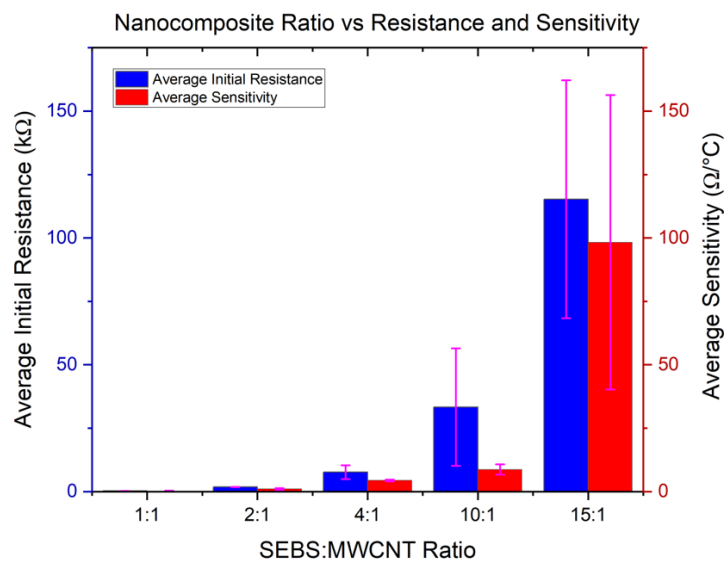
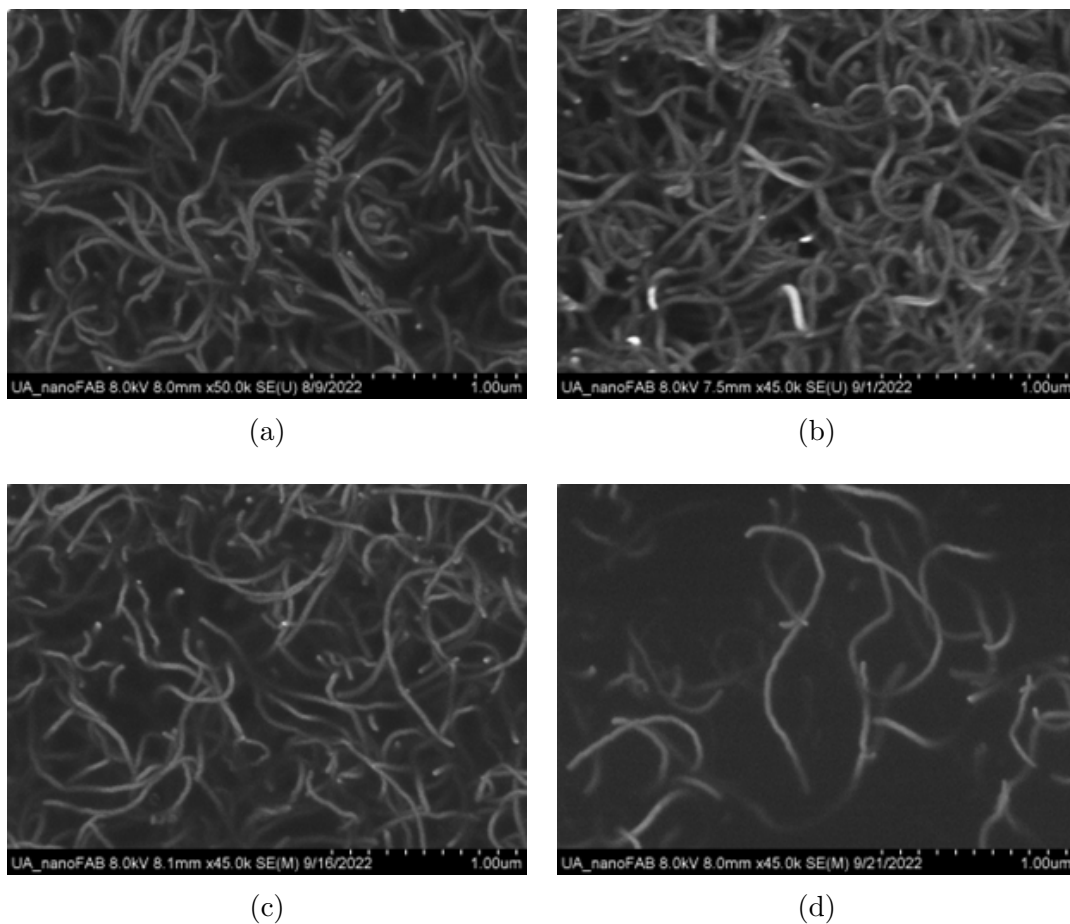
the sensor and to test robustness. The skin temperature testing was done using a similar test setup, but with resistance measured every 5 minutes over a 30-minute span while simultaneously taking a reference temperature measurement using an infrared thermometer. Scanning electron microscope (SEM) images were taken with a Hitachi S-4800 FESEM. Nanocomposite film thickness measurements were taken with an Alpha-Step IQ Profilometer. UV-vis spectrophotometry scans were taken using a Hitachi U-3900H Spectrophotometer. Thermogravimetric scans were carried out using a Discovery Thermogravimetric Analyzer.

### **3.3 Results and Discussion**

The discussion of the results will focus on two aspects: the nanocomposite film properties and the performance of the final sensor. The aerosol jet printing of the gold and polyimide layers is already an optimized process and will not be discussed.

#### **3.3.1 Nanocomposite Weight Ratio Optimization**

The most crucial optimization parameter for the nanocomposite film was the selection of the SEBS to MWCNT ratio when mixing and dispersing the nanocomposite in toluene. The SEBS weight was kept constant at 0.5g in 100 mL of toluene, while the MWCNT concentration was decreased at regular intervals until high sensitivity was reached. SEM images were taken for 4:1, 5:1, 10:1, and 15:1 SEBS to CNT weight ratios (Figures 3.3 (a)-(d)). When each nanocomposite was dropped and annealed on 3D printed devices, initial resistance measurements were taken. Sensitivity was extracted via heat test method outlined in Section 3.2.3. Figure 3.3 (e) outlines the average initial resistance and sensitivity for devices made with each weight ratio. It can be observed that resistance increases with CNT concentration decreases. The sensitivity also increases as the resistance increases, which is expected as the CNT concentration approaches the percolation threshold. The optimized weight ratio was found to be 15:1 which resulted in an average initial resistance of 100 k $\Omega$ .



(e)

Figure 3.3: FESEM images of the nanocomposite with 10  $\mu\text{m}$  nanotubes at SEBS:MWCNT ratios of (a) 4:1 (b) 5:1 (c) 10:1 (d) 15:1. (e) The relationship between nanocomposite weight ratio and initial resistance and sensitivity.

In Figure 3.3 (e), it can be seen that the variation and error of the average initial resistance and sensitivity increases dramatically as the ratio of SEBS to MWCNT increases. This is due to the random nature of the percolation network as the filler concentration of the matrix approaches the percolation regime. The optimal ratio was taken to be 15:1 for two main reasons. Firstly, the variation was becoming very large as shown by the error bars in Figure 3.3 (e) and consistent devices in the middle of the range were becoming more difficult to achieve. The devices were thus deemed to be within the percolation regime. Secondly, with less CNT concentration, the nanocomposite solution was also becoming more difficult to drop-cast due to lack of viscosity. Another reason that contributed to the decision that the 15:1 ratio was optimal was that large resistance values, such as those above  $1\text{ M}\Omega$ , were becoming difficult to measure with the digital multi-meter that was used for all measurements. Measurements were wildly fluctuating which is a limitation of the measurement method. This is also the reason negative temperature coefficients take into account initial resistance - low resistance measurements are less prone to fluctuation and are generally more accurate.

Although the percolation threshold can be explicitly found by comparing resistance-frequency plots for different weight percentages of CNT, this was not done in this work and only estimated. One reason for this was that some devices made with a 15:1 ratio included resistances that reached higher than  $1\text{ M}\Omega$ , which can be taken as insulating for the purposes of a resistive sensor. This can be explained by the random nature of the orientation of the nanotube network. If the MWCNT ratio is at or very close to the percolation threshold, these random variations between individual devices may cause each device to have widely varying initial resistances. Thus, the weight ratio that results in the nanocomposite closest to the percolation threshold for our specific MWCNTs was taken to be 15:1. Furthermore, at lower concentrations of MWCNT, the drop-casted dispersion was quickly becoming thinner and harder to control. In future work, this could be improved by 3D printing the nanocomposite in addition

to the electrodes. A second reason for estimation of the percolation threshold was that since we are interested purely in the performance of the finalized device, the weight ratio was deemed to be adequately close to the actual percolation threshold as it indicated high sensitivity.

Since the percolation threshold depends on the type of MWCNT, the initial resistance and sensitivity of 1.5  $\mu\text{m}$  tubes (NANOCYL<sup>®</sup> NC7000<sup>™</sup>) was studied in comparison to the 10  $\mu\text{m}$  tubes (Figure 3.4). The average initial resistance was found to be much lower for a SEBS: MWCNT weight ratio of 5:1 at 418  $\Omega$  versus 4.12 k $\Omega$  for 10  $\mu\text{m}$  tubes. The sensitivity was also lower at 0.29  $\Omega/^\circ\text{C}$  versus 3.24  $\Omega/^\circ\text{C}$  for 10  $\mu\text{m}$  tubes. Together, these indicate a reduction of 90% for initial resistance and 91% for sensitivity. We speculate the reason for this to be in the improved quality of the network with the 1.5  $\mu\text{m}$  tubes which leads to more conductive pathways and lowered resistance. The shorter tubes allow for more individual CNTs per gram of powder which results in a greater amount of tube terminations. This would lead to greater interconnectivity and a more intricate network of pathways. Due to the increased sensitivity of the 10  $\mu\text{m}$  tubes, they were used in all subsequent devices and measurement.

Figure 3.5 shows the resistance vs temperature calibration curve of an optimized device taken by the same method outlined in Section 3.2.3. It can be seen that the sensor exhibits high linearity ( $R^2 > 0.99$ ) in both its forward and backwards sweep. This is due to the annealing treatment which has been reported to increase linearity but decrease sensitivity [78, 112]. Calisi et al. found that annealing MWCNT/SEBS nanocomposites at a temperature higher than the melting transition temperature of the ethylene-co-butene block (44 $^\circ\text{C}$ ) leads to a significant change in the percolation network [112]. Additionally, the percolation threshold is lowered due to a decrease in CNTs. In this work, non-annealed samples were not studied as annealing has been shown to increase linearity significantly [112]. Thus, the original (unoptimized) procedure already included an annealing step. Another important parameter for

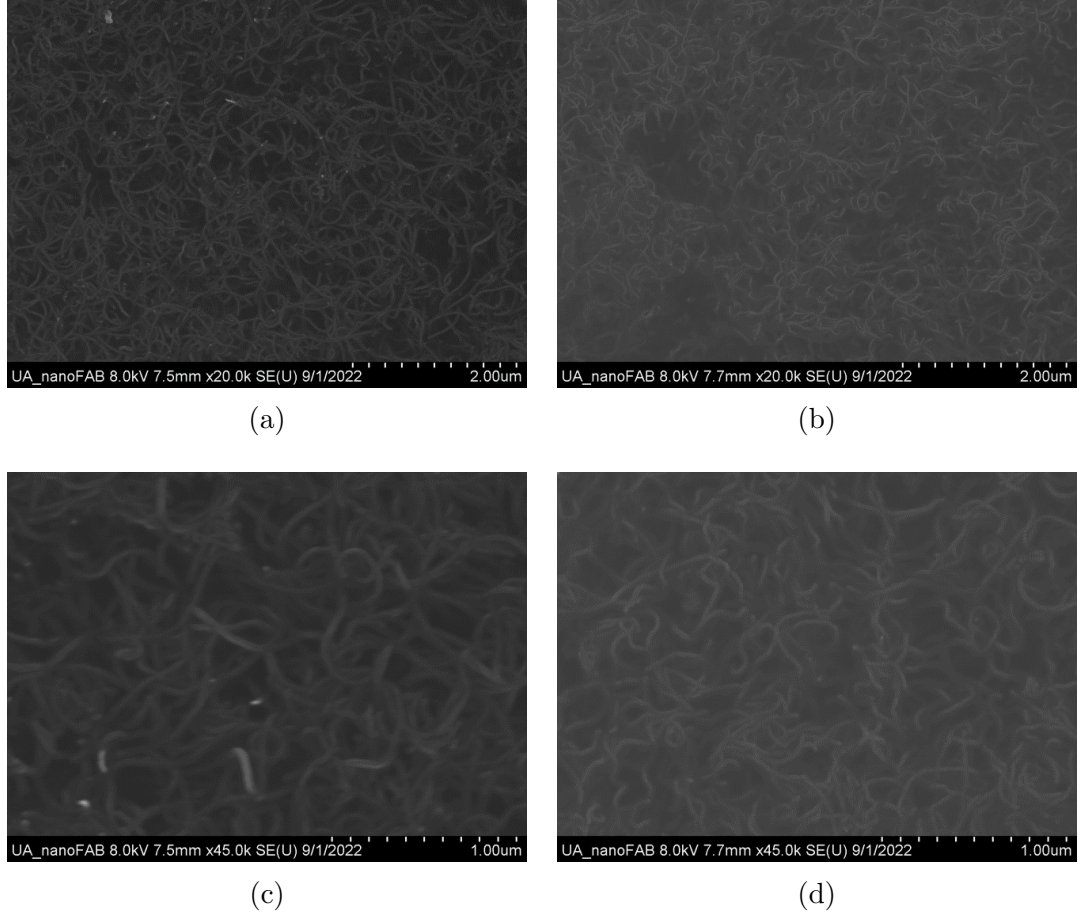


Figure 3.4: FESEM images of the nanocomposite with 10  $\mu\text{m}$  nanotubes at a SEBS:MWCNT ratio of 5:1 at (a) x20k magnification and (c) x45k magnification. For comparison, 1.5  $\mu\text{m}$  nanotubes at a SEBS:MWCNT ratio of 5:1 are shown at (b) x20k magnification and (d) x45k magnification.

a temperature sensor is the negative temperature coefficient (NTC), which can be extracted from the initial and final resistances and temperatures of the calibration curve, assuming a highly linear curve. This can be shown in Equation 3.1:

$$\alpha = \frac{R_f - R_0}{P} R_0 (T_f - T_0) \quad (3.1)$$

where  $\alpha$  is the temperature coefficient ( $\text{K}^{-1}$ ) (negative for this material),  $R_0$  and  $T_0$  are the original or reference resistance ( $\Omega$ ) and temperature ( $^{\circ}\text{C}$ ), and  $R_f$  and  $T_f$  are the final resistance ( $\Omega$ ) and temperature ( $^{\circ}\text{C}$ ) on the curve. Once the NTC is extracted, temperature can easily be calculated by measuring resistance of the final device at

any time and using Equation 3.2:

$$T = \frac{R - R_0}{\alpha R_0} + T_0 \quad (3.2)$$

Where  $R_0$  and  $T_0$  are the initial resistance ( $\Omega$ ) and temperature ( $^{\circ}\text{C}$ ) (taken usually at room temperature),  $R$  is the measured resistance ( $\Omega$ ),  $T$  is the corresponding temperature ( $^{\circ}\text{C}$ ) at the measured  $R$ , and  $\alpha$  is the negative temperature coefficient of the material ( $\text{K}^{-1}$ ).

The highest NTC of our devices was extracted with a 15:1 SEBS to MWCNT ratio and was found to be  $-0.00134 \text{ K}^{-1}$ . This corresponds to a sensitivity of  $237 \text{ } \Omega/^{\circ}\text{C}$ , which is around 2x higher than other reported work for these kinds of nanocomposite sensors [78, 113]. Although the NTC value is not as high as other commercial temperature sensors such as thermistors, the sensitivity value itself is quite high and is sufficient for measurement purposes. The NTC value takes into account the initial resistance, which is inherently high in our sensors due to the operating principle. However, with modern circuitry, higher resistance values are becoming easier to measure – this can be done for our sensors by interfacing with an external circuit using the flexible connector board shown in Figure 3.2. Another advantage of our sensor is that it displays high linearity, which is more desirable for measurement than the logarithmic curve of a thermistor.

The sensor also exhibits hysteresis in its resistance response as shown by the backward sweep in Figure 3.5. However, the back swept resistance curve also appears to be highly linear and deviates from the original forward sweep curve by a maximum of  $0.70 \text{ k}\Omega$  at approximately  $47^{\circ}\text{C}$ . In the desired temperature sensitivity range of  $30\text{-}40^{\circ}\text{C}$ , the hysteresis becomes noticeably less pronounced. The hysteresis is likely due to the intrinsic hysteresis present in the conductivity-temperature curve of carbon nanotubes. This kind of hysteresis has been observed in different nanocomposites such as CNT-PEEK [107], CNT- $\text{Al}_2\text{O}_3$  [114], and CNT-polystyrene nanocomposites [115].

However, Karimov et al. have demonstrated CNT temperature hysteresis in pure MWCNT films. Whether this is due to intrinsic material properties or the network of CNTs (outside of a nanocomposite) is still unclear. Furthermore, the hysteresis observed in multiple studies is inconsistent in that the backward temperature sweep results in both higher and lower resistance values than the original curve. For example, Karimov et al. demonstrate hysteresis in a pure MWCNT film with a return path that specifies a lower resistance at each temperature than the original curve [103]. In this work, the resistance increases on the cooling cycle. We speculate this is due to the expansion of the tubes in the heating cycle, where the tubes are re-oriented randomly and then agglomerate on the cooling cycle, resulting in less conductive pathways in the percolation network, leading to an elevated resistance.

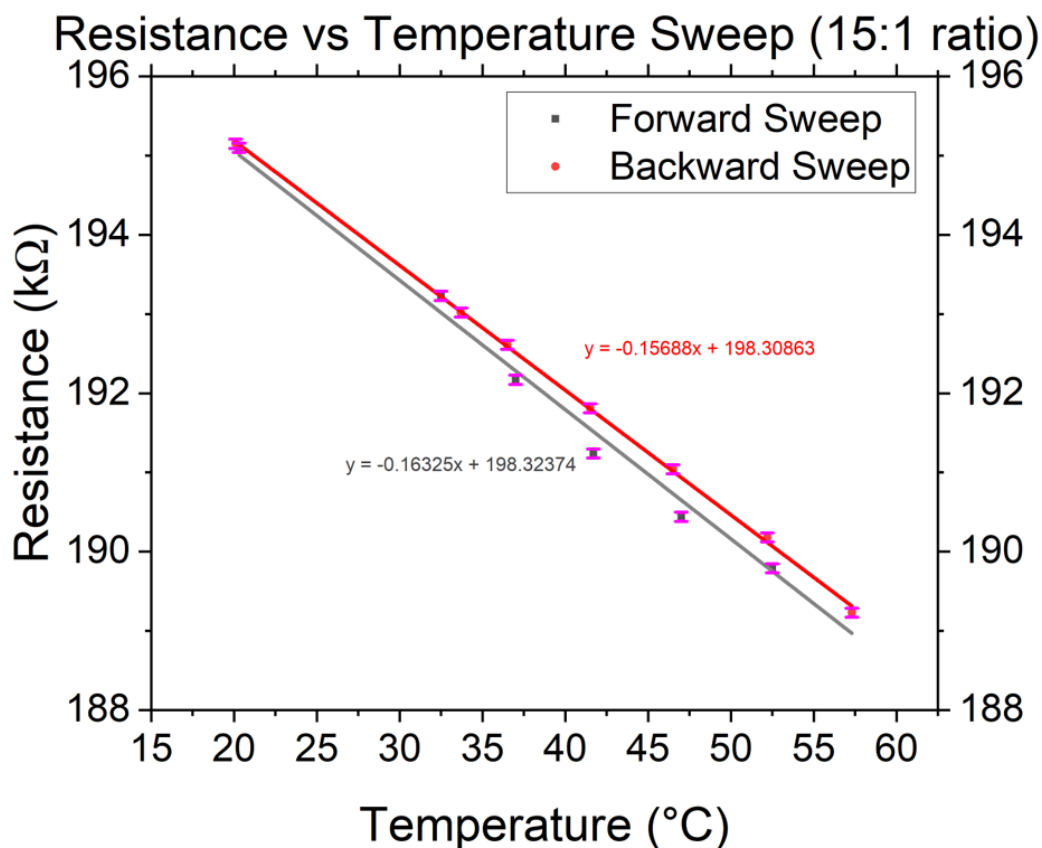


Figure 3.5: Resistance response of an optimized sensor (15:1 nanocomposite ratio) in a controlled environment (hot plate, no movement). The grey line indicates the resistance of the device when the temperature was increased, while the red line indicates the resistance when the temperature was decreased.

### 3.3.2 Nanocomposite Film Characterization

When drop casting the nanocomposite dispersion, it was critical to create a uniform film. Due to the random nature of CNT networks, consistency across multiple devices is difficult to achieve. CNTs tend to agglomerate because of high van der Waals forces which causes issues when considering the small area between electrodes for a temperature sensor. There is also the “coffee ring” effect to consider – when dispersions of CNTs are drop casted, the drying causes CNTs to accumulate at the edges of the film. The contact line between the dispersion and the substrate is fixed – thus, because the CNTs are still moving from the velocity of the drop cast, they

self-assemble on the perimeter of the film [103]. In this work, the coffee ring effect was observed. Thickness measurements were made by profilometer. For the final device, 6  $\mu\text{L}$  of dispersion were made to cover 36  $\text{mm}^2$  of sensor area. Thus, profilometer measurements were done on circular drop casts of the same amount of dispersion. There were two film thicknesses observed – one for the coffee ring perimeter and one for the flat uniform area on the inside of the ring. The thickness of the perimeter was approximately  $\sim 2$   $\mu\text{m}$  on average, while the thickness of the flatter inside area was approximately 0.6  $\mu\text{m}$ . Figure 3.6 (a) shows the coffee ring effect for different drop casts of varying volume on 5 mil polyimide substrate. It can be seen that there is a clear dark ring around the outside of the drop cast where the CNTs have concentrated. To help mitigate the consequences of this effect, a polyimide well was printed in a circular pattern at the top of the sensor where the CNT-gold interface is found. After drop-casting the nanocomposite onto devices with the printed well, the CNT coffee ring was found to concentrate on the edge of the PI well, leaving a uniform film inside the enclosed area, and more importantly, in the area between electrodes. This method resulted in more consistent initial resistance readings. Additionally, it helped avoid the random spread of the nanocomposite. Raising the SEBS:MWCNT ratio resulted in a less viscous dispersion which spread over more electrode area than expected, which led to higher variation in resistance readings. The PI well allowed us to fix the contact area for consistent testing.

To further confirm the uniformity of the film area inside the well, UV-vis measurements were carried out. Due to the difficulty in applying the UV-vis laser on different locations of the 36  $\text{mm}^2$  sensor area, a glass wafer was used instead. After drop casting 5 mL of dispersion on the glass wafer, a similar film was observed with a uniform inner area with a dark perimeter ring. The UV-Vis spectra was measured at 4 locations which are shown in Figure 3.6 (b). The corresponding UV-vis spectra is shown in Figure 3.6 (c) and is in line with spectra in other reported work [116]. Originally, consistent results were difficult to achieve due to the non-uniformity of the

film. After optimizing the measurement procedure with the glass wafer, Figure 3.6 (c) shows that the curves are virtually identical for each of the four different positions. The difference in maximum absorbance value can be attributed to different types of CNTs used and in different concentrations. In general, the film was confirmed to be quite uniform in the area inside the perimeter and suitable for use in a sensor.

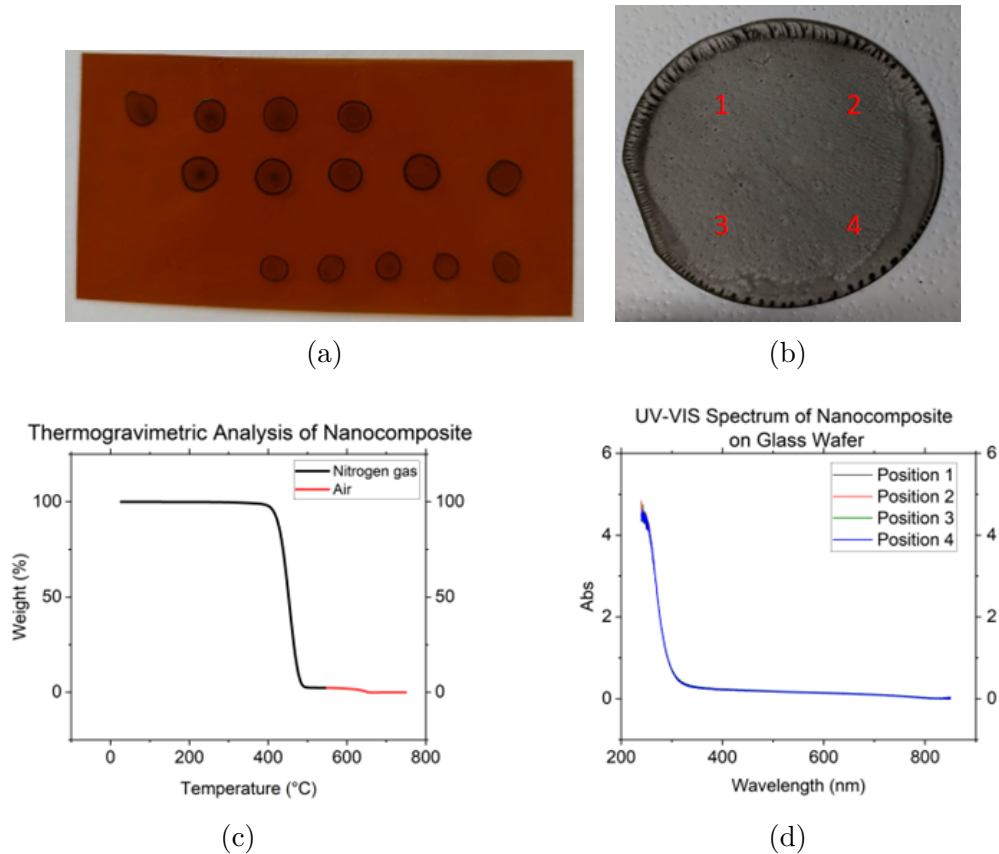


Figure 3.6: (a) Nanocomposite drop-casts of varying volumes on 5 mil Kapton with a pronounced coffee ring.(b) UV-vis spectra of nanocomposite dropped on glass wafer at various positions of the wafer. The area of the glass wafer from which the nanocomposite sample was taken is indicated by the inside of the circle in (d). (c) Thermogravimetric analysis of the nanocomposite dropped on glass wafer was conducted with the results. (d) The positions (1-4) at which the UV-vis spectra were measured.

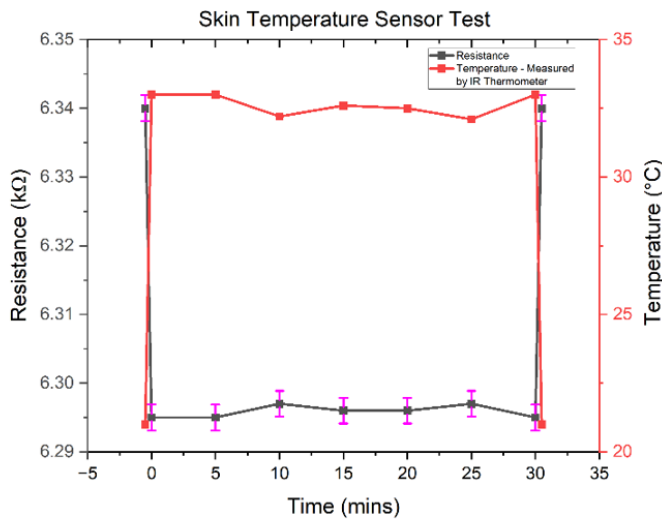
To confirm the weight percentage of the CNTs in the nanocomposite, thermogravimetric analysis was used. As in the UV-vis measurements, non-uniformity of the film was an issue for obtaining consistent results. In one sample, TGA measurements indicated a higher concentration of CNTs when the MWCNT amount was actually

lowered. This was due to the method of collection - the nanocomposite was drop casted on glass slide, scraped off, and loaded onto a weighing boat. However, agglomeration of the CNTs allowed larger concentrations of CNT to be included in the final sample which heavily skewed results. To achieve more consistent samples, the same nanocomposite from the UV-VIS measurements were used. After UV-VIS measurements were conducted, the nanocomposite was taken from the circular area indicated in Figure 3.6 (b). This method resulted in much more consistent and lower weight percentages in line with the literature [105, 106]. The weight percentage of CNTs observed from the 15:1 SEBS to MWCNT ratio nanocomposites was approximately 2.5% on average. Figure 3.6 (d) shows the TGA sweep of one 15:1 sample – at approximately 400°C the SEBS is evaporated and swept out of the chamber, while the CNTs remain. The remaining CNTs are purged at 550°C when the purge gas is switched to air from nitrogen. This is indicated by the color change on the curve. The flat area between approximately 450 and 550°C indicates 2.5% CNTs. This was estimated to be the percolation threshold for the specific MWCNTs used in this work.

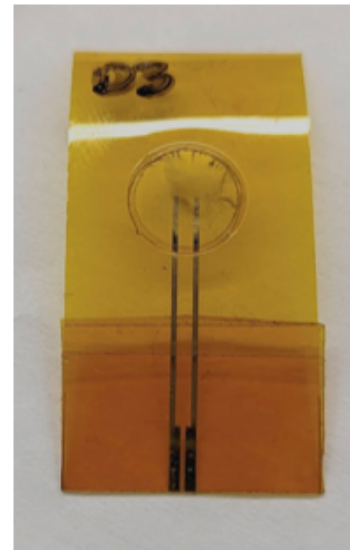
### **3.3.3 Skin Temperature Measurement**

A preliminary sensor design (4:1 SEBS to MWCNT ratio) was used to measure the skin of the author to provide a proof of concept for the working of the temperature sensor prior to optimization of the design. The results are shown in Figure 3.7 (a). The temperature was originally taken off skin at room temperature and then secured on skin, with measurements taken every 5 minutes. At the conclusion of 30 minutes, the sensor was taken off skin and measured in the air at room temperature after 30 seconds. Each point had a reference measurement of the skin taken by an infrared thermometer to correlate temperature changes with resistance response. As indicated by the initial and final points, the sensor has excellent response to changes in temperature. The average response time for resistance stabilization after the sensor was switched from ambient room temperature to skin temperature and vice versa was

approximately 15 seconds, a value which has not been reported in the literature to the best of our knowledge. This may be due to the thin layer of Kapton substrate (1 mil) which allows for faster heat transfer from the surface to the nanocomposite film. On the skin, the sensor also demonstrates adequate stabilization, as neither the temperature or resistance fluctuate. Any skin temperature fluctuations are accompanied by slight resistance fluctuations in the expected direction (as temperature increases, resistance decreases and vice versa). Overall, there is a clear distinction between the ambient room and skin temperatures, which confirms the correct operation of our sensor. The sensor stability over time also makes this an excellent candidate for skin temperature sensing.



(a)



(b)

Figure 3.7: (a) The results of the skin temperature measurement. The first and last points are taken roughly 30 seconds before and after the 30-minute-long skin test and indicate the resistance of the device in the ambient room temperature (off-skin). (b) An encapsulated device with a comparatively opaquer circular area at the top sensing area of the device.

The repeatability of the sensor was also tested using the same type of skin test. This is shown in Figure 3.8. The sensor was repeatedly placed on skin and taken off multiple times in a span of 30 seconds. It can be seen that the sensor features quick

response time as well as a tendency to return to its correct start and end points which correspond with the temperature of the ambient air and the temperature of the skin. As with all measurements with this type of sensor, minor fluctuations are present. However, these are likely due to fluctuation in the temperature itself, rather than error present in the measurement method, as even minor temperature fluctuations are present in the ambient environment surrounding the skin and sensor due to air movement. It has been observed with these sensors that even slight movement of air is enough to change the temperature and thus the resistance of the sensor due to high sensitivity.

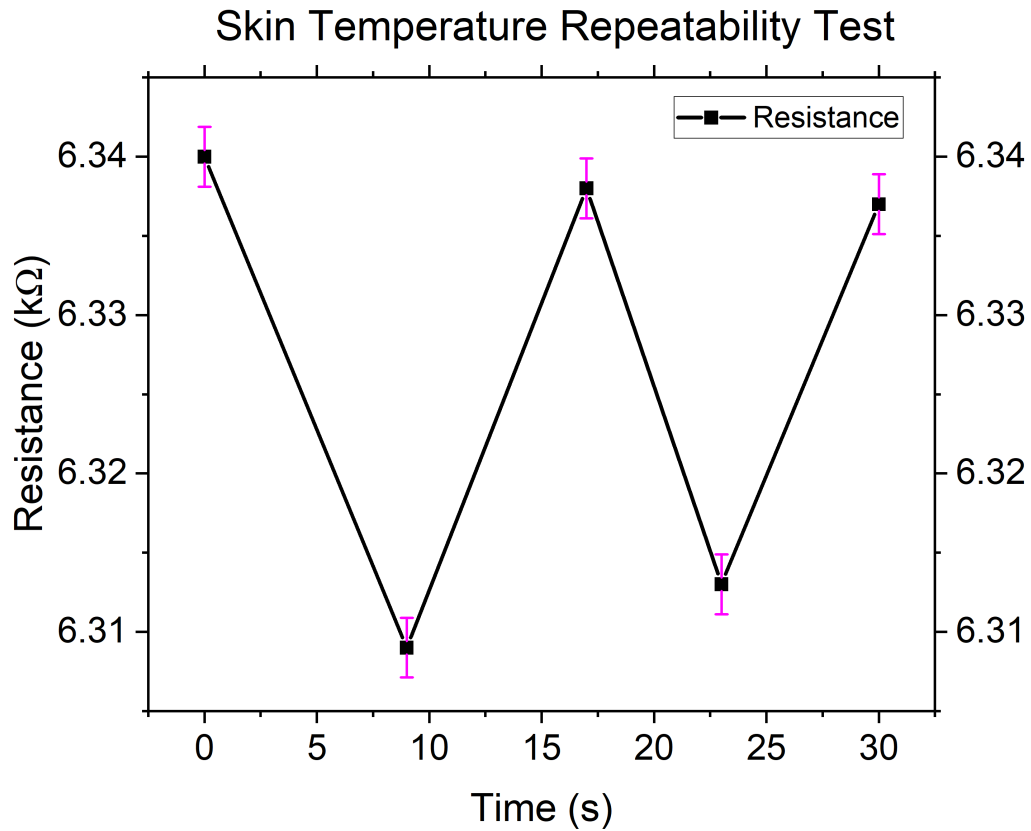


Figure 3.8: The skin temperature repeatability test. The higher points correspond to the sensor reading in ambient air, while the low points correspond to the reading when the sensor was placed on skin.

Due to their novelty, the health impacts of carbon nanotubes at human bio-

interfaces are not yet well understood [117–119]. Signs of carbon nanotube-based toxicity has been found in different biological systems in the human body [119], which indicates potential biological incompatibility. Skin sensing provides the potential for harm to a patient because of proximity to various bio-interfaces. For example, skin testing near an open wound could provide a direct pathway into the bloodstream for CNTs. For this reason, we have studied the effects of a polyimide encapsulation layer aerosol-jet printed over the top of the nanocomposite film in a circular pattern (approximately 1.5  $\mu\text{m}$  thick). Figure 3.7 (b) shows such a device which shows an opaquer sensing area with the polyimide encapsulation than a non-encapsulated device (Figure 3.2 (a)). Resistance-temperature sweeps were taken with encapsulated devices to compare with non-encapsulated devices (15:1 SEBS to MWCNT ratio). It was found that out of 7 devices, each device had its initial resistance decreased by an average of 26.47  $\text{k}\Omega$ . The sensitivities were also decreased by an average of 10.84  $\Omega/\text{C}$ . Together, these represent a 25% decrease in initial resistance and 20% decrease in sensitivity. This was likely due to the extra annealing time of the polyimide ink, which is 90 minutes at 130°C. Other studies have found that annealing MWCNT/SEBS nanocomposites decreases sensitivity but increases linearity and stability [78, 112]. Although the polyimide encapsulation decreases sensitivity, the sensors are still highly sensitive in the 30-40°C range for measurement purposes, while protecting the user or patient from potential harmful effects of carbon nanotubes. An example of a device that has had its sensitivity and initial resistance reduced by an encapsulation layer is shown in Figure 3.9. It is also worth noting that the Kapton substrate our devices are printed on has high thermal conductivity - this allows us to place the sensor on skin with the side with the sensing layer facing upwards and away from the skin. This adds an extra layer of protection against any potential harmful effects.

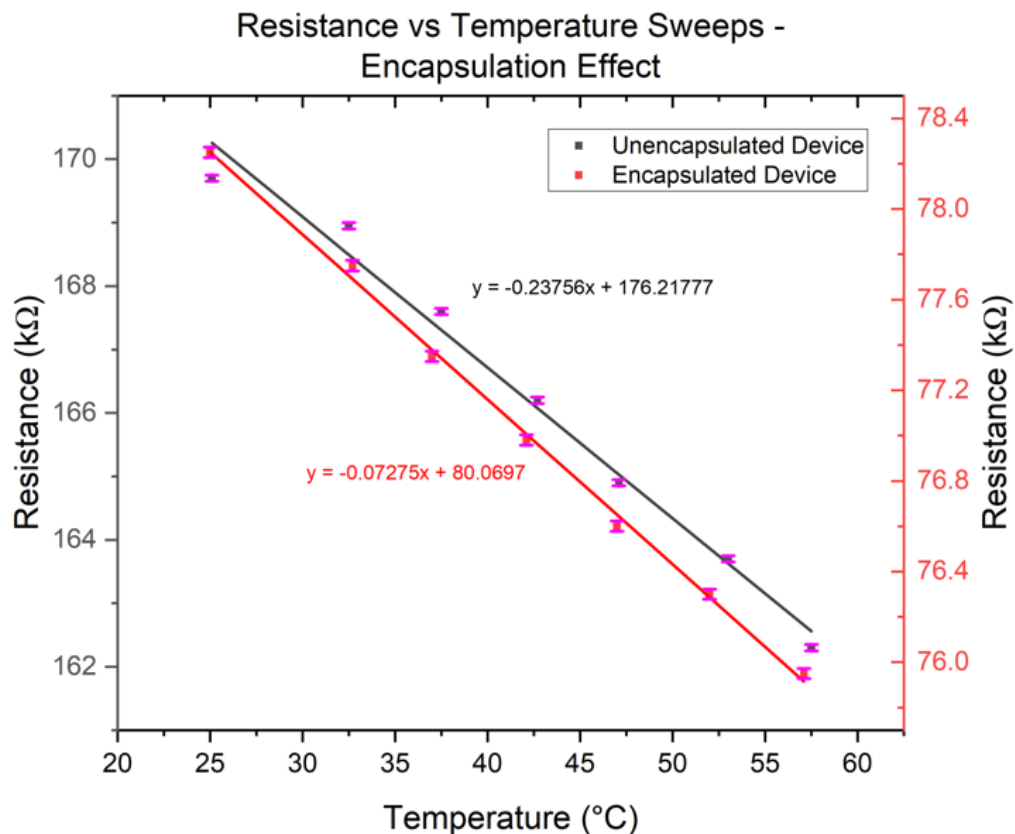


Figure 3.9: Resistance response of a sensor pre and post-encapsulation. The sensitivity has dropped from  $237 \Omega/^\circ\text{C}$  to  $72 \Omega/^\circ\text{C}$ , corresponding with a decrease in initial, room-temperature resistance.

### 3.3.4 Mouse Testing

As part of a larger project that aims to incorporate multiple sensors on one biosensing platform, the sensors outlined in this chapter were tested on live animal models - specifically, healthy and diabetic mice. The ethics approvals of the larger project included the sensors present in this chapter. The work aims to analyze various biomarkers in diabetic wound fluid in order to detect infections in the wounds and prevent amputations. Temperature of the skin surrounding the wound can also be used as a correlation marker for other analytes such as glucose, lactate, and pH levels. Thus, the skin of both healthy and diabetic mice was monitored in a similar fashion to the author’s skin temperature measurement in Section 3.3.3. A mouse skin temperature

test for both a healthy and a diabetic mouse is shown in Figure 3.10. It can be seen that the diabetic mouse displayed a lower average skin temperature than the healthy mouse at approximately 27°C compared to the healthy mouse at approximately 32°C.

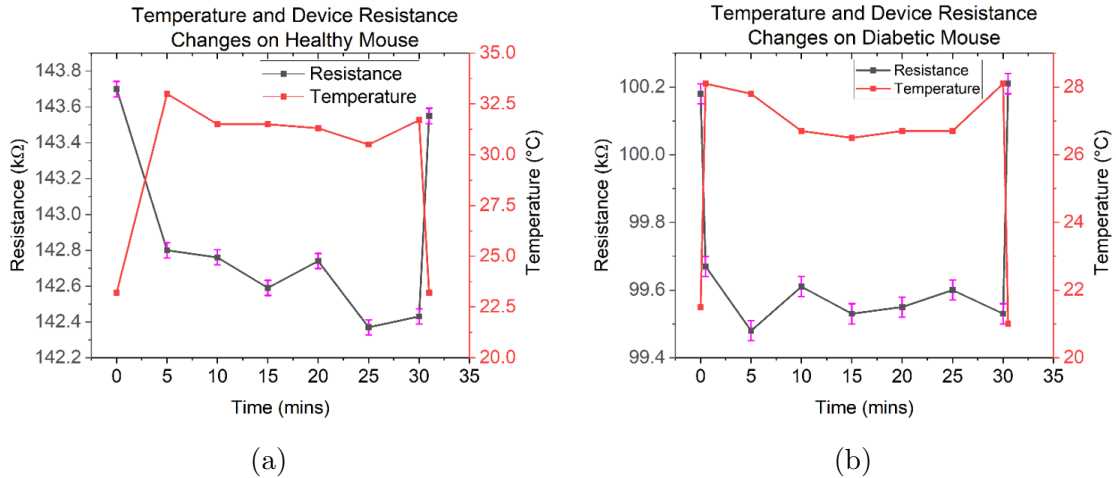


Figure 3.10: Skin temperature measurements for both a (a) healthy and (b) diabetic mouse. The first and last points are taken roughly 30 seconds before and after the 30-minute-long test and indicate the resistance of the device in the ambient room temperature (off-mouse).

As evidenced by the skin testing experiments in this section and the previous section, the temperature sensor performs as expected in a variety of contexts - as temperature of the sensor material increases, the resistance decreases and vice versa. The resistance change is also highly sensitive. Earlier in the chapter, sensors were tested only on hot plates in a lab setting. The results in this section and the previous section confirm that the sensor can be used in real-world applications for analysis. For example, the data extracted in this chapter will be used for diabetic wound analysis as part of the larger project mentioned previously.

### 3.4 Conclusion

Temperature sensor devices were fabricated using a combination of aerosol jet 3D printing and drop-casting. Nanocomposite dispersion weight ratio and procedure was optimized, resulting in a  $\sim 2.5\%$  weight ratio, confirmed by thermogravimetric analy-

sis, which was estimated to be the percolation threshold (at a SEBS:MWCNT ratio of 15:1). Devices made from optimized nanocomposite demonstrated high linearity in the range of 20-55°C ( $R^2 > 0.99$ ) with a maximum sensitivity of 237  $\Omega/^\circ\text{C}$ , which corresponds to a negative temperature coefficient of  $-0.00134 \text{ K}^{-1}$ . High linearity and sensitivity were demonstrated in both forwards and backwards temperature sweeps of the same device with minimal hysteresis shown in the range of 30-40°C. Effects of using shorter MWCNTs were also explored – reducing the average nanotube length from  $\sim 10 \mu\text{m}$  to  $\sim 1.5 \mu\text{m}$  resulted in a 90% reduction in initial resistance and 91% in sensitivity due to the enhanced percolation network which likely lowered the percolation threshold. Characterization of the film revealed that uniformity of the film was an issue due to the “coffee ring” effect. Polyimide drop-casting wells were 3D printed onto the sensor to mitigate this effect and achieve a film with higher uniformity as confirmed by UV-vis measurements. Skin temperature measurements were also successfully demonstrated with a response time of  $\sim 15$  seconds and minimal resistance fluctuations at a stable temperature over the course of a 30-minute-long test. In order to mitigate the risk of potential harmful effects of CNTs on the human body, the effect of a polyimide encapsulation layer 3D printed over the nanocomposite film on the performance of the devices was studied. It was found the encapsulation layer led to a decrease in initial resistance for all devices, resulting in an average sensitivity decrease of 20%. Finally, testing of the sensor was carried out on live animal models in order to gain insight into temperature changes of healthy and diabetic mice. The results confirmed that the sensor could be used as a sensor on live animal models.

The ease of fabrication of these flexible devices, coupled with the demonstrated lab and skin temperature testing results, indicate CNT/thermoplastic nanocomposites as excellent candidates for non-invasive skin temperature sensing. Future work will focus on 3D printing the nanocomposite itself as a means to achieve greater uniformity in film thickness as well as distribution of nanotubes.

## Chapter 4

# Aerosol Jet 3D-Printed Depletion Mode Logic Gates for Ion Sensing

### 4.1 Introduction

In recent years, logic gates built using organic semiconductor devices have gained significant attention [120–122]. Specifically, logic gates built using organic electrochemical transistors (OECTs) have been studied extensively mainly due to their low operating voltages [18, 83, 123]. The operating principle of an OECT is described in the background chapter. Logic gates have rarely been used as biosensor devices, however [18]. Because OECTs change their threshold voltage based on the concentration of ion or analyte in the electrolyte solution, their switching behavior changes based on this concentration as well. This can be exploited in the design for a logic gate biosensor. The advantage of a logic gate based sensor is mainly in the measurement method. The operating principle of a logic gate, as described in the background chapter, results in the output of a voltage level of "1" or "0". Due to the measurement of a voltage rather than a current, measurement is simplified and less prone to noise because of the intrinsic amplification in a transistor device. Most OECT-based sensors are current-sensing devices, which require more sophisticated circuitry. Another advantage of a logic gate based sensor is the inclusion of a reference level. In a NOT gate, two transistors are used - thus, in an OECT logic gate-based sensor, electrolyte must be included or dropped on two devices. Because of this, one OECT may be used

as a "sensing" device with a varying concentration in its electrolyte, while the other electrolyte is maintained at a known reference concentration. This simplifies data processing and can be used to create larger systems where a concentration can be isolated by analyzing the voltage output of multiple logic gates, each with a different reference concentration.

In this chapter, NOT gates based on OECT devices are built using aerosol jet printing and analyzed. Due to the difficulty of finding suitable n-type organic semiconductors, this chapter focuses on logic gates built only with a p-type semiconductor, PEDOT:PSS, as its channel material. These OECT devices operate in the depletion mode and require a modification of the traditional design to operate in a NOT gate configuration. Individual characterization of the devices is shown as well as the input/output behavior of the NOT gate circuit. Additionally, the effect of different concentrations of ions in the electrolyte solutions is shown (with different types of solutions as well). This is done to showcase the performance of the NOT gate circuit as a biosensor. To further improve upon the feasibility of this type of device as a biosensor, the effect of a hydrogel dropped instead of liquid solution on the performance of the OECTs is explored. In a pure laboratory test setting, liquid solution is dropped and is regularly replaced as the liquid evaporates. Since there are two transistors used in the NOT gate, this removes the need for dropping the electrolyte on the reference transistor, simplifying the measurement and paving the way for easier integration of the device in a biosensor system for real-world testing. The hydrogel can be included on the reference transistor during fabrication, while the sensing transistor would use the electrolyte from whichever medium that is to be used for sensing (i.e blood, saliva, or sweat).

Preliminary results are also shown for the NOT gate device with the application of selective glucose sensing. Because OECTs are sensitive to any ion in solution due to the voltage pushing positively-charged ions, selectivity is an issue for any device like this in a biosensing application. For example, if a solution were to contain both a

high concentration of sodium ions and low concentration of calcium ions, the device would only be able to detect the high concentration of sodium. This is an issue if the intended sensing target is the calcium. Thus, for a real-world application, selectivity is crucial. Glucose sensing has been demonstrated in OECT device, but has not been demonstrated in logic gate sensors. In this chapter, NOT gate devices are functionalized to target glucose molecules and preliminary sensing results are outlined.

## 4.2 Materials and Methods

### 4.2.1 Material Preparation

For the purposes of aerosol jet printing, multiple inks were used to print various layers of OECT devices. Gold (Au) ink (UTDOTS, UTDAu40 TE) was ordered and used as-is, as was polyimide (PI) ink (UTDOTS, PI-AJ) and platinum (Pt) ink (UTDOTS, UTDPt). PEDOT:PSS ink was prepared as a solution of the following ingredients: PEDOT:PSS solution dispersed in water (Clevios PH-1000, 5 mL), ethylene glycol (EG) (Sigma Aldrich, 1.25 mL), dodecylbenzene sulfonic acid (DBSA) (Sigma Aldrich, 12.5  $\mu$ L) and (3-glycidyloxypropyl) trimethoxysilane (GOPS) (Sigma Aldrich, 60  $\mu$ L). The ethylene glycol was added to improve the conductivity of the printed film. DBSA is added to adjust the surface tension, while GOPS is a crosslinker that is used to prevent the film from dissolving in electrolyte. The ingredients are stirred under an N<sub>2</sub> environment at 700 rpm for 15 minutes, then transferred to a clean bottle and ultrasonicated for an additional 15 minutes. The resulting solution is then filtered twice - once with a 1.5  $\mu$ m filter, and once with a 0.45  $\mu$ m filter. 1.5 mL of the final solution is then used for aerosol jet printing.

To test the effects of hydrogel on ion sensing, a hydrogel was created with a mixture of gelatin powder (Sigma Aldrich, Gelatin B) and 100 mM NaCl solution. The ingredients were mixed at a ratio of 5% w/v of gelatin to solution and stirred at 1200

rpm overnight at a temperature of 60°C. 15  $\mu\text{L}$  of the resulting mixture was drop casted on the devices and left to evaporate overnight in a refrigerator at 4°C.

To functionalize the OECT devices for glucose sensing, various materials are required. The procedure involves drop-casting various layers one after the other. First, a 1% w/v chitosan (CHIT) (Sigma Aldrich, low molecular weight) solution was prepared, mixed with 1% v/v acetic acid (Sigma Aldrich). Glucose oxidase (GOx) (Sigma Aldrich, from *aspergillus niger*), the primary sensing enzyme, was dissolved in phosphate buffer solution (PBS) (Fisher Scientific, 1xPBS) at a concentration of 50 mg/mL and ultrasonicated for 10 minutes. The CHIT and GOx solutions were mixed together at a 1:1 ratio to achieve a final GOx concentration of 25 mg/mL. 7.5  $\mu\text{L}$  of the resulting solution was drop-casted onto devices and left to dry at 4°C overnight. 0.5  $\mu\text{L}$  of Nafion solution (Sigma Aldrich, 2.5%) was then drop-casted and left to dry at 4°C. A hydrogel was then created from PBS and gelatin in order to prevent the previous layers from washing away, in the same manner as the NaCl hydrogel (5% w/v). To prevent the melting of the hydrogel at elevated temperatures, the crosslinker gluteraldehyde (GA) (Sigma Aldrich, grade II) was added to the hydrogel mixture and immediately drop-casted before the crosslinking occurred. 4  $\mu\text{L}$  of the mixture was drop casted with a GA weight of 1%. The final films are left to dry at 4°C overnight, and then washed with DI water before use.

### 4.2.2 Aerosol Jet Printing

Similar to the temperature sensor in Chapter 3, the device electrodes and traces were printed using an Optomec Aerosol Jet 5X 3D printer onto polyimide (Kapton®) substrate of thickness either 1 or 2 mil. The Au nanoparticle ink was deposited under a sheath gas flow of 30 ccm and atomizer gas flow of 25 ccm. The trace widths were 300  $\mu\text{m}$ , with landing pads for testing measuring 1 mm x 1 mm. The OECT gates are 3 mm x 3 mm. This was optimized based on balancing the need for a lower threshold with preserving ink and lowering printing time (as a gate size increases, the

threshold decreases, as discussed in the background chapter). The gold electrodes were annealed on a hot plate at 280°C for 1 hour.

After gold deposition, the PEDOT:PSS channel was printed with a W/L ratio of approximately 4 ( $W = 750 \mu\text{m}$ ,  $L \sim 180 \mu\text{m}$ ). Depending on the application, either 2 or 10 layers of PEDOT:PSS were deposited under a sheath and atomizer flow of 35 and 20 ccm, respectively. The effect of varying layers of PEDOT:PSS on thickness and resistivity was studied and is outlined in Appendix B.1. The PEDOT:PSS layer was annealed at 130°C for 20 minutes. A final mask layer was then printed with PI ink to prevent shorting of traces due to electrolyte (sheath and atomizer flow of 60 and 27 ccm, respectively). 4 layers of PI were used for this purpose ( $\sim 1 \mu\text{m}$ ). The final device was annealed at 130°C for 1 hour and 30 minutes.

In addition to these 3 inks, devices that would later be functionalized with GOx had their gold gates covered by an additional layer of Pt nanoparticle ink. This is to help facilitate the reaction outlined in Section 4.3. The Pt ink was deposited under a sheath and gas flow of 30 and 18 ccm, respectively. The layer was not annealed but sintered by the 3D printer’s built-in laser system.

### 4.2.3 Material and Electrical Characterization

Square films of both PEDOT:PSS and PI were printed and their thickness was measured with an Alpha-step IQ profilometer. The resistivity of PEDOT:PSS was measured by a Lucus Pro4 4000 4-point probe. The annealing temperature and time of the PI ink was optimized using Fourier Transform Infrared (FTIR) spectroscopy using a Thermo Nicolet iS50 FTIR system. These results are not the main focus of this chapter and are thus shown in the Appendix B.1 and B.2. The optimal annealing temperature and time were found to be 130°C for 90 minutes.

All electrical characterization of OECT devices and NOT gates were done with a Keithley 2612B sourcemeter using custom Labview programs. For individual characterization, individual  $I_D$ - $V_D$  curves were collected, with  $I_D$ - $V_G$ , transconductance, and

$\sqrt{I_D}$ - $V_G$  curves extracted from these. Peak transconductance and voltage threshold values were extracted from these curves. For individual devices, the drain voltage is swept from 0 to -1V in steps of 0.02V due to the OEETs being p-type, depletion mode devices. The gate voltage is swept from 0 to 1.6V in steps of 0.1V.

For the OEET NOT gate circuit, a function generator (model ) was used in conjunction with the Keithley sourcemeter to generate  $V_{out}$  vs  $V_{in}$  curves. To maximize sensitivity, 0.3V is taken to be the power supply voltage,  $V_{dd}$ . The input voltage is swept from 0 to approximately 2V in steps of 0.02V, depending on the device and concentration of electrolyte. To extract the sensitivity of the NOT gate devices, the input voltage was measured at a fixed output voltage (i.e 1 mV) for each concentration of electrolyte dropped on the channel. This is known as the switching voltage,  $V_{in,switching}$ . The sensitivity (mV/dec) is then extracted as the difference in  $V_{in,switching}$  plotted against the concentration of electrolyte in a logarithmic scale.

## 4.3 Logic Gate Theory, Circuit, and Design

### 4.3.1 Depletion-mode NOT Gate Operating Principle

The NOT gate circuit in this chapter functions similarly to a standard NOT gate as outlined in the background Section 2.4.1. The key difference is that only the p-type, depletion mode material, PEDOT:PSS, is used as the channel material in both transistors due to the difficulty in finding suitable and stable n-type OMIECs. Because of this, the circuit found in this chapter is not a complementary circuit and requires modification from the traditional pull-up/pull-down network configuration. The modified circuit is shown in Figure 4.1 (a). The top transistor, Q1, acts as the sensing transistor, while the bottom transistor Q2 acts as the reference transistor. Because the two OEET devices in the circuit have the same switching behavior, the bottom transistor has its gate shorted to its source. This results in the device's  $V_{GS}$  value always being equal to 0.

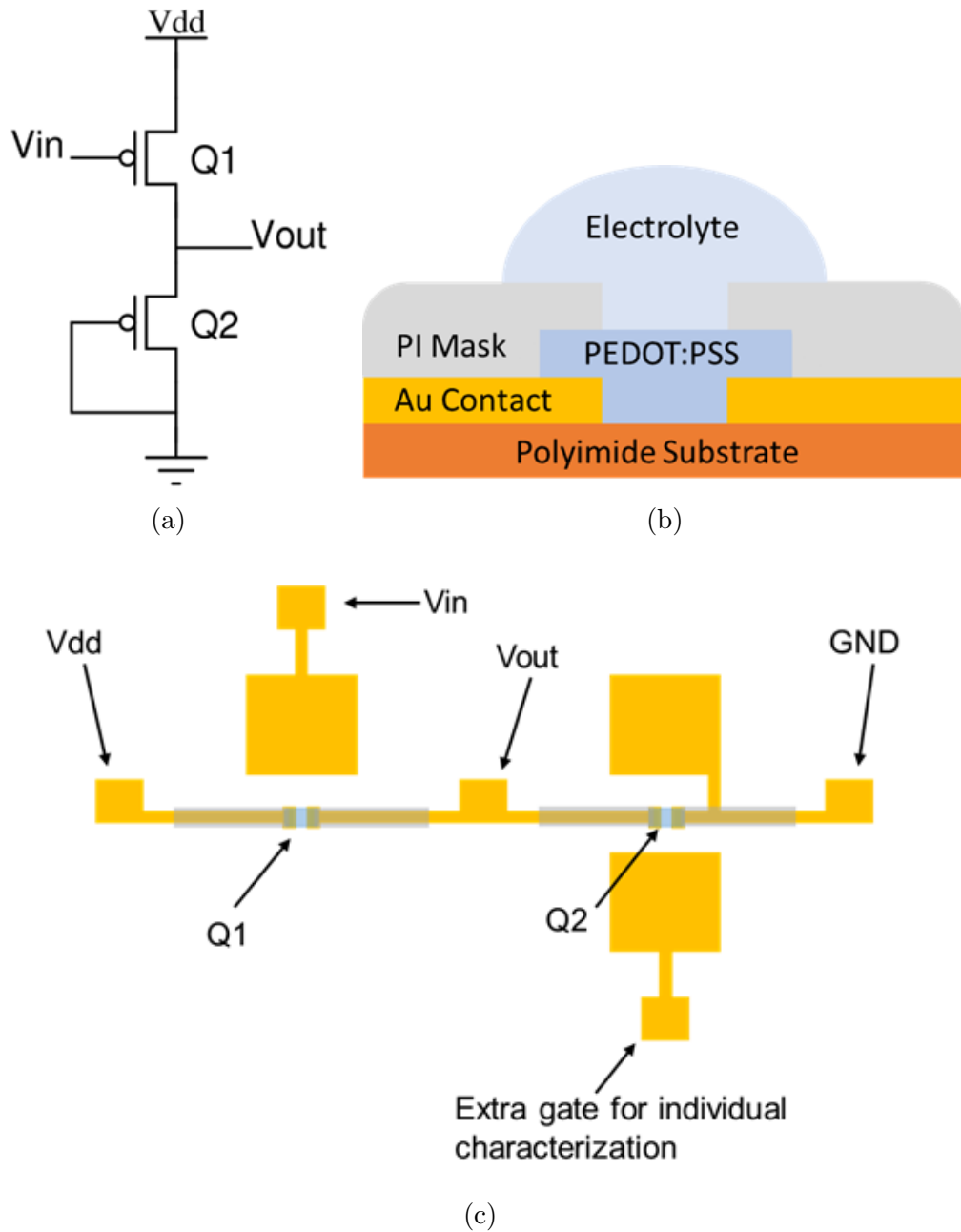


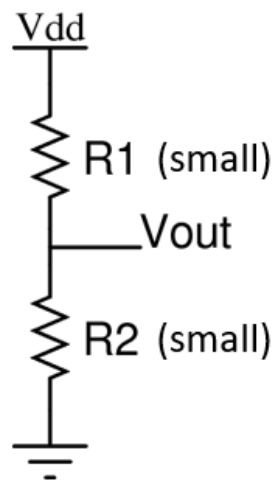
Figure 4.1: (a) Circuit schematic of the depletion mode NOT gate. (b) Cross section of a 3D printed OEET device. Not pictured: the in-plane gold gate that would be found in plane with the Au contact but behind the cross section (looking into the page). (c) 2D top-down view of the layout of the NOT gate circuit.

Because the device is a p-type depletion mode device (due to PEDOT:PSS), this causes the device to always be in its ON state, pulling the output voltage to ground (GND), or 0 V. The cross section of a 3D printed OEET is shown in Figure 4.1 (b). As

discussed in Section 4.2.2, the Au electrodes are first deposited on polyimide substrate, followed by PEDOT:PSS and then PI. Electrolyte is then dropped manually, unless hydrogel is deposited as outlined in the subsequent section 4.4.3. The top-down 2D view of the full layout of the circuit is pictured in Figure 4.1 (c). Each layer which would be drawn in Autodesk AutoCAD and converted to a text script to be sent to the 3D printer, allowing multiple iterations of circuit layouts to be easily created. As shown in the layout, each device has an in-plane gate, allowing measurement without immersing a probe in the electrolyte itself. This was done due to the intention of eventually using these kinds of devices for real-life sensing. The second transistor, Q2, has its gate physically shorted to the trace that connects to the GND probe. For characterization of Q2, a second gate was included in the design. Since the gate voltage must be swept to characterize each device, this is only possible if the  $V_{GS}$  value can be modified. For this reason, electrolyte is dropped over the extra characterization gate for individual characterization of Q2. In NOT gate performance tests, the electrolyte is dropped over the shorted gate.

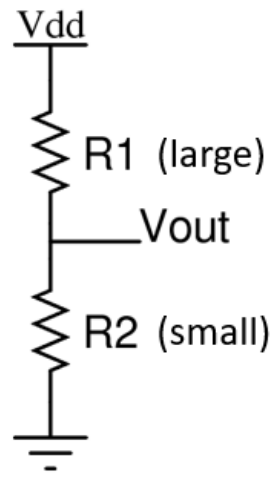
The shorting of the gate of Q2 results in a modified NOT gate transfer curve. Because Q2 is always in an ON state, it acts as a fixed resistance in the circuit. Thus, depending on the input to the single sensing transistor Q1, the NOT gate can be represented by a voltage-division circuit, shown in Figure 4.2. In the first case (Figure 4.2 (a)), the input to Q1 is low, or 0 V. Both devices are on with roughly the same ON resistance (assuming matched devices), causing the output to be divided evenly between  $V_{dd}$  and GND. In the second case (Figure 4.2 (b)), the input to Q2 is high, with the voltage level corresponding to however much is required to fully turn off Q1. This causes the resistance of Q1 to be very large in comparison to Q2, allowing Q2 to pull the output low to GND, or 0 V.

**Case 1:  $V_{in} = \text{GND (0)}$ ,  
 $R1 \approx R2$ ,  $V_{out} = \frac{1}{2} V_{dd}$**

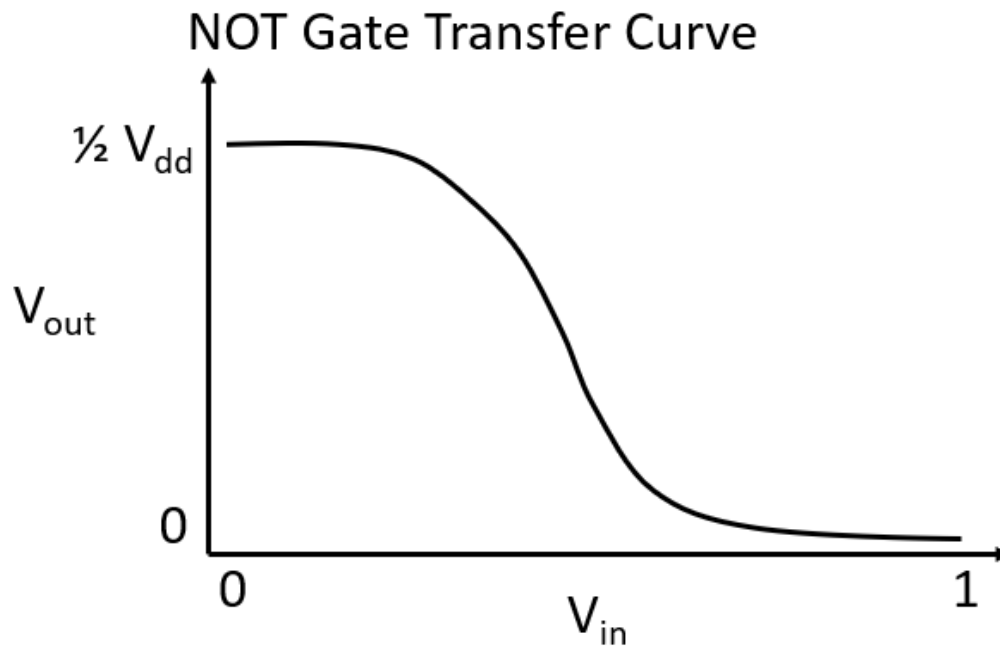


(a)

**Case 2:  $V_{in} = V_{dd} (1)$ ,  
 $R1 \gg R2$ ,  $V_{out} = \text{GND (0)}$**



(b)



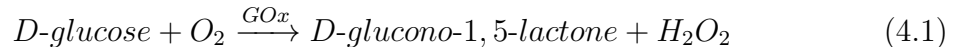
(c)

Figure 4.2: (a) Resistance representation of the depletion-mode NOT gate with  $V_{in}$  of logical 0. (b) Resistance representation of the depletion-mode gate with  $V_{in}$  of logical 1. (c) The transfer curve of the depletion-mode NOT Gate.

In an ideal gate, the channels would be made of complementary materials (p and n-type). In this configuration, the output is degraded to a maximum of half of the power supply level. This is not ideal for circuit applications, as the degraded output level may not be enough to fully turn off the p-type devices in the next stage of logic, if one exists. This is why in complex systems such as larger digital arithmetic circuits, complementary MOS (CMOS) devices are used. However, since this work focuses on devices for the purposes of biosensing, one stage of logic is sufficient and the degraded output logic level is irrelevant.

### 4.3.2 Glucose Sensing Mechanism

As discussed in Section 2.2.1, OECTs operate based on the assumption that ions in the electrolyte can dope or de-dope the OMIEC that acts as the channel material. In this chapter, some logic gates were functionalized to target glucose molecules. Since these molecules are not charged, they must undergo a reaction to help facilitate proper OECT operation. In the functionalization scheme outlined in Section 4.2.1, glucose oxidase (GOx) is dropped in order to help set the condition for a reaction that can generate hydrogen peroxide ( $H_2O_2$ ). This reaction is shown below:



where the symbols have their usual meanings. In the presence of GOx, glucose forms hydrogen peroxide in an amount that is directly proportional to the amount of glucose. Hydrogen peroxide is important due to its decomposition into oxygen, hydrogen ions and electrons. This reaction is catalyzed by platinum, which is why the golden gates shown in Figure 4.1 (c) had an extra layer of platinum ink printed over them for certain devices in this chapter. The dissociation reaction is shown below:



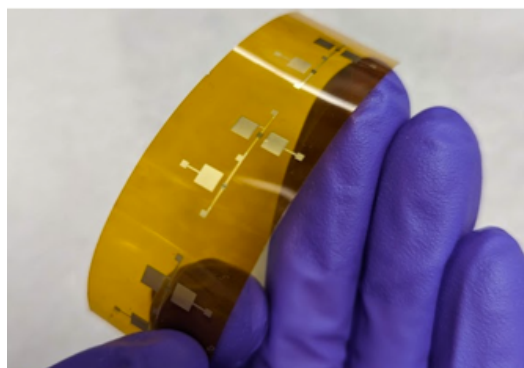
where  $e^-$  is an electron that is transferred to the Pt gate electrode. This electron transfer current increases the effective gate voltage of the device, decreasing its threshold. Thus, an increase in either glucose molecules or gate voltage is sufficient to drive the hydrogen ions into the channel to de-dope it, turning it off. This functionalization scheme has been used for OECT devices for glucose sensing in the past, but to the best of our knowledge has not been used for biosensor devices in the form of logic gates [58]. An image of a device with the glucose functionalization is illustrated in Figure 4.3 (b).



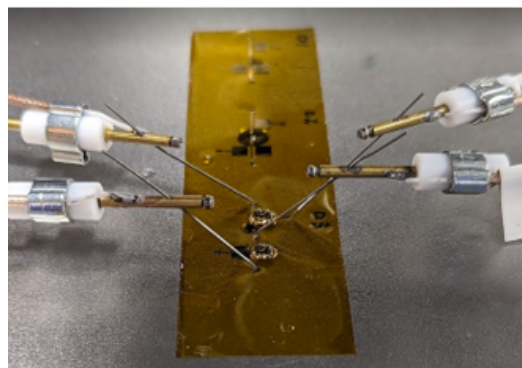
(a)



(b)



(c)



(d)

Figure 4.3: (a) A hydrogel-treated Q1 of a NOT gate device under test. (b) Q1 of a NOT gate device functionalized with GOx, nafion, and a protective hydrogel of 1xPBS. (c) Fabricated NOT gates printed on 2 mil polyimide substrate without hydrogel treatment or glucose functionalization. (d) Standard testing setup of printed NOT gates with liquid electrolyte dropped on the channels.

## 4.4 Results and Discussion

In this chapter, 3 variants of device are tested. First are devices that have no hydrogel or functionalization scheme - these are used purely for ion sensing and require electrolyte dropped over the channel and gate before each test. These are illustrated in Figure 4.3 (c) and (d).

Secondly, there are devices that have been treated with an ionic hydrogel based on gelatin as outlined in Section 4.2.1. The ion sensing performance of these devices was assessed in order to eliminate the need for dropping liquid electrolyte before each test, which would simplify real-world testing. This type of device is illustrated under test in Figure 4.3 (a).

Finally, glucose-functionalized devices were developed with an additional platinum gate layer and functionalization scheme outlined in Section 4.2.1. This was done in order to assess the glucose sensing performance and selectivity. All types of devices were first tested individually as well as in the NOT gate circuit configuration.

### 4.4.1 Individual OECT Characterization

In order to gain insight into circuit behavior, the OECT devices must be first individually characterized. The  $I_D$ - $V_D$  curves of the most sensitive devices in this work are shown in Figure 4.4. Two devices from a single NOT gate are demonstrated side-by-side (Q1 and Q2, as explained in Section 4.3.1). The drain voltage of the devices is swept from 0 to -1V while the gate voltage is swept from 0 to 1.6V. The drain voltage range was chosen in order to avoid electrolysis of the water, even though it can be seen in Figure 4.4 that neither device saturates at the lower gate voltages. The gate voltage was chosen based on past device performance (the threshold voltage is calculated to be below 1.6V as outlined later in the section). Because the OECTs are p-type, depletion mode devices, they require a negative voltage between drain and source. This results in the current being drawn from source to drain, or from ground

to power supply, which is the opposite of the conventional current flow in transistors. Hence, the current is shown as negative in all graphs.

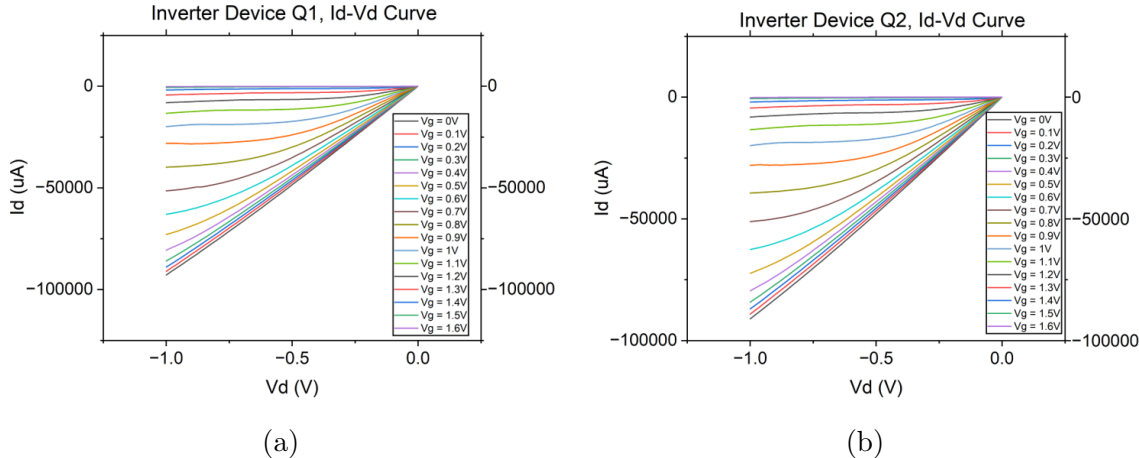


Figure 4.4: (a)  $I_D$ - $V_D$  curves of Q1 of a NOT gate. (b)  $I_D$ - $V_D$  curves of Q2 of a NOT gate.

From the  $I_D$ - $V_D$  curves,  $I_D$ - $V_G$  curves may be extracted which are shown in Figure 4.5. Because the gate voltage is swept in increments of 0.1V in Figure 4.4, the transconductance may be extracted by taking the difference in current level between  $V_G$  increments and dividing it by 0.1 (according to the definition of  $g_m$ ). As demonstrated in Figures 4.4 and 4.5, the devices are well matched, with the current level at 0V reaching 92.8 mA and 91.1 mA for devices Q1 and Q2, respectively. The maximum transconductance is also 116.96 mS and 117.39 mS, which are currently the highest in the world for a planar OECT, to the author's best knowledge, with another high transconductance planar OECT reported by Markova et al., with a value of 108 mS [124]. Other high transconductance OECTs have very recently been reported, but have used techniques such as ultra-thin vertical channel stacking and coaxial channels to achieve tiny channel lengths [125, 126]. In one work, the geometry of the OECT device was exploited to use the thickness of the film as the channel length, which resulted in a channel length of 60 nm and transconductance of 275 mS [126]. The channel length for the devices in this work is approximately 180  $\mu\text{m}$ , which results in a relatively small  $W/L$ , with room for even more improvement of the  $g_m$  value.

Additionally, the planar OECTs have the advantage of exposing their channel to the electrolyte effectively in order to be useful for biosensing. It is speculated the devices in this work have such high values owing to the quality and high crystallinity of the film achieved through aerosol jet printing. It should be noted that achieving extremely high transconductance is not a focus of this work and can easily be improved even more by a variety of techniques: printing a higher number of layers (the highest number of layers printed in this work was 10, resulting in a thickness of approximately  $1.25 \mu\text{m}$ ), shrinking the channel length (the PEDOT devices in this work have a channel length of  $180 \mu\text{m}$  while the shortest channel length printed for other devices was  $22 \mu\text{m}$  as shown in Appendix A.5), and running the devices at a higher drain voltage than  $-1\text{V}$  to achieve a higher current spread at saturation ( $-1\text{V}$  was arbitrarily chosen to avoid risk of water electrolysis).

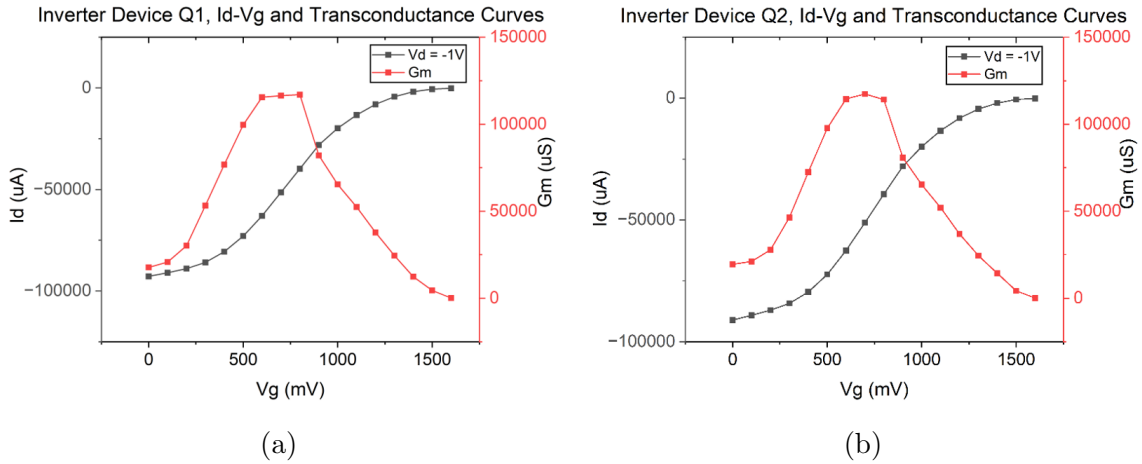


Figure 4.5: (a)  $I_D$ - $V_G$  and  $g_m$  curves of Q1 of a NOT gate. (b)  $I_D$ - $V_G$  and  $g_m$  curves of Q2 of a NOT gate.

Using the extracted  $I_D$ - $V_G$  curves, the voltage threshold can also be extracted based on taking the square root of the current as outlined in Section 2.2.1 and Equation 2.4. The matched characteristics of the two printed devices is further confirmed by their threshold voltages, which are  $1.485\text{V}$  and  $1.490\text{V}$  for devices Q1 and Q2, respectively. In Figure 4.6, the linear equations used to extract these values are shown on the most linear part of the  $\sqrt{I_D}$ - $V_G$  curve (in blue).

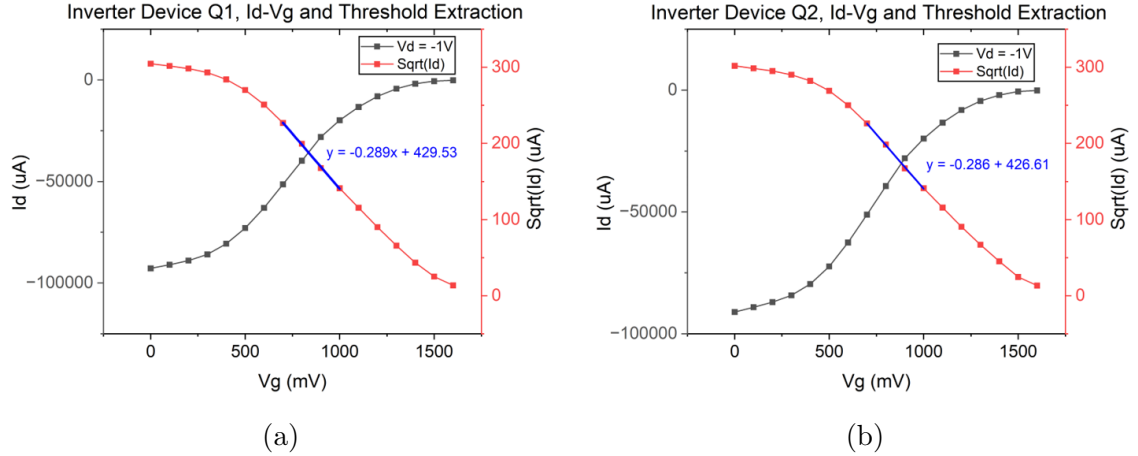


Figure 4.6:  $\sqrt{I_D}$ - $V_G$  curves indicating the equations for voltage threshold extraction (in blue) for (a) Q1 and (b) Q2 of a NOT gate.

#### 4.4.2 Ion Sensing Results

The devices from the previous section were connected in an inverter configuration as illustrated in Figure 4.1 and tested for NOT gate performance. As shown in Figure 4.7, input voltage sweeps were applied with varying concentrations of electrolyte (in this case, NaCl solution) on device Q1, while the bottom device Q2 had a constant reference electrolyte concentration of 100 mM. The devices exhibit classic inverter switching behavior - as the input voltage is swept from input logic level low to high (in this case, 0V to approximately 2V), the device output logic level switches from logic level high to low. As the power supply level  $V_{DD}$  is 0.3V (chosen in order to optimize device threshold and sensitivity), the output level high should theoretically be 0.15V or 150mV as shown in Figure 4.7 (a). However, as a thicker device with more printed channel layers and higher transconductance is used, the output level becomes much more degraded as shown in Figure 4.7 (b) where the output level is only approximately 40 mV.

Figure 4.8 shows the difference in  $I_D$ - $V_D$  curves between these two kinds of devices. The thicker device is capable of running approximately 10x the amount of current than the thinner device, but results in a smaller voltage swing in the NOT gate

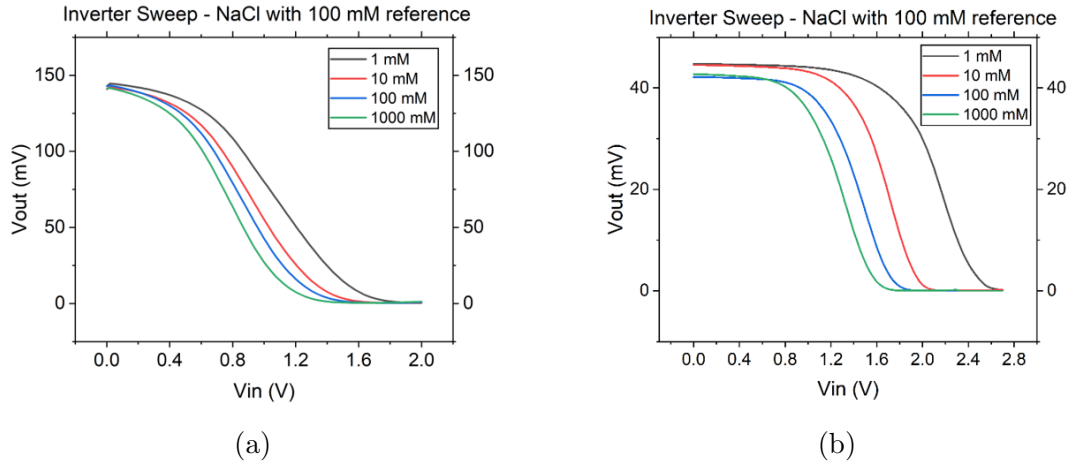


Figure 4.7: NOT gate sweeps with a varying NaCl concentration for devices with (a) 2 printed PEDOT layers ( $\sim 250\text{nm}$ ) and (b) 10 printed PEDOT layers ( $\sim 1.25\mu\text{m}$ ).

transfer curve (Figure 4.7 (b)). This may be due to the thickness of the device not allowing a fast response due to the inability of the ions to permeate into the film at the start of the voltage sweep. Regardless of the output level, however, the thicker device exhibits a higher sensitivity to the  $\text{Na}^+$  ions as shown in Figure 4.9 (a) and (b).

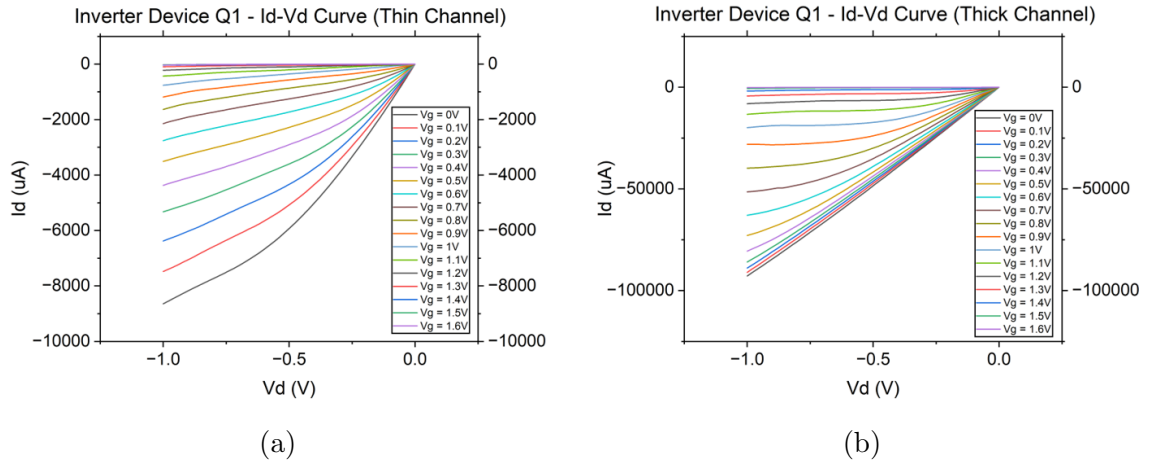


Figure 4.8:  $I_D$ - $V_D$  curves for (a) thinner ( $\sim 250\text{nm}$ ) channel devices and (b) thicker ( $\sim 1.25\mu\text{m}$ ) channel devices.

Due to the varying concentration of NaCl in the electrolyte, varying amounts of ions are available to be driven into the channel at a certain gate voltage. With more

ions in the solution, less voltage is required to de-dope the channel, lowering the threshold voltage. This is reflected in the NOT gate transfer curves in Figure 4.7. As the NaCl concentration increases, the NOT gate transfer curve shifts to the left. This can be used to detect the ion concentration in the solution, as shown in Figure 4.9. The sensitivity was extracted by evaluating the input voltage required to output a voltage of 1mV. This was chosen due to the highest sensitivity at this point and was called the switching voltage,  $V_{in,switching}$ .

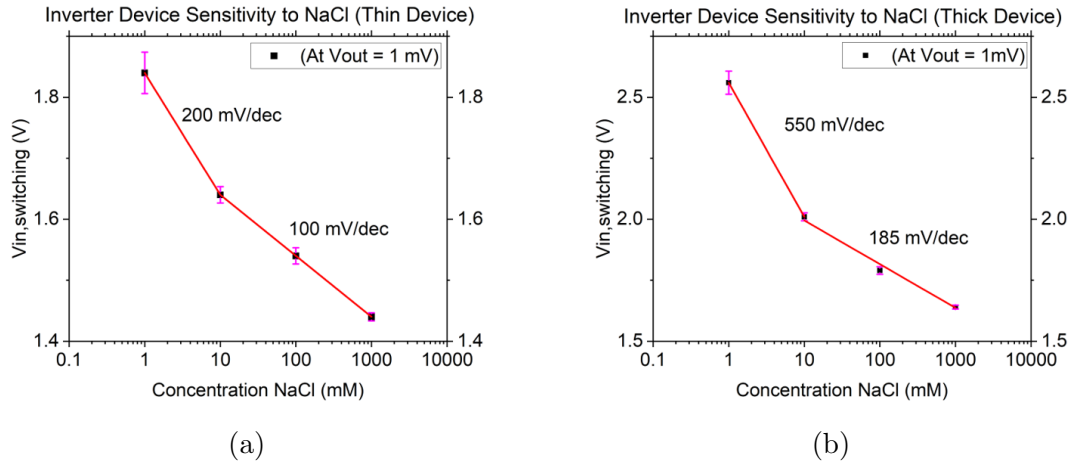


Figure 4.9: Switching voltage vs NaCl concentration curves for (a) thinner ( $\sim 250$ nm) channel devices and (b) thicker ( $\sim 1.25\mu\text{m}$ ) channel devices.

As shown in Figure 4.9, the thicker device with higher transconductance exhibits a significantly higher sensitivity to NaCl, particularly in the 1-10 mM range. This is due to the higher device  $g_m$  value as well as the thickness, which requires more ions to be driven into the channel and thus a wider spread between gate voltages required to achieve this.

Although the highest sensitivity was exhibited for Na<sup>+</sup> ions, different ions were also tested. The results are shown in Figure 4.10, with Na<sup>+</sup>, Ca<sup>+</sup>, Mg<sup>+</sup>, and K<sup>+</sup> ions tested in electrolyte solutions at the same concentrations.

The sensitivities for these devices were extracted and are illustrated in sensitivity curves in Figure 4.11 for each ion type. It can be seen that the highest sensitivity is demonstrated by NaCl, followed by MgCl<sub>2</sub>, KCl, and finally CaCl<sub>2</sub>. This can be

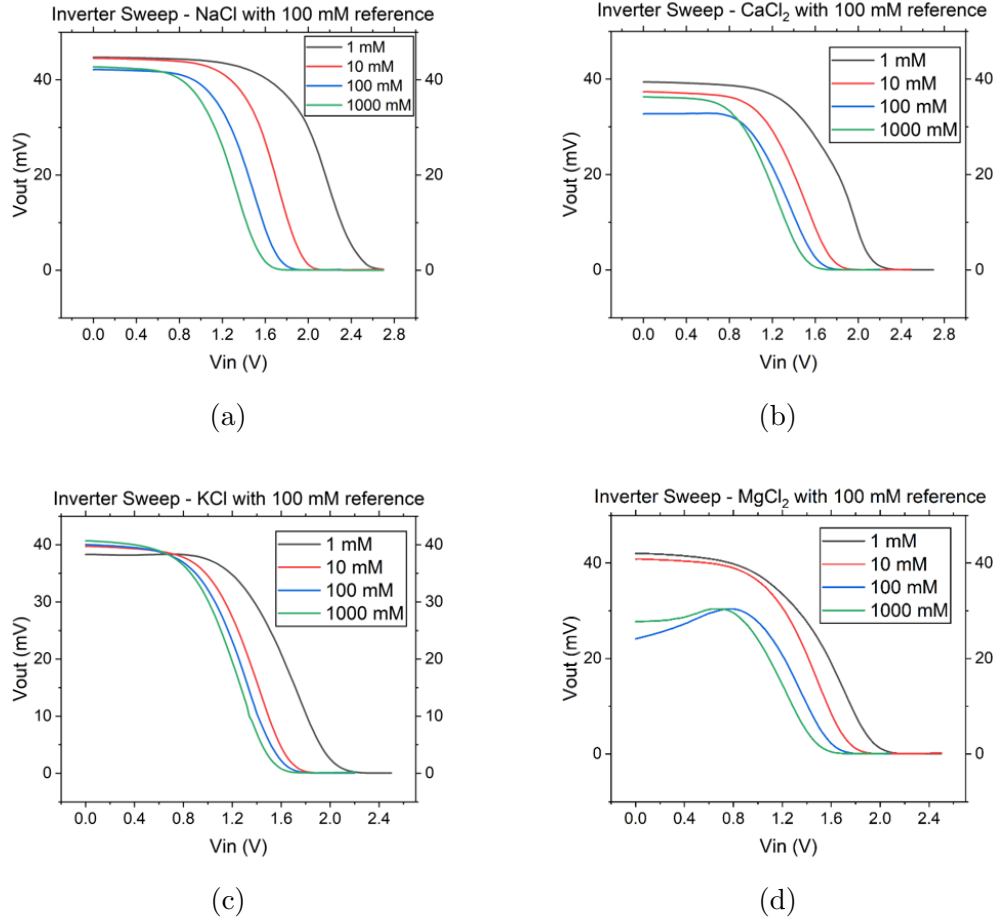


Figure 4.10: NOT gate sweeps with varying concentrations of (a) NaCl, (b) CaCl<sub>2</sub>, (c) KCl, and (d) MgCl<sub>2</sub>

explained by the fact that heavier ions experience lower ionic mobility, which impacts the performance of the device. Thus, lower concentrations require more gate voltage to effectively turn off the device, and this relationship appears to be non-linear due to the higher concentrations requiring approximately the same gate voltage. This results in less of a spread of gate voltage to turn off the device for each concentration, lowering the sensitivity. Other work has also verified this same relationship between ion type and sensitivity.

It can be noted that all of the sensitivities extracted are higher than the theoretical Nernst limit, which is 59.2 mV/dec [127]. This limit is a theoretical value that was first extracted for ion-selective FETS (ISFETs) in order to determine the maximum rate

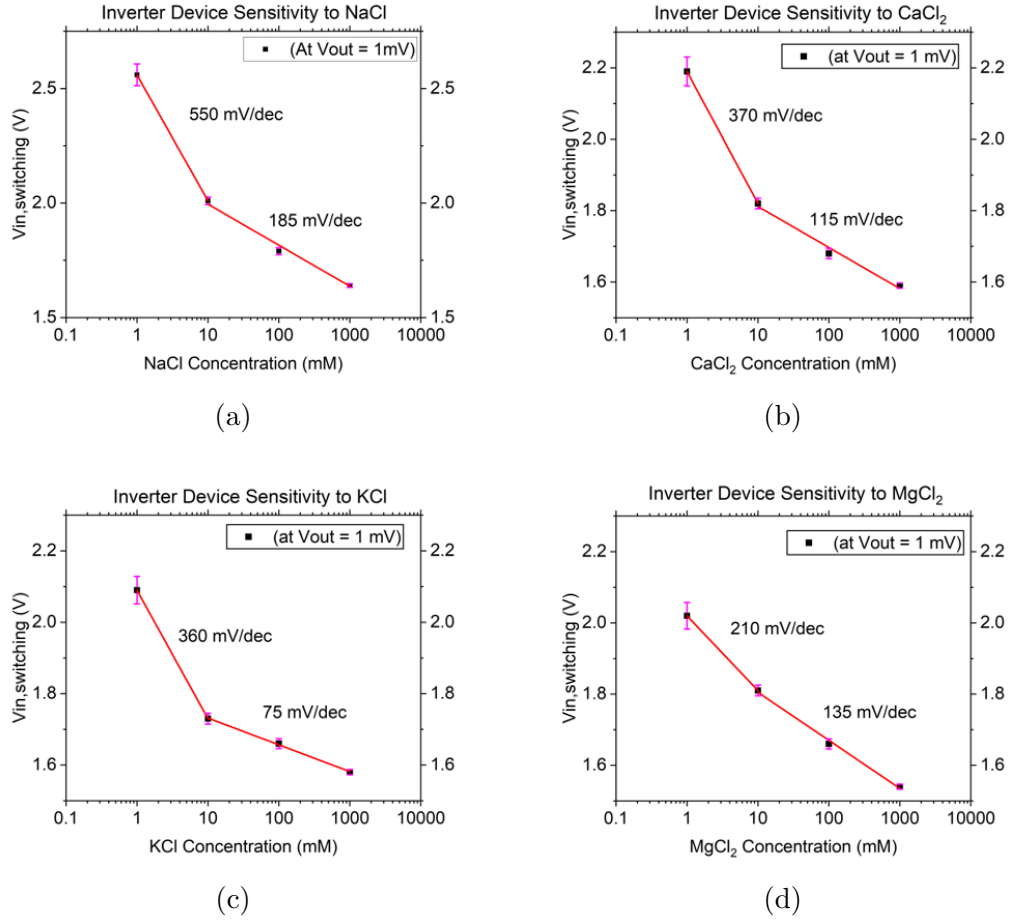


Figure 4.11: Sensitivity curves for devices tested with (a) NaCl, (b) CaCl<sub>2</sub>, (c) KCl, and (d) MgCl<sub>2</sub>

of change of the surface potential of their gate when detecting pH. The Nernst limit is achieved by taking an equation first derived by a combination of the Guoy-Chapman-Stern model and surface binding theory. The following describes the equation:

$$\frac{d\psi_0}{dpH} = 2.303\alpha \frac{\kappa T}{q} \quad (4.3)$$

where  $\psi_0$  represents the surface potential of the gate (V),  $\alpha$  is a dimensionless unit describing the capacitance of the gate dielectric and ionic solution present (from 0 to 1),  $\kappa$  is Boltzmann's constant, T is the absolute temperature (in K or °C depending on the units of Boltzmann's constant), and q is the elementary charge (C). As  $\alpha$  tends to unity, the absolute limit approached by this equation is 59.2 mV/dec. In

the literature this has been used as a standard for pH and ion sensing, but has been surpassed in this work and other work [18, 127]. Since this relationship relies on the geometry and physics of ISFET devices, other configurations such as OECTs in this work have been shown to surpass this limit.

### 4.4.3 Hydrogel Treatment Results

In order to make the device useful as a biosensor, the effect of dropping a hydrogel rather than liquid solution on the channel of the device was explored. In a biosensor device, ideally the reference electrode would be covered in hydrogel because the reference electrolyte remains fixed. Thus, the top transistor can have a varying analyte concentration. A biosensor of this kind can focus on directing solution to only one device rather than two, allowing for a simpler system, such as a microfluidics system that directs flow only to one transistor (the top transistor, Q1). This would also be useful in a lab setting where electrolyte would not have to keep getting dropped on the device due to evaporation.

Because of the fact that only Q2, the always-on transistor, is the device that needs to have electrolyte dropped on it, the traditional performance of the device is not as important as the performance of the device in the always-on state. However, for the sake of thoroughness, the effects of the hydrogel on regular performance are studied. A hydrogel of 100 mM NaCl was dropped on the channel of an OECT device according to the procedure outlined in Section 4.2.1 and tested individually. The results are shown in Figure 4.12.

As shown in Figure 4.12, the dropping of a hydrogel reduces the maximum current level of the device as well as its peak transconductance. The maximum current level at gate voltage of 0V and drain voltage of -1V was reduced from 81.9 mA to 59.2 mA. The peak transconductance was also reduced from 109 mS to 56.2 mS. This is likely due to the permeability of the hydrogel itself - the hydrogel is gelatin based and highly viscous, which makes ion movement through the hydrogel difficult. The current

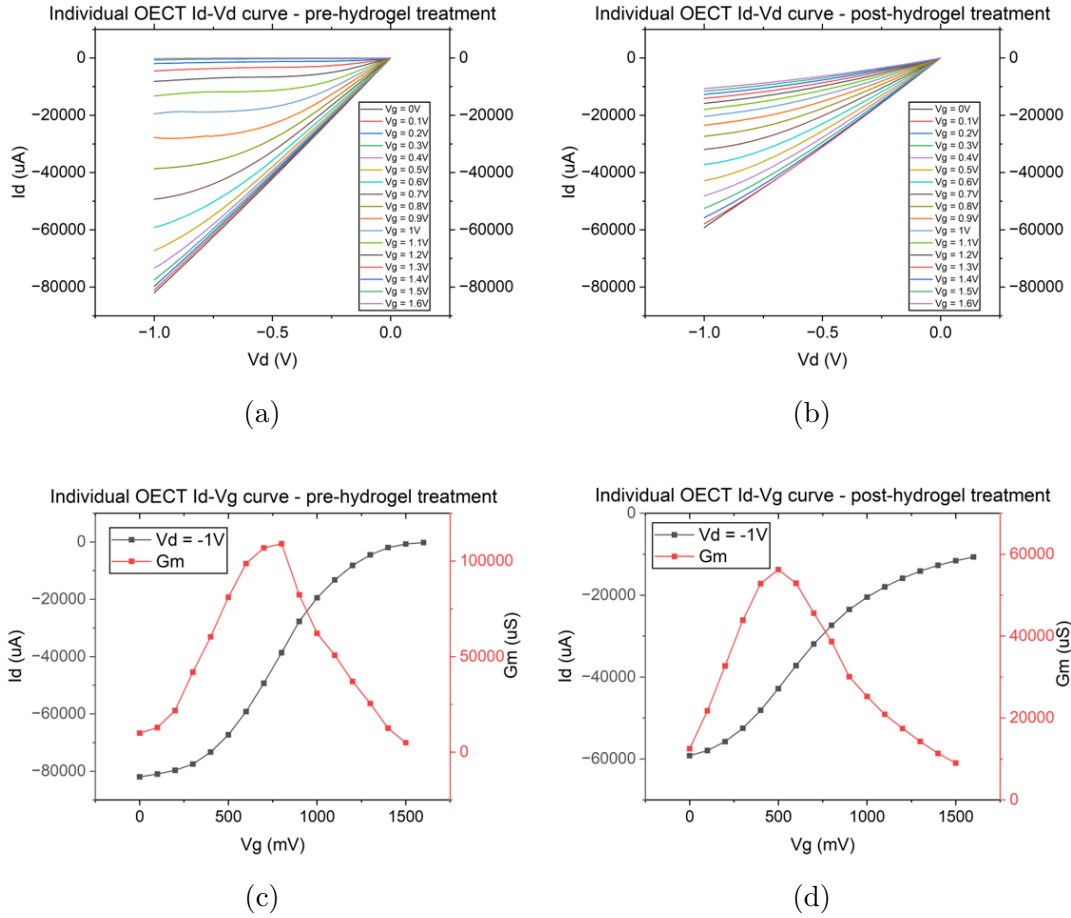


Figure 4.12:  $I_D$ - $V_D$  curves for devices (a) pre-hydrogel treatment and (b) post-hydrogel treatment.  $I_D$ - $V_G$  and transconductance curves for devices (c) pre-hydrogel treatment and (d) post-hydrogel treatment.

decrease is due to lack of ionic charge in the channel at 0V (due to the permeability) which would usually contribute to the current between source and drain. Additionally, the device cannot fully turn off at a reasonable voltage (Figure 4.12 (b) shows the device is not close to turning off even at a gate voltage of 1.6V). Due to the lowered effect each gate voltage step has in driving in more ions, the peak transconductance has also been reduced.

Although the performance of a single device is degraded with a hydrogel layer, the hydrogel may still be incorporated in device Q2 of a OECT inverter. A hydrogel was dropped over Q2 while NaCl solution was dropped in varying concentrations over Q1. The results with and without a hydrogel on Q2 are illustrated in Figure

4.13. For the detection range of 1-10 mM NaCl, the sensitivity dropped from 570 mV/dec to 300 mV/dec. However, in the 10-100 mM range, the detection range stayed approximately the same, rising slightly from 190 mV/dec to 210 mV/dec. This confirms the operation of a hydrogel-based inverter ion sensor, although further work is needed to improve the sensitivity in the 1-10 mM range. The transfer curves for post-hydrogel treatment seem to follow the same trend as the transfer curves for heavier ions, where the 1 mM graph shifts to the left while the 10, 100, and 1000 mM remain relatively the same, reducing the sensitivity for only the 1-10 mM range. Further work can focus on isolating the reason for this to improve the sensitivity.

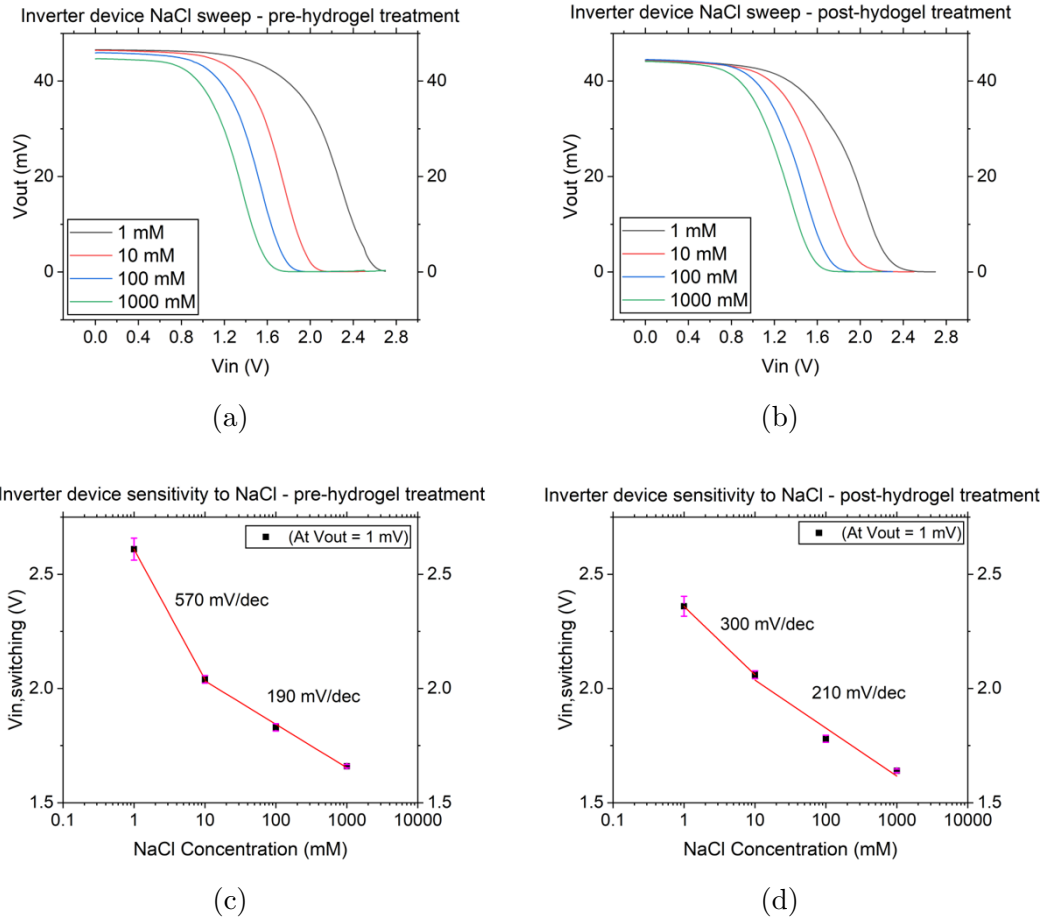


Figure 4.13: NOT gate sweeps of an inverter device with NaCl (a) pre-hydrogel treatment and (b) post-hydrogel treatment. Sensitivity curves for NaCl solution for an inverter device (c) pre-hydrogel treatment and (d) post-hydrogel treatment.

#### 4.4.4 Glucose Sensing Results

OECT devices were functionalized according to the GOx functionalization scheme outlined in Section 2.4.1 in order to create a glucose-sensitive inverter biosensor. Using both glucose and NaCl solution (both 100 mM) as the electrolyte, Q1 was individually characterized to gain insight into shifts in current levels, transconductance, and voltage threshold. Q2 was not individually functionalized due to its shorted gate not allowing individual characterization. The results are shown in Figure 4.14.

As indicated by the  $I_D$ - $V_D$  curves, it can be seen that the maximum current level drops when glucose is dropped rather than another electrolyte such as NaCl. This is

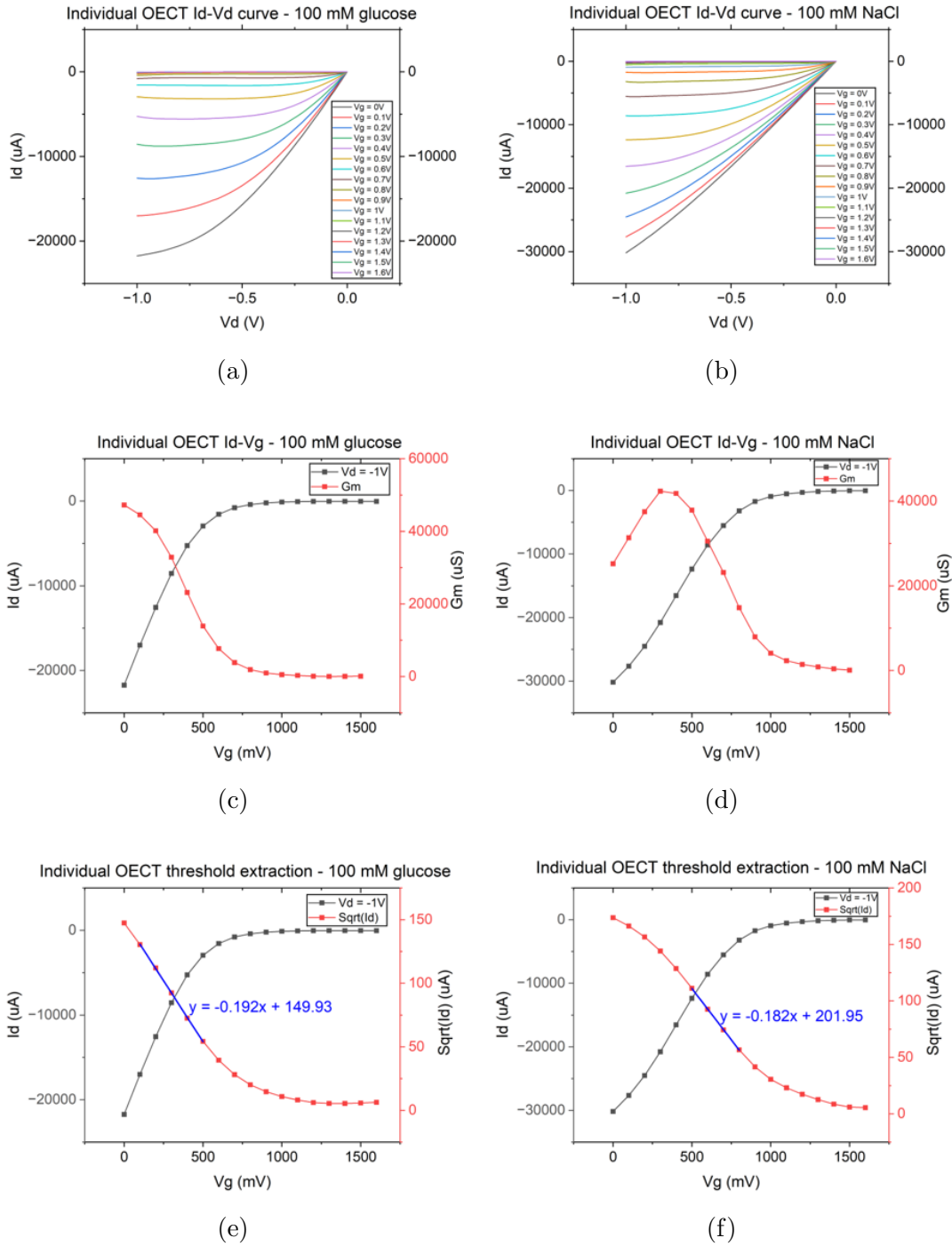


Figure 4.14:  $I_D$ - $V_D$  curves for device Q1 with (a) 100 mM glucose and (b) 100 mM NaCl.  $I_D$ - $V_G$  and  $g_m$  curves for device Q1 with (c) 100 mM glucose and (d) 100 mM NaCl. Voltage extraction demonstrated for device Q1 with (e) 100 mM glucose and (f) 100 mM NaCl.

most likely due to the lower ionic mobility of the glucose molecules due to their greater weight. The transconductance is also higher at 47.2 mS for glucose compared to 42.3 mS for NaCl. This is due to the targeted reaction that occurs at the functionalized gate in the presence of glucose. The voltage threshold is also drastically different for the device tested with glucose - the threshold is 0.78V compared to the device tested with NaCl, which is 1.11V. This is due to the faradaic current that is induced at the platinum gate due to the dissociation of hydrogen peroxide. The current increases the effective gate voltage of the device and decreases its threshold. This threshold difference can be used to selectively detect glucose rather than ions such as NaCl, as shown in Figure 4.14. However, this would assume hydrogen peroxide is not already present in the solution, as the hydrogen peroxide is ultimately what determines the change in threshold. Future work could focus on an even more selective functionalization scheme.

NOT gate sweeps were performed on the finished inverter with functionalizations both on Q1 and Q2 (with shorted gate). The results are illustrated in Figure 4.15. It can be seen in Figure 4.15 (a) that the glucose does have the expected effect on the output voltage curve - as glucose concentration increases, the curve shifts to the left to lower input voltages. However, as shown in Figure 4.15 (b), the sensitivity is not close to the sensitivities of the ion sensing curves shown previously in the chapter due to time limitations. Future work can focus on optimizing the sensitivity of the glucose inverter devices in order to create a more useful biosensor. It should be noted that these are preliminary results, and the devices used for this glucose functionalization were not as sensitive as the devices used for ion sensing shown previously in the chapter. This is demonstrated by the difference in the voltage output level at a gate voltage of 0V for the inverter shown in Figure 4.15 (a) (glucose) versus the inverter shown in Figure 4.10 (a) (NaCl). The output level is 80 mV for the glucose compared to 40 mV, indicating a lower sensitivity. As discussed previously, the trend with these inverters indicates a lower and more degraded output voltage for thicker and more

sensitive OECT devices.

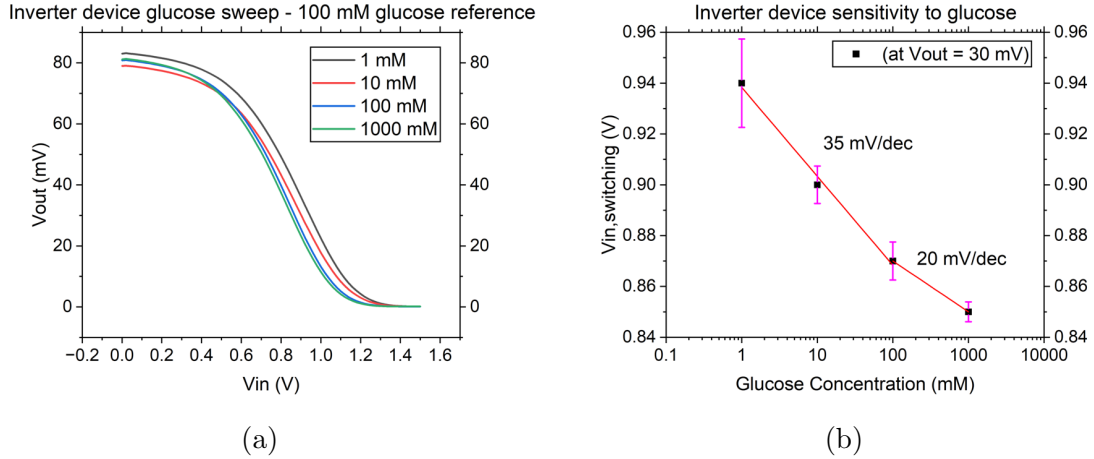


Figure 4.15: (a) NOT gate sweeps of a glucose-functionalized inverter device with varying glucose concentration. (b) Sensitivity curve of a glucose-functionalized inverter device.

## 4.5 Conclusion

In this chapter, logical NOT gates were built using OECTs. The gates were used for the sensing of 4 different ion types as well as glucose. To make the devices more useful as biosensing devices, the effects of using hydrogel rather than electrolyte solution on the channel of the sensing transistor were explored. It was found that the devices built had extremely high transconductance (as high as 117 mS) that directly translated to high sensing performance. The NOT gates operated according to the logical theory outlined in Section 4.3.1 and had a maximum sensitivity of 570 mV/dec when sensing NaCl in the 1-10 mM range. It was found that hydrogel had an adverse effect on the sensitivity and performance of the devices, with the trade-off of convenience and ease of use in biosensing application. Finally, the devices were found to be sensitive to glucose when functionalized with GOx. The maximum sensitivity was found to be 35 mV/dec in the 1-10 mM range. Future work will focus on optimizing hydrogel performance by increasing permeability of the gel in order to increase ionic mobility, while maintaining structural integrity. For ion sensing, selectivity can be improved

upon by incorporation of an ion-selective membrane. Preliminary results for this are shown in the Appendix C. Finally, glucose sensitivity can be improved upon by improving the sensitivity of the OECT device itself as well as optimization of the functionalization scheme for these devices. Additionally, in order to make the devices more selective, an alternate functionalization scheme may be used that doesn't rely on hydrogen peroxide generation since in real-world applications, the compound may be present in the analyte solution.

Table 4.1: Summary of sensitivity results for various sensing parameters using a PEDOT:PSS based depletion mode logic inverter.

Sensing Parameter (detected with logic gate configuration)	Detection Range (mM)	Sensitivity (mV/dec)
Na <sup>+</sup> ion	1-10	550
	10-1000	185
Ca <sup>2+</sup> ion	1-10	370
	10-1000	115
K <sup>+</sup> ion	1-10	360
	10-1000	75
Mg <sup>2+</sup> ion	1-10	210
	10-1000	135
Na <sup>+</sup> ion (pre-hydrogel treatment)	1-10	570
	10-1000	190
Na <sup>+</sup> ion (post-hydrogel treatment)	1-10	300
	10-1000	210
Glucose Molecule	1-100	35
	100-1000	20

# Chapter 5

## Complementary NOT Gate Based on Aerosol Jet 3D-Printed Organic Electrochemical Transistors

### 5.1 Introduction

In the area of organic electronics, complementary logic gates have historically proved to be difficult to implement due to the stability issues present in n-type organic semiconductors [128]. The advantage of complementary logic gates is in the fact that a full output voltage swing from the power supply voltage to ground (0V) is possible over the same input voltage range. This makes binary digital logic possible with input and output logic levels roughly equal to each other. The operating principle of a traditional complementary logical NOT gate is outlined in the background section 2.4. Ideally, logic gates will include p-type devices in the pull-up network (PUN) and an n-type device in the pull-down network (PDN). This has been implemented and demonstrated in the literature to varying degrees of success. Kwon et al demonstrated 3D complementary organic TFTs using inkjet printing on PET substrate using dithieno[2,3-d;2',3'-d']benzo[1,2-b;4,5-b']dithiophene (DTBDT-C<sub>6</sub>) as the p-type material and an n-type benzo-bis(thiadiazole) derivative (TU-3) as the n-type material [129]. Casula et al. have also inkjet-printed complementary circuits on paper substrate [130]. Additionally, a single channel material may be

used for such applications if the material is ambipolar; an ambipolar material is one that exhibits both n-type and p-type conduction based on the polarity of voltages applied. Yoo et al. achieved complementary circuits by spin coating poly[2,5-bis(2-hexyldecyl)-2,3,5,6-tetrahydro-3,6-dioxopyrrolo[3,4-c]pyrrole-1,4-diyl-alt-[2,2':5',2"-terthiophene]-5,5"-diyl] (PDPP3T), an ambipolar organic material, as the channel material for organic TFTs [131]. However, the need for a wide voltage range complicates the circuits involved in implementing these kinds of logic gates. Organic electrochemical transistors have also been used in complementary logic gates due to their low operating voltages [84, 132] using a combination of different fabrication techniques. However, fully aerosol-jet printed complementary logic gates have not yet been realized.

In the previous chapter, one single channel material was used to implement depletion-mode logic gates. However, because of the need for circuit modification, the voltage swing did not range from the power supply voltage to 0V. This chapter focuses on achieving fully aerosol-jet printing a complementary NOT gate with output characteristics that can be useful for pure digital logic operations rather than biosensing. The NOT gate is fabricated using PEDOT:PSS as the p-type material and gNDI-Br<sub>2</sub> as the n-type material. The operating principle of these two OMIECs has been outlined in the background section 2.2. Individual characterization of each type of device is shown as well as efforts to match their current driving capabilities. Because the p-type and n-type materials are different kinds of organic materials, matching the individual characteristics such as saturation current and voltage threshold are crucial to obtaining a circuit with proper input and output voltage behavior. Final NOT gate sweeps are shown as well as optimizations of individual characterizations for each device.

## 5.2 Materials and Methods

### 5.2.1 Material Preparation

The complementary NOT gates were prepared similarly to the depletion-mode NOT gates in Chapter 4, with the addition of the gNDI-Br<sub>2</sub> channel which added another step to the fabrication. Gold (Au) and polyimide (PI) inks were used as prepared and outlined in Section 4.2.1. The PEDOT:PSS ink recipe, however, was slightly modified to degrade the characteristics of the PEDOT:PSS in order to match the characteristics of the p-type device closely with the n-type device. For this reason, the ratios of the 4 ingredients outlined in Section 4.2.1 were modified to lower the conductivity of the PEDOT:PSS. In the PEDOT:PSS ink solution for this work, the quantities of ethylene glycol (EG), dodecylbenzene sulfonic acid (DBSA), and (3-glycidyloxypropyl) trimethoxysilane (GOPS) were 0.265 mL, 5  $\mu$ L, and 50  $\mu$ L, respectively, when added to 5 mL of PEDOT:PSS. The rest of the preparation procedure remained the same and 1.5 mL of the remaining solution was used for aerosol jet printing.

The NDI ink was prepared in a similar fashion to the PEDOT:PSS ink with a final volume of 1.5 mL. 75 mg of synthesized NDI was taken and mixed at a 9:1 ratio of oxylene to chloroform, for a volume of 1.35 mL of oxylene and 0.15 mL of chloroform. The mixture was manually stirred until the NDI was dissolved in solution, and then ultrasonicated for 30 minutes. The resulting ink was then directly transferred to the aerosol jet printing vial.

### 5.2.2 Aerosol Jet Printing

The complementary NOT gates were printed in the same manner as the depletion-mode NOT gates in Chapter 4. Au electrodes, PEDOT:PSS channel, and polyimide ink was deposited under the same parameters outlined in Section 4.2.2. However, the PEDOT:PSS channel was only deposited with one layer of printing in order to achieve a less conductive film. The channel was once again printed with a W/L ratio

of approximately 4 ( $W = 750 \mu\text{m}$ ,  $L \sim 180 \mu\text{m}$ ). The NDI channel was printed with 4 layers under a sheath and atomizer flow of 40 and 20 ccm, respectively. The NDI was printed and annealed directly with the PI film at the same time, meaning it was annealed for 1 hour and 30 minutes total. Due to issues with the performance of the film, the printed channel length was optimized and shrunk down to approximately  $22 \mu\text{m}$  while the length remained the same as for the PEDOT:PSS channel at  $750 \mu\text{m}$ , for a W/L ratio of approximately 34. The details of the optimization of the small feature size printing are outlined in Appendix A.5.

### 5.2.3 Electrical Characterization

Similar to the depletion-mode logic gates, the complementary NOT gates were characterized exclusively with a Keithley 2612B sourcemeter controlled by custom Labview programs. In order to gain insight into the performance of both the PEDOT:PSS and NDI-based devices, individual characterization was performed through measurement of  $I_D$ - $V_D$  and  $I_D$ - $V_G$  curves, with saturation current, transconductance, and voltage threshold values extracted. In contrast to the PEDOT:PSS devices, the drain of the NDI-based devices were swept from 0 to a positive voltage of 1V in steps of 0.02V, with the gate voltage being swept from 0 to 1.2V. The NDI devices are more prone to instability than the PEDOT:PSS devices; for this reason, the gate voltage was swept from 0V to a maximum of 1.2V in steps of 0.1V to avoid damaging the channel.

For the NOT gate sweeps, the setup was identical to the setup outlined in Chapter 4, with some variation in both power supply and input voltage ranges. These variations are further explored in the results section of this chapter.

## 5.3 Logic Gate Theory, Circuit, and Design

In contrast to the previous chapter's NOT gates, the NOT gate in this chapter has the same circuit configuration as a traditional complementary MOS inverter pair. When the input voltage is low, the top p-type device conducts, connecting the output to

the power supply voltage. When the input is high, the top transistor turns off and the n-type transistor turns on, pulling the output to ground, or the low level. The schematic is pictured in Figure 5.1 (a), along with the cross-section and layout in Figures 5.1 (b) and (c). It can be seen in the cross-section and layout that the NDI channel is shorter in length than the PEDOT:PSS channel. This is due to the instability of the small-molecule-based film. It was observed through experiments that a channel length comparable to the PEDOT:PSS channel did not result in a working device. This is likely due to the higher probability of defects in a longer channel for the small-molecule film than for a shorter channel, because devices with a longer channels would not exhibit turn-on behavior, implying conductivity issues.

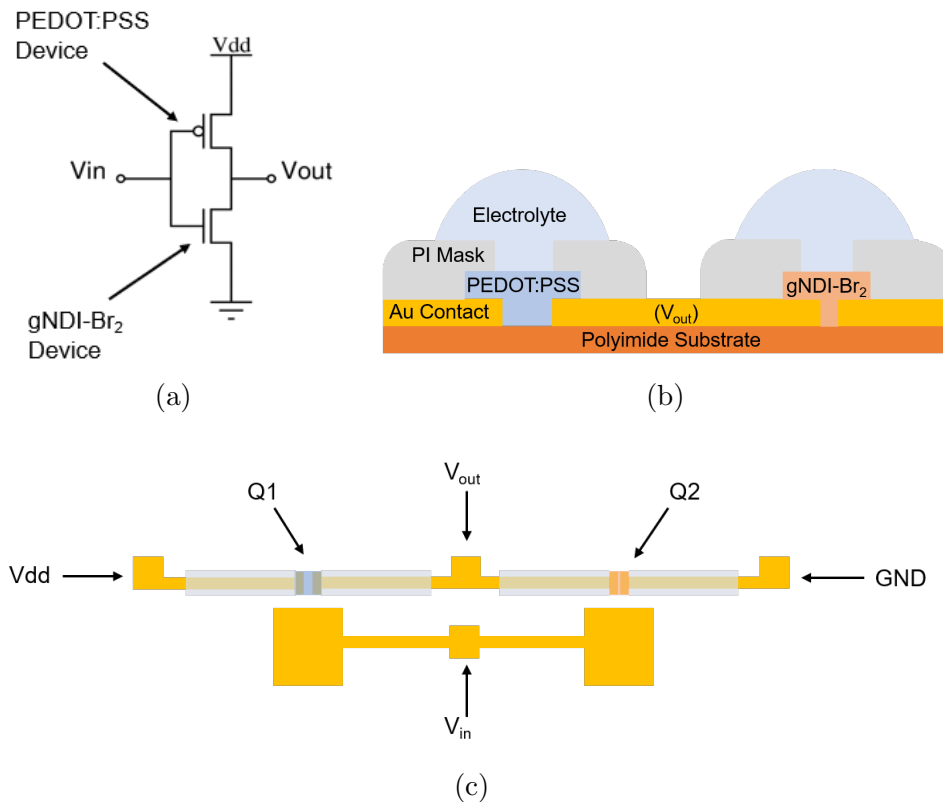
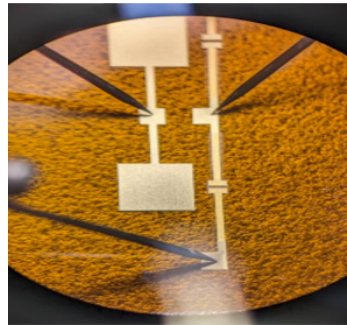
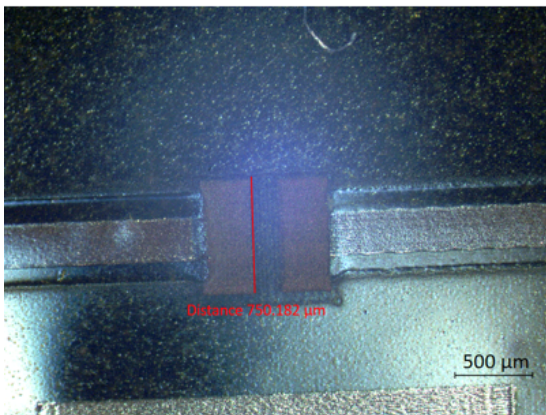


Figure 5.1: (a) Circuit schematic of the complementary organic NOT gate. (b) Cross section of the 3D printed inverter. Not pictured: the in-plane gold gates that would be found in plane with the Au contact but behind the cross section (looking into the page). (c) 2D top-down view of the layout of the complementary organic NOT gate circuit.

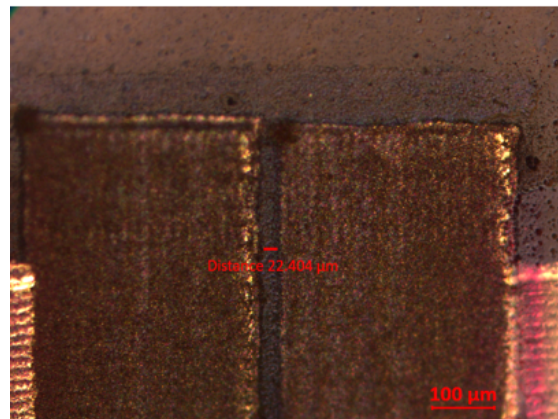
Figure 5.2 (a) shows a photograph of a printed complementary inverter with the NDI device under test. It can be seen that the NDI channel is noticeably shorter in length than the PEDOT:PSS channel above it. The difference is illustrated in Figures 5.2 (b) and (c), where microscope images of each channel are shown in more detail. Images were taken with a Zeiss Axio microscope with Zeiss Axiocam and Zen software. Figure 5.2 (b) shows an image of a PEDOT:PSS channel under 2.5x magnification with a measurement of the channel width, which is approximately  $750\ \mu\text{m}$  as designed. Figure 5.2 (c) shows an image of an NDI channel under 10x magnification with a measurement of the channel length, which is noticeably shorter than the channel length of the PEDOT:PSS in Figure 5.2 (b), and is measured to be approximately  $22\ \mu\text{m}$ .



(a)



(b)



(c)

Figure 5.2: (a) Photograph of the printed complementary inverter with NDI channel under test. (b) Microscope image of PEDOT:PSS channel with width measured. (c) Microscope image of gNDI-Br<sub>2</sub> channel with length measured.

## 5.4 Results and Discussion

### 5.4.1 Individual OECT Characterization

Both the p-type and n-type devices in the printed inverter were characterized individually/separately to gain insight into the crucial characteristics needed to match them. The  $I_D$ - $V_D$  curves are shown in Figure 5.3. As expected, the p-type depletion mode device's current decreases with an increase in gate voltage while the n-type enhancement mode device's current increases. This is ideal for the proper function of a complementary gate. However, it can be seen that even with optimizations, the currents of the devices are quite mismatched. The PEDOT:PSS was purposefully degraded as mentioned in Section 5.2.1 - the ingredient ratios were modified and only one layer was printed in order to worsen the performance of the device.

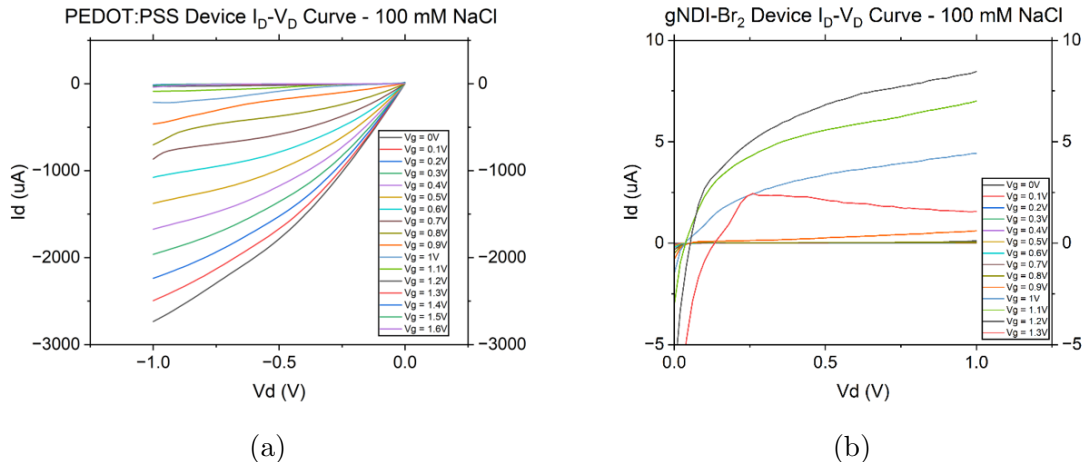


Figure 5.3:  $I_D$ - $V_D$  curves of printed (a) PEDOT:PSS and (b) gNDI-Br<sub>2</sub> devices.

As can be seen in Figures 5.3 (a) and 5.4 (a), even with the performance degradation, the PEDOT:PSS OECT still outperforms the NDI OECT by a wide margin. The maximum current level through the PEDOT:PSS device was lowered to  $\sim 3$  mA, as opposed to  $\sim 90$  mA as demonstrated in the previous chapter. The transconductance was lowered to 2.99 mS as a result, down from a maximum of 117 mS as demonstrated in the previous chapter. However, the performances of the p and n-type devices are still mismatched due to the low performance of the n-type device.

The NDI device exhibits a maximum current of  $8.46 \mu\text{A}$ , which is nearly an order of magnitude less than the maximum current of the PEDOT:PSS. The peak transconductance was found to be  $38 \mu\text{S}$ . The low performance of the NDI can be attributed to the conductivity of the film, which is based on an n-type small molecule. Intrinsically, these types of materials do not exhibit conductivity as high as polymeric p-type materials. Additionally, the NDI device exhibits a phenomena where it begins to turn off again after a certain gate voltage. As can be seen in Figure 5.3 (b), the maximum current level is at a gate voltage of  $1.2\text{V}$ , and then decreases again at  $1.3\text{V}$  (the curve indicated in red). This complicates circuit behavior and is explored further in Section 5.4.2.

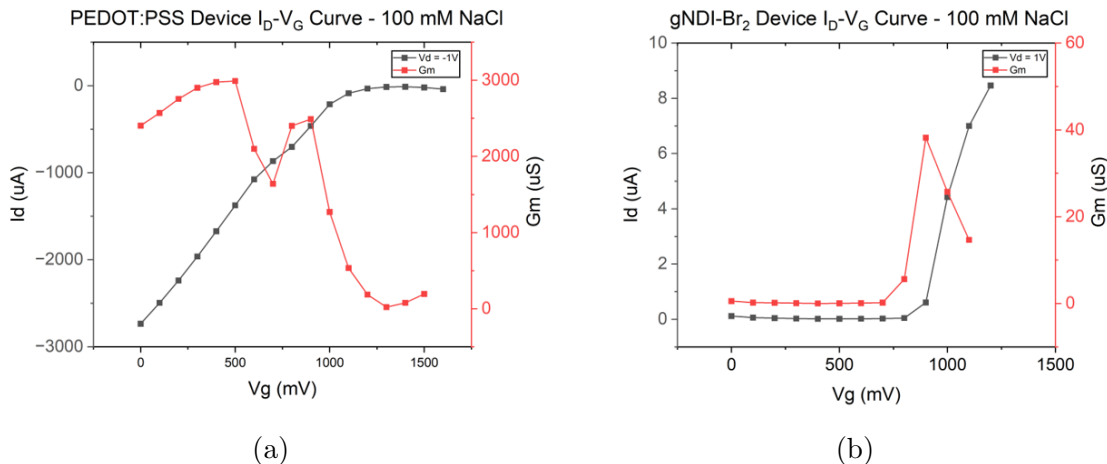


Figure 5.4:  $I_D$ - $V_G$  and transconductance curves of printed (a) PEDOT:PSS and (b) gNDI- $\text{Br}_2$  devices.

The threshold voltages of each device were also extracted from the  $I_D$ - $V_G$  curves as demonstrated in Figures 5.5 (a) and (b). For the PEDOT:PSS device, the threshold was slightly lowered to  $1.29\text{V}$  compared to the previous chapter where the threshold was found to be approximately  $1.49\text{V}$ . This is due to the number of layers printed (1 layer for the devices in this chapter vs. 10 in the previous chapter). With fewer layers, the thickness of the film decreases, and thus less material is required to be de-doped to turn the device off. As a result, a lower amount of ions is required to fully turn off the device, which translates to a lower threshold voltage. For the NDI device, the

threshold was calculated to be approximately 0.86V. Although not perfectly matched, for the purposes of an inverter, the thresholds are close enough to trigger switching in the  $\sim 1V$  range of input voltage.

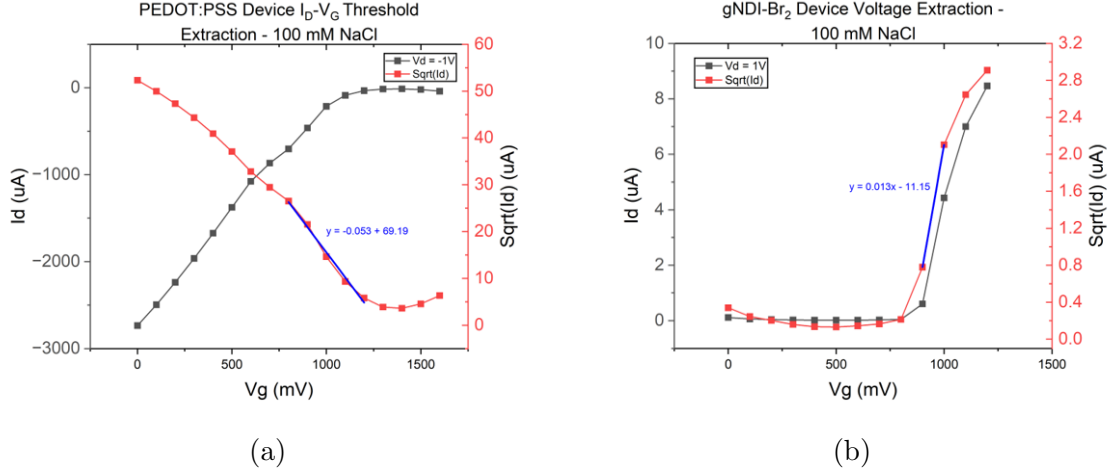


Figure 5.5:  $I_D$ - $V_G$  curves and voltage extraction of printed (a) PEDOT:PSS and (b) gNDI-Br<sub>2</sub> devices.

## 5.4.2 NOT Gate Performance

After individual characterization, NOT gate sweeps were carried out in a fashion similar to the sweeps carried out in the previous chapter, with 100 mM NaCl solution dropped on both channels as the electrolyte. For the sake of consistency, a drain voltage of 300 mV was again used as the power supply voltage and the input voltage was swept from 0V to 1.4V in increments of 0.1V. The output behavior is shown in Figure 5.6. As shown by the output curve, the output high level is now 300 mV, as opposed to the degraded output level in the previous chapter. Other experimental sweeps showed that different drain voltages and thus output high levels as high as 1V are also possible with this configuration. As the input voltage value becomes closer to the switching threshold of both devices, the curve tends towards the low voltage level, but is not lowered completely to 0V. At approximately 1.3V, the curve begins to switch back towards the high level. This is due to the behavior of the NDI device - at 1.3V, the device current begins to decrease, turning the device off again. Additionally,

the output level only is able to decrease to approximately 293 mV before increasing to 300 mV again. This is because of the mismatch in current levels between both devices. Since the NDI channel can only support a small amount of current in its on state, the drain-to-source on resistance,  $R_{DS, ON}$ , is still higher than the off-state resistance of the PEDOT:PSS device due to its off-current. As a result, Ohm's law and the voltage divider effect dictate that the output voltage will still be closer to the supply voltage than to 0V. Further optimizations are needed to adjust voltage levels, but Figure 5.6 does demonstrate successful theoretical switching behavior for two complementary devices, as both n and p-type devices are shown to affect the final output.

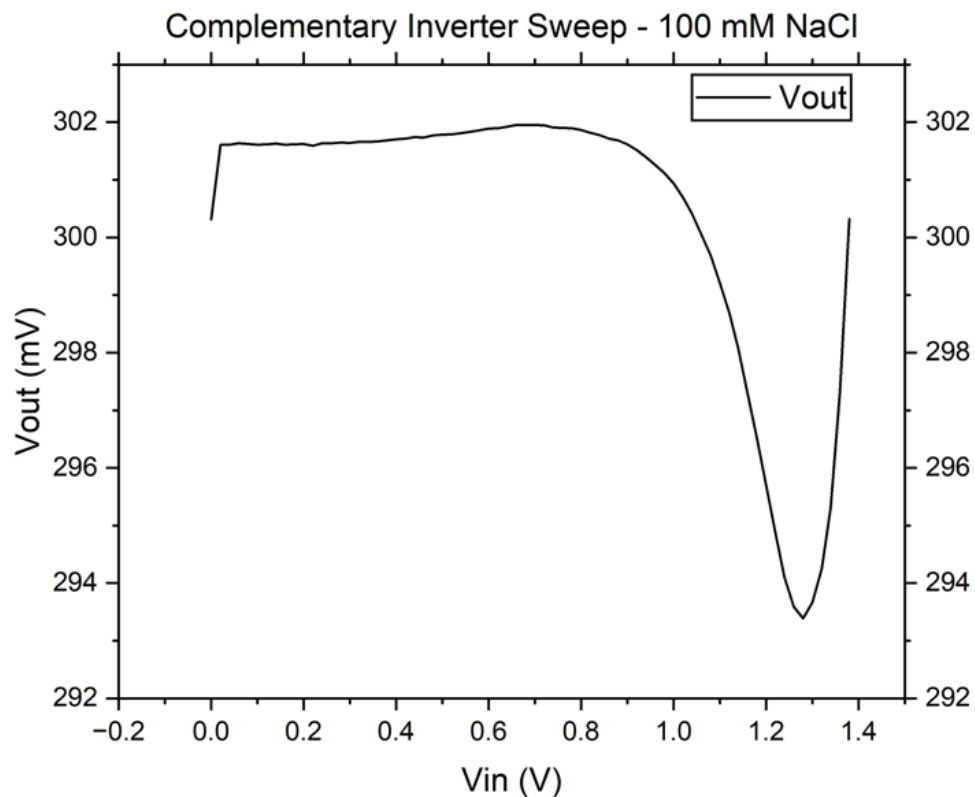


Figure 5.6: NOT gate sweep of the printed complementary gate.

### 5.4.3 Future Optimizations

As discussed in the previous section, the correct operation of a complimentary printed OECT inverter was confirmed; however, the output voltage levels are not yet useful for logical operation. In order to have the entire range of voltage available at the output, either the performance of the PEDOT:PSS must be further worsened or the performance of the NDI must be enhanced. Additionally, another p-type material may be used. In order to degrade the PEDOT:PSS, multiple strategies may be employed, such as over-oxidation of PEDOT:PSS, increasing of the W/L ratio, and further modification of the PEDOT:PSS recipe. Over-oxidation of PEDOT:PSS has been demonstrated and has even resulted in PEDOT OECT devices operating in the accumulation mode [133]. Increasing the W/L ratio is also a viable and preferred strategy, especially with the quick prototyping capabilities of aerosol jet printing. The width and length were arbitrarily chosen to be 750  $\mu\text{m}$  and  $\mu\text{m}$  due to the ease of printing and imaging of the channel. The width can easily be modified to be shorter than the length, and the length can be elongated indefinitely to increase the resistance of the channel significantly, which would result in a smaller current. The PEDOT:PSS recipe can also be modified to decrease or remove the concentration of ethylene glycol in the solution to decrease the conductivity, but this is not preferred due to the possibility of the need for reoptimization of printing parameters. In order to enhance the performance of the NDI device, more layers of channel can be printed in order to increase the thickness of the channel and increase the current-carrying capability. Further shrinking of the channel length is also a possibility, but is not preferred due to the challenge in achieving the length that has already been printed for the NDI devices in this chapter. Because of this, increasing the width of the channel is preferred in order to increase the W/L, but may be an issue if the devices need to be miniaturized for the final application.

Another consideration in achieving optimal logical operation for these devices is in

the threshold optimization. Ideally, the thresholds of both devices are the same in order to create a clean transition from high to low, or low to high. For example, if one were to use a power supply voltage of 1V, sweeping the input voltage from 0 to 1V should result in a transition from high to low that would cover the entire range roughly symmetrically, i.e, the transition would happen roughly at 0.5V and the graph would be symmetrical around this point. For this kind of device, both thresholds of p and n-type devices would be around 0.5V. The output voltage could then be passed to the next stage of logic and is enough for the devices in the next stage to turn on or off. In this work, the thresholds are close but do not match exactly (1.29V for the p-type and 0.86V for the n-type device). To decrease or increase a threshold voltage, a larger or smaller gate size area could be used [1]. Additionally, using OECTs allows the editing of threshold levels based on the electrolyte dropped on the channel. With a higher concentration of ions in electrolyte, the threshold voltage would be lower and vice versa. This provides a simple way of matching threshold levels since electrolyte can easily be removed from and added to the structure.

## 5.5 Conclusion

In this chapter, complimentary logical NOT gates were built using p-type and n-type OECTs. In addition to the same kinds of p-type devices demonstrated in the previous chapter, gNDI-Br<sub>2</sub>-based OECTs were fully printed using aerosol jet printed and successfully demonstrated with a minimum channel length of 22  $\mu\text{m}$  in order to enhance their performance. Both p and n-type devices were included in a NOT gate design and tested in a circuit configuration. Correct switching behavior was observed, but was limited in terms of the logical levels that were outputted as well as the voltage threshold matching. Future work can focus on optimizing and matching the device characteristics as described in Section 5.4.3. Once this is achieved, larger complimentary gates can easily be designed such as NAND and NOR gates. From these, larger circuits such as multiplexers and ring oscillators can be built. Finally,

these devices can be included in larger biosensing circuits by moving digital processing on-board without the need for external circuits. For this, the circuits built can be printed with contact pads to be interfaced with flexible connector boards as already demonstrated in Chapter 3.

# Chapter 6

## Conclusion

### 6.1 Summary

In this thesis, various electronic devices were 3D-printed using aerosol jet printing. The purpose of this fabrication method is to realize economical, reliable, and repeatable devices that can be used for a variety of applications, such as biosensing and digital logic, both of which are demonstrated in this thesis. The work focuses mainly on organic semiconductors, namely the development of printed organic electrochemical transistors, but also includes a passive resistive sensor. This aimed to demonstrate the versatility of aerosol jet printing as a fabrication method for different kinds of devices. In addition, results are shown that demonstrate the viability of 3D printed devices as wearable biosensors. Overall, aerosol jet printing was shown to be an effective method that can be used to prototype devices at a much faster rate than traditional fabrication methods such as photolithography.

In Chapter 3, the passive resistive temperature sensor was designed, fabricated and tested. Aerosol jet printing was used to print gold electrodes/contacts and a polyimide well to contain the drop-casted sensing material, a nanocomposite of multi-walled carbon nanotubes and a thermoplastic. Optimizations for the weight ratio of the nanocomposite mixture were carried out extensively and the final mixtures were characterized with thermogravimetric analysis, UV-Vis spectrophotometry, and scanning electron microscopy. It was found that the devices exhibited high linearity

and a maximum sensitivity of  $237 \Omega/^{\circ}\text{C}$ , with a negative temperature coefficient of  $-0.00134 \text{ K}^{-1}$ . This optimized sensor was also printed with a connector land pattern with the goal of interfacing with a flexible connector board, which was also designed as a part of this work. In addition to heating tests performed on a hot plate, the sensor was tested on the author's skin temperature as a means of verifying the sensor's performance as a flexible biosensor. The results demonstrate that the sensor is an excellent candidate for a cheap, disposable, and biocompatible biosensor that may be fabricated quickly via aerosol jet printing.

In Chapter 4, logic gates based on organic electrochemical transistors were fabricated using aerosol jet printing. In contrast to the previous chapter, the devices were fully 3D printed, including the channel sensing material. First, OECT devices with PEDOT:PSS as the channel material were individually fabricated and optimized in order to gain insight into their individual parameters. It was found that using aerosol jet printing, devices exhibited extremely high transconductance for planar devices (up to  $117 \text{ mS}$ ) which led to high sensing performance. In order to create useful biosensors, NOT gates were built using these OECTs with one channel material. The NOT gates provided a voltage rather than a current output, simplifying data processing requirements. Ion sensitivity tests were conducted with 4 different ion types. The highest sensitivity reported was  $570 \text{ mV/dec}$  when sensing NaCl in the 1-10 mM range. To minimize the need for dropping electrolyte on one of the two transistors during real-world testing, the effect of dropping a hydrogel on one of the two transistors in the circuit was explored and was found to lower the sensitivity of the device. Devices were also built to be sensitive to glucose, providing a useful biosensing application. The maximum sensitivity was found to be  $35 \text{ mV/dec}$  in the 1-10 mM range. This work builds on the work in the previous chapter in terms of demonstrating viable biosensors using aerosol jet printing. It also confirms aerosol jet printing as a premier method of fabrication for OECTs, as it features the highest transconductance for a planar OECT at the time of writing.

In Chapter 5, logic gates were built using two channel materials, resulting in a complementary NOT gate. In contrast to the previous chapter, the pull-down transistor device was fabricated with an n-type small molecule semiconductor, gNDI-Br<sub>2</sub>. Both n-type and p-type devices were individually characterized due to the need for proper transistor matching in order to create a useful logic gate. A successful fully 3D printed NDI was demonstrated after shrinking the channel size to a minimum of 22  $\mu\text{m}$ , due to the poor performance of the small-molecule organic semiconductor. After building an inverter using OECTs with both materials, it was found that the mismatch between the two devices was too great for the NOT gate to perform useful logical operation, but the correct switching behavior was confirmed using NOT sweeps. This work builds upon the previous chapter by focusing on building 3D printed NOT gates purely for digital logic applications, since the devices in the previous chapter were useful for biosensing but not for logical operation. The chapter also emphasizes the difficulty of building organic complementary logic circuits and specifically the non-trivial nature of increasing the performance of n-type organic semiconductors.

Overall, the devices in the separate chapters have slightly different applications but can be interfaced together. Since aerosol jet printing was confirmed as a viable fabrication method for these kinds of devices, it can be used to create larger platforms that include all these devices.

## 6.2 Future Work

### 6.2.1 Temperature Sensor

The greatest difficulty in the development of this device was the consistency of results. Due to the random nature of the orientation of the carbon nanotubes in the matrix, this factor will always be present, however, drop-casting of the dispersion onto the printed device creates more inconsistency in results due to the inconsistent spread of the dispersion as well as the coffee ring effect. This was minimized in the work by the printing of the polyimide well, but can be reduced even further by 3D printing of the nanocomposite dispersion itself. This was not done in this work due to the time-consuming nature of optimizing printing parameters for a new aerosol. In addition, the average length of the nanotubes in this work was approximately  $10\ \mu\text{m}$ , which is larger than the size of the aerosol particles ( $1\ \mu\text{m}$ ). This would result in non-uniform printing, or even a complete lack of printing deposition. Future work could focus on obtaining a nanocomposite dispersion using shorter nanotubes as well as optimizing printing parameters for this dispersion. This would result in a fully 3D printed temperature sensor which would minimize the effects of overspread of drop-casting and create more consistency in both measurement and repeatability.

### 6.2.2 Depletion-mode Logic Gates

The devices demonstrated in this work exhibited high sensitivity due to the use of PEDOT:PSS in both channel materials with an extremely high transconductance. This can be exploited to sense a variety of analytes. This work has already shown the devices can be functionalized to sense glucose molecules, but these are preliminary results without optimized sensitivity. Future work can focus on increasing the sensitivity of glucose sensing, as well as developing functionalization schemes for different analytes. The hydrogel that was included in the structure of some of the devices also proved to be useful in simplifying measurement for real-world applications, but

decreased sensitivity. Future work could focus on optimizing hydrogel recipes to increase both stability and permeability of the gel. This would help in avoiding evaporation/dehydration of the gel as well as allowing ions to easily penetrate the film, maintaining the same sensitivity and device characteristics as the device would have pre-hydrogel treatment.

### **6.2.3 Complimentary Logic Gates**

As evidenced in Chapter 5, the process of matching the characteristics of two separate n and p-type organic materials is not trivial. Since the printing of an NDI OECT was already optimized, future work would most likely focus on further degrading the performance of PEDOT:PSS. In the event that the mismatch between devices is still too great, replacing one of the materials would be the next course of action, which is not preferable due to the optimization of printing parameters for a new ink. Since it is unlikely that any other n-type material could achieve the performance of the degraded PEDOT:PSS (PEDOT:PSS is one of, if not the highest performing p-type polymers demonstrated throughout the literature), it would be preferable to replace the PEDOT:PSS and optimize a new p-type material. Once this is done and complementary devices are optimized for logical operation, it would be much easier to build more complex circuits such as NAND and NOR gates, multiplexers and decoders, since the only difference would be in the amount of transistors per circuit and how they are connected/configured. Printing logical circuits on flexible substrate could open the way to simpler on-board processing of biosensor devices.

### **6.2.4 Biosensing Platform**

As discussed previously, the different devices built in this thesis could be included in a larger platform. Wearable devices have already been demonstrated to sense multiple analytes in the literature as well as in commercial devices [2, 3]. A potential biosensor platform built with the devices in this work could include temperature sensing, ion

sensing, and glucose sensing, as well as a complimentary logic-based multiplexer to switch between each signal. The voltage output of each of these devices would make it easy to multiplex each signal and read it using digital processing circuitry. A device like this would make it simple to collect data, such as medical information, at a continuous rate. However, this kind of platform would require each sensor to be fully optimized and robust in order to accurately collect and predict information. The optimizations listed in the previous sections would greatly aid this. Future work would focus on optimizing printing of all sensors on one substrate and minimizing the footprint of each one. This may not be a trivial process as printing multiple devices would take more time and would thus be more tedious to prototype, with more potential for defects that can render entire devices useless.

# Bibliography

- [1] J. Fan, “Biosensor development using organic electrochemical transistors (oects) fabricated via printing techniques,” PhD thesis, University of Alberta, Edmonton, Canada, 2021.
- [2] T. Stuart, J. Hanna, and P. Gutruf, “Wearable devices for continuous monitoring of biosignals: Challenges and opportunities,” *APL Bioengineering*, vol. 6, p. 021502, 2 Jun. 2022, ISSN: 2473-2877. DOI: 10.1063/5.0086935. [Online]. Available: <https://aip.scitation.org/doi/10.1063/5.0086935>.
- [3] L. Wang, K. Jiang, and G. Shen, “Wearable, implantable, and interventional medical devices based on smart electronic skins,” *Advanced Materials Technologies*, vol. 6, p. 2100107, 6 Jun. 2021, ISSN: 2365-709X. DOI: 10.1002/admt.202100107. [Online]. Available: <https://onlinelibrary.wiley.com/doi/10.1002/admt.202100107>.
- [4] B. J. Privett, J. H. Shin, and M. H. Schoenfisch, “Electrochemical sensors,” *Analytical Chemistry*, vol. 82, pp. 4723–4741, 12 Jun. 2010, ISSN: 0003-2700. DOI: 10.1021/ac101075n. [Online]. Available: <https://pubs.acs.org/doi/10.1021/ac101075n>.
- [5] J. F. Tressler, S. Alkoy, and R. E. Newnham, “Piezoelectric sensors and sensor materials,” *Journal of Electroceramics*, vol. 2, 4 1998. DOI: <https://doi.org/10.1023/A:1009926623551>.
- [6] P. Wang, W. Chen, F. Wan, J. Wang, and J. Hu, “A review of cavity-enhanced raman spectroscopy as a gas sensing method,” *Applied Spectroscopy Reviews*, vol. 55, pp. 393–417, 5 May 2020, ISSN: 0570-4928. DOI: 10.1080/05704928.2019.1661850. [Online]. Available: <https://www.tandfonline.com/doi/full/10.1080/05704928.2019.1661850>.
- [7] V. Acha, M. Meurens, H. Naveau, and S. N. Agathos, “Atr-ftir sensor development for continuous on-line monitoring of chlorinated aliphatic hydrocarbons in a fixed-bed bioreactor,” *Biotechnology and Bioengineering*, vol. 68, pp. 473–487, 5 Jun. 2000, ISSN: 0006-3592. DOI: 10.1002/(SICI)1097-0290(20000605)68:5<473::AID-BIT1>3.0.CO;2-8. [Online]. Available: [https://onlinelibrary.wiley.com/doi/10.1002/\(SICI\)1097-0290\(20000605\)68:5<473::AID-BIT1>3.0.CO;2-8](https://onlinelibrary.wiley.com/doi/10.1002/(SICI)1097-0290(20000605)68:5<473::AID-BIT1>3.0.CO;2-8).

- [8] C. Cao, J. B. Andrews, and A. D. Franklin, "Completely printed, flexible, stable, and hysteresis-free carbon nanotube thin-film transistors via aerosol jet printing," *Advanced Electronic Materials*, vol. 3, p. 1700057, 5 May 2017, ISSN: 2199160X. DOI: 10.1002/aelm.201700057. [Online]. Available: <https://onlinelibrary.wiley.com/doi/10.1002/aelm.201700057>.
- [9] Y. Li, Y. Mao, C. Xiao, X. Xu, and X. Li, "Flexible ph sensor based on a conductive pani membrane for ph monitoring," *RSC Advances*, vol. 10, pp. 21–28, 1 2020, ISSN: 2046-2069. DOI: 10.1039/C9RA09188B. [Online]. Available: <http://xlink.rsc.org/?DOI=C9RA09188B>.
- [10] Y.-C. Tsai, S.-C. Li, and J.-M. Chen, "Cast thin film biosensor design based on a nafion backbone, a multiwalled carbon nanotube conduit, and a glucose oxidase function," *Langmuir*, vol. 21, pp. 3653–3658, 8 Apr. 2005, ISSN: 0743-7463. DOI: 10.1021/la0470535. [Online]. Available: <https://pubs.acs.org/doi/10.1021/la0470535>.
- [11] S. Wen, H. Heidari, A. Vilouras, and R. Dahiya, "A wearable fabric-based rfid skin temperature monitoring patch," *IEEE*, Oct. 2016, pp. 1–3, ISBN: 978-1-4799-8287-5. DOI: 10.1109/ICSENS.2016.7808919. [Online]. Available: <http://ieeexplore.ieee.org/document/7808919/>.
- [12] H. Lee *et al.*, "A graphene-based electrochemical device with thermoresponsive microneedles for diabetes monitoring and therapy," *Nature Nanotechnology*, vol. 11, pp. 566–572, 6 Jun. 2016, ISSN: 17483395. DOI: 10.1038/NNANO.2016.38.
- [13] C. Wang, H. Dong, L. Jiang, and W. Hu, "Organic semiconductor crystals," *Chemical Society Reviews*, vol. 47, pp. 422–500, 2 2018, ISSN: 0306-0012. DOI: 10.1039/C7CS00490G. [Online]. Available: <http://xlink.rsc.org/?DOI=C7CS00490G>.
- [14] L. Torsi, M. Magliulo, K. Manoli, and G. Palazzo, "Organic field-effect transistor sensors: A tutorial review," *Chemical Society Reviews*, vol. 42, p. 8612, 22 2013, ISSN: 0306-0012. DOI: 10.1039/c3cs60127g. [Online]. Available: <http://xlink.rsc.org/?DOI=c3cs60127g>.
- [15] D. Elkington, N. Cooling, W. Belcher, P. Dastoor, and X. Zhou, "Organic thin-film transistor (otft)-based sensors," *Electronics*, vol. 3, pp. 234–254, 2 Apr. 2014, ISSN: 2079-9292. DOI: 10.3390/electronics3020234. [Online]. Available: <http://www.mdpi.com/2079-9292/3/2/234>.
- [16] R. B. Rashid, X. Ji, and J. Rivnay, "Organic electrochemical transistors in bioelectronic circuits," *Biosensors and Bioelectronics*, vol. 190, p. 113461, Oct. 2021, ISSN: 09565663. DOI: 10.1016/j.bios.2021.113461. [Online]. Available: <https://linkinghub.elsevier.com/retrieve/pii/S095656632100498X>.
- [17] R. Granelli *et al.*, "High-performance bioelectronic circuits integrated on biodegradable and compostable substrates with fully printed mask-less organic electrochemical transistors," 2022. DOI: 10.1002/smll.202108077. [Online]. Available: [www.small-journal.com](http://www.small-journal.com).

- [18] D. Majak, J. Fan, and M. Gupta, “Fully 3d printed oect based logic gate for detection of cation type and concentration,” *Sensors and Actuators, B: Chemical*, vol. 286, pp. 111–118, May 2019, ISSN: 09254005. DOI: 10.1016/J.SNB.2019.01.120.
- [19] R. Ratnesh, A Goel, G Kaushik, H Garg, M Singh, and B Prasad, “Advancement and challenges in mosfet scaling,” 2021. DOI: 10.1016/j.mssp.2021.106002. [Online]. Available: <https://doi.org/10.1016/j.mssp.2021.106002>.
- [20] Y. Liao *et al.*, “The research on the fabrication of the novel basic unit for 3d structure integrated circuit,” *Journal of Physics: Conference Series*, vol. 2524, p. 012035, 1 Jun. 2023, ISSN: 1742-6588. DOI: 10.1088/1742-6596/2524/1/012035. [Online]. Available: <https://iopscience.iop.org/article/10.1088/1742-6596/2524/1/012035>.
- [21] D. D. ELEY, “Phthalocyanines as semiconductors,” *Nature*, vol. 162, pp. 819–819, 4125 Nov. 1948, ISSN: 0028-0836. DOI: 10.1038/162819a0.
- [22] J. Hwang *et al.*, “Donor engineered deep-blue emitters for tuning luminescence mechanism in solution-processed oleds,” *Chemical Engineering Journal*, vol. 416, pp. 1385–8947, 2021. DOI: 10.1016/j.cej.2021.129185. [Online]. Available: <https://doi.org/10.1016/j.cej.2021.129185>.
- [23] T. Taima *et al.*, “Sexithiophene-based photovoltaic cells with high light absorption coefficient via crystalline polymorph control,” *The Journal of Physical Chemistry C*, vol. 121, pp. 19 699–19 704, 36 Sep. 2017, ISSN: 1932-7447. DOI: 10.1021/acs.jpcc.7b07953.
- [24] F. Ortman, F. Bechstedt, and K. Hannewald, “Charge transport in organic crystals: Interplay of band transport, hopping and electron–phonon scattering,” *New Journal of Physics*, vol. 12, p. 023011, 2 Feb. 2010, ISSN: 1367-2630. DOI: 10.1088/1367-2630/12/2/023011.
- [25] F. Reines and H. W. Sobel, “Test of the pauli exclusion principle for atomic electrons,” *Physical Review Letters*, vol. 32, pp. 954–954, 17 Apr. 1974, ISSN: 0031-9007. DOI: 10.1103/PhysRevLett.32.954.
- [26] M. Brinkmann, L. Hartmann, L. Biniek, K. Tremel, and N. Kayunkid, “Orienting semi-conducting pi-conjugated polymers,” *Macromolecular Rapid Communications*, vol. 35, pp. 9–26, 1 Jan. 2014, ISSN: 10221336. DOI: 10.1002/marc.201300712.
- [27] A. Moliton and R. C. Hiorns, “Review of electronic and optical properties of semiconducting pi-conjugated polymers: Applications in optoelectronics,” *Polymer International*, vol. 53, pp. 1397–1412, 10 Oct. 2004, ISSN: 0959-8103. DOI: 10.1002/pi.1587.
- [28] P. von Ragué Schleyer, “Introduction: Delocalization pi and sigma,” *Chemical Reviews*, vol. 105, pp. 3433–3435, 10 Oct. 2005, ISSN: 0009-2665. DOI: 10.1021/cr030095y.

- [29] S. Y. Son *et al.*, “High-field-effect mobility of low-crystallinity conjugated polymers with localized aggregates,” *Journal of the American Chemical Society*, vol. 138, pp. 8096–8103, 26 Jul. 2016, ISSN: 0002-7863. DOI: 10.1021/jacs.6b01046.
- [30] T. Heumueller *et al.*, “Reducing burn-in voltage loss in polymer solar cells by increasing the polymer crystallinity,” *Energy Environ. Sci.*, vol. 7, pp. 2974–2980, 9 2014, ISSN: 1754-5692. DOI: 10.1039/C4EE01842G.
- [31] D. T. Scholes *et al.*, “The effects of crystallinity on charge transport and the structure of sequentially processed f4 tcnq-doped conjugated polymer films,” *Advanced Functional Materials*, vol. 27, p. 1702654, 44 Nov. 2017, ISSN: 1616-301X. DOI: 10.1002/adfm.201702654.
- [32] N. P. Bradshaw *et al.*, “Aerosol-jet-printable covalent organic framework colloidal inks and temperature-sensitive nanocomposite films,” *Advanced Materials*, Jun. 2023, ISSN: 0935-9648. DOI: 10.1002/adma.202303673.
- [33] B. Lussem, M. Riede, and K. Leo, “Doping of organic semiconductors,” *physica status solidi (a)*, vol. 210, pp. 9–43, 1 Jan. 2013, ISSN: 18626300. DOI: 10.1002/pssa.201228310.
- [34] I. Salzmann, G. Heimel, M. Oehzelt, S. Winkler, and N. Koch, “Molecular electrical doping of organic semiconductors: Fundamental mechanisms and emerging dopant design rules,” *Accounts of Chemical Research*, vol. 49, pp. 370–378, 3 Mar. 2016, ISSN: 0001-4842. DOI: 10.1021/acs.accounts.5b00438.
- [35] J. Chen, W. Zhang, L. Wang, and G. Yu, “Recent research progress of organic small-molecule semiconductors with high electron mobilities,” *Advanced Materials*, vol. 35, 11 Mar. 2023, ISSN: 0935-9648. DOI: 10.1002/adma.202210772.
- [36] S. Griggs, A. Marks, H. Bristow, and I. McCulloch, “N-type organic semiconducting polymers: Stability limitations, design considerations and applications,” *Journal of Materials Chemistry C*, vol. 9, pp. 8099–8128, 26 2021, ISSN: 2050-7526. DOI: 10.1039/D1TC02048J.
- [37] O. D. Jurchescu, J. Baas, and T. T. M. Palstra, “Effect of impurities on the mobility of single crystal pentacene,” *Applied Physics Letters*, vol. 84, pp. 3061–3063, 16 Apr. 2004, ISSN: 0003-6951. DOI: 10.1063/1.1704874.
- [38] H. Mu, W. Li, R. Jones, A. Steckl, and D. Klotzkin, “A comparative study of electrode effects on the electrical and luminescent characteristics of alq3/tpd oled: Improvements due to conductive polymer (pedot) anode,” *Journal of Luminescence*, vol. 126, pp. 225–229, 1 Sep. 2007, ISSN: 0022-2313. DOI: 10.1016/J.JLUMIN.2006.07.005.
- [39] J. E. Knox, M. D. Halls, H. P. Hratchian, and H. B. Schlegel, “Chemical failure modes of alq3-based oleds: Alq3 hydrolysis,” *Physical Chemistry Chemical Physics*, vol. 8, pp. 1371–1377, 12 Mar. 2006, ISSN: 1463-9084. DOI: 10.1039/B514898G. [Online]. Available: <https://pubs.rsc.org/en/content/articlehtml/2006/cp/b514898g><https://pubs.rsc.org/en/content/articlelanding/2006/cp/b514898g>.

- [40] T. D. Anthopoulos, D. M. D. Leeuw, E. Cantatore, P. V. Hof, J. Alma, and J. C. Hummelen, "Solution processible organic transistors and circuits based on a c 70 methanofullerene," *Journal of Applied Physics*, vol. 98, p. 54503, 5 Sep. 2005, ISSN: 00218979. DOI: 10.1063/1.2034083/291934. [Online]. Available: /aip/jap/article/98/5/054503/291934/Solution-processible-organic-transistors-and.
- [41] G. W. Ludwig and R. L. Watters, "Drift and conductivity mobility in silicon," *Physical Review*, vol. 101, pp. 1699–1701, 6 Mar. 1956, ISSN: 0031-899X. DOI: 10.1103/PhysRev.101.1699. [Online]. Available: <https://link.aps.org/doi/10.1103/PhysRev.101.1699>.
- [42] G. Horowitz, M. E. Hajlaoui, and R. Hajlaoui, "Temperature and gate voltage dependence of hole mobility in polycrystalline oligothiophene thin film transistors," *Journal of Applied Physics*, vol. 87, pp. 4456–4463, 9 May 2000, ISSN: 0021-8979. DOI: 10.1063/1.373091. [Online]. Available: <https://pubs.aip.org/aip/jap/article/87/9/4456-4463/489324>.
- [43] D. Xia *et al.*, "Oligofluorene with multiple spiro-connections: Its and their use in blue and white oleds," *New Journal of Chemistry*, vol. 43, pp. 3788–3792, 9 2019, ISSN: 1144-0546. DOI: 10.1039/C8NJ06135A. [Online]. Available: <http://xlink.rsc.org/?DOI=C8NJ06135A>.
- [44] Y. Furusho and E. Yashima, "Synthesis and function of double-stranded helical polymers and oligomers," *Macromolecular Rapid Communications*, vol. 32, pp. 136–146, 2 Jan. 2011, ISSN: 10221336. DOI: 10.1002/marc.201000533.
- [45] U Bielecka, P Lutsyk, K Janus, J Sworakowski, and W Bartkowiak, "Effect of solution aging on morphology and electrical characteristics of regioregular p3ht fets fabricated by spin coating and spray coating," 2011. DOI: 10.1016/j.orgel.2011.06.027.
- [46] Y. Zhang, X. Yao, and Y. Cui, "Chemical and biological sensors a dpp-dtt field-effect transistor-based biosensor for detecting interleukin-6," vol. 7, p. 4500104, 1 2023. DOI: 10.1109/LSENS.2022.3224950. [Online]. Available: <https://www.ieee.org/publications/rights/index.html>.
- [47] S. Liu *et al.*, "Enhanced efficiency of polymer solar cells by adding a high-mobility conjugated polymer," *Energy and Environmental Science*, vol. 8, pp. 1463–1470, 5 May 2015, ISSN: 17545706. DOI: 10.1039/C5EE00090D. [Online]. Available: <https://pubs.rsc.org/en/content/articlehtml/2015/ee/c5ee00090d><https://pubs.rsc.org/en/content/articlelanding/2015/ee/c5ee00090d>.
- [48] F. S. Kim, C. H. Park, Y. Na, and S. A. Jenekhe, "Effects of ladder structure on the electronic properties and field-effect transistor performance of poly(benzobisimidazobenzophenanthroline)," *Organic Electronics*, vol. 69, pp. 301–307, Jun. 2019, ISSN: 15661199. DOI: 10.1016/j.orgel.2019.03.049. [Online]. Available: <https://linkinghub.elsevier.com/retrieve/pii/S1566119919301582>.

- [49] B. D. Paulsen, K. Tybrandt, E. Stavrinidou, and J. Rivnay, “Organic mixed ionic–electronic conductors,” *Nature Materials*, vol. 19, pp. 13–26, 1 Jan. 2020, ISSN: 1476-1122. DOI: 10.1038/s41563-019-0435-z. [Online]. Available: <https://www.nature.com/articles/s41563-019-0435-z>.
- [50] R. delOlmo, T. C. Mendes, M. Forsyth, and N. Casado, “Mixed ionic and electronic conducting binders containing pedot:pss and organic ionic plastic crystals toward carbon-free solid-state battery cathodes,” *Journal of Materials Chemistry A*, vol. 10, pp. 19 777–19 786, 37 2022, ISSN: 2050-7488. DOI: 10.1039/D1TA09628A.
- [51] S. Hazra, A. Banerjee, and A. K. Nandi, “Organic mixed ion-electron conductivity in polymer hybrid systems,” vol. 17, p. 3, 2023. DOI: 10.1021/acsomega.2c04516. [Online]. Available: <http://pubs.acs.org/journal/acsofd>.
- [52] D. Bernards and G. Malliaras, “Steady-state and transient behavior of organic electrochemical transistors,” *Advanced Functional Materials*, vol. 17, pp. 3538–3544, 17 Nov. 2007, ISSN: 1616301X. DOI: 10.1002/adfm.200601239.
- [53] K. Sun *et al.*, “Review on application of pedots and pedot:pss in energy conversion and storage devices,” *Journal of Materials Science: Materials in Electronics*, vol. 26, pp. 4438–4462, 7 Jul. 2015, ISSN: 0957-4522. DOI: 10.1007/s10854-015-2895-5.
- [54] L. Hu, J. Song, X. Yin, Z. Su, and Z. Li, “Research progress on polymer solar cells based on pedot:pss electrodes,” *Polymers*, vol. 12, p. 145, 1 Jan. 2020, ISSN: 2073-4360. DOI: 10.3390/polym12010145.
- [55] L. Wang *et al.*, “Realizing ultrahigh transconductance in organic electrochemical transistor by co-doping pedot:pss with ionic liquid and dodecylbenzenesulfonate,” 2022. DOI: 10.1002/marc.202200212. [Online]. Available: <https://onlinelibrary.wiley.com/doi/10.1002/marc.202200212>.
- [56] D. Kiefer *et al.*, “Enhanced n-doping efficiency of a naphthalenediimide-based copolymer through polar side chains for organic thermoelectrics,” 2018. DOI: 10.1021/acseenergylett.7b01146. [Online]. Available: <https://pubs.acs.org/sharingguidelines>.
- [57] S. Kang, J. Fan, J. B. P. Soares, and M. Gupta, “Naphthalene diimide-based n-type small molecule organic mixed conductors for accumulation mode organic electrochemical transistors,” *RSC Advances*, vol. 13, pp. 5096–5106, 8 2023, ISSN: 2046-2069. DOI: 10.1039/D2RA07081B.
- [58] J. Fan, A. A. F. Pico, and M. Gupta, “A functionalization study of aerosol jet printed organic electrochemical transistors (oects) for glucose detection †,” vol. 2, p. 7445, 2021. DOI: 10.1039/d1ma00479d.
- [59] M. Pelgrom, H. Tuinhout, and M. Vertregt, “Transistor matching in analog cmos applications,” *IEEE*, 1998, pp. 915–918, ISBN: 0-7803-4774-9. DOI: 10.1109/IEDM.1998.746503. [Online]. Available: <http://ieeexplore.ieee.org/document/746503/>.

- [60] X. Chen *et al.*, “N-type rigid semiconducting polymers bearing oligo(ethylene glycol) side chains for high-performance organic electrochemical transistors,” *Angewandte Chemie International Edition*, vol. 60, pp. 9368–9373, 17 Apr. 2021, ISSN: 1433-7851. DOI: 10.1002/anie.202013998. [Online]. Available: <https://onlinelibrary.wiley.com/doi/10.1002/anie.202013998>.
- [61] Y.-D. Kim, D.-H. Lee, J.-U. Kim, and K. H.-K. Roh, “A simulation study on lot release control., mask scheduling, and batch scheduling in semiconductor wafer fabrication facilities,” *Journal of Manu/acturing Systems*, vol. 17, 2 1998.
- [62] H. S. White, G. P. Kittlesen, and M. S. Wrighton, “Chemical derivatization of an array of three gold microelectrodes with polypyrrole: Fabrication of a molecule-based transistor,” *Journal of the American Chemical Society*, vol. 106, pp. 5375–5377, 18 Sep. 1984, ISSN: 0002-7863. DOI: 10.1021/ja00330a070.
- [63] V. Venkatraman *et al.*, “Subthreshold operation of organic electrochemical transistors for biosignal amplification,” *Advanced Science*, vol. 5, 8 Aug. 2018, ISSN: 21983844. DOI: 10.1002/ADVS.201800453.
- [64] H. I. Kim *et al.*, “Improving the performance and stability of inverted planar flexible perovskite solar cells employing a novel ndi-based polymer as the electron transport layer,” 2018. DOI: 10.1002/aenm.201702872. [Online]. Available: <https://onlinelibrary.wiley.com/doi/10.1002/aenm.201702872>.
- [65] S. Rathinavel, K. Priyadharshini, and D. Panda, “A review on carbon nanotube: An overview of synthesis, properties, functionalization, characterization, and the application,” *Materials Science and Engineering: B*, vol. 268, p. 115095, Jun. 2021, ISSN: 09215107. DOI: 10.1016/j.mseb.2021.115095. [Online]. Available: <https://linkinghub.elsevier.com/retrieve/pii/S0921510721000556>.
- [66] W. Yang and G. Weng, “Electrical conductivity of carbon nanotube- and graphene-based nanocomposites,” in 2018, pp. 123–155.
- [67] A. R. Urade, I. Lahiri, and K. S. Suresh, “Graphene properties, synthesis and applications: A review,” *JOM*, vol. 75, pp. 614–630, 3 Mar. 2023, ISSN: 1047-4838. DOI: 10.1007/s11837-022-05505-8. [Online]. Available: <https://link.springer.com/10.1007/s11837-022-05505-8>.
- [68] L.-C. Qin, “Determination of the chiral indices (n,m) of carbon nanotubes by electron diffraction,” *Phys. Chem. Chem. Phys.*, vol. 9, pp. 31–48, 1 2007, ISSN: 1463-9076. DOI: 10.1039/B614121H. [Online]. Available: <http://xlink.rsc.org/?DOI=B614121H>.
- [69] K. Lonnecke, O. Eberhardt, and T. Wallmersperger, “Electrostatic charge distribution in armchair and zigzag carbon nanotubes: A numerical comparison of cnt charge models,” *Acta Mechanica*, vol. 234, pp. 1–16, 1 Jan. 2023, ISSN: 0001-5970. DOI: 10.1007/s00707-021-03085-3. [Online]. Available: <https://link.springer.com/10.1007/s00707-021-03085-3>.

- [70] H. He, L. A. Pham-Huy, P. Dramou, D. Xiao, P. Zuo, and C. Pham-Huy, “Carbon nanotubes: Applications in pharmacy and medicine,” *BioMed Research International*, vol. 2013, pp. 1–12, 2013, ISSN: 2314-6133. DOI: 10.1155/2013/578290.
- [71] M. delCarmen, O. Galao, F. J. Baeza, E. Zornoza, and P. Garcé, “Mechanical properties and durability of cnt cement composites,” *Materials*, vol. 7, pp. 1640–1651, 2014, ISSN: 1996-1944. DOI: 10.3390/ma7031640. [Online]. Available: [www.mdpi.com/journal/materialsArticle](http://www.mdpi.com/journal/materialsArticle).
- [72] K. Mylvaganam and L. C. C. Zhang, “Ballistic resistance capacity of carbon nanotubes,” *NANOTECHNOLOGY*, vol. 18, p. 4, 2007. DOI: 10.1088/0957-4484/18/47/475701.
- [73] P. Bondavalli, P. Legagneux, and D. Pribat, “Carbon nanotubes based transistors as gas sensors: State of the art and critical review,” *Sensors and Actuators B: Chemical*, vol. 140, pp. 304–318, 1 Jun. 2009, ISSN: 0925-4005. DOI: 10.1016/J.SNB.2009.04.025.
- [74] I. Dube *et al.*, “Understanding the electrical response and sensing mechanism of carbon-nanotube-based gas sensors,” *Carbon*, vol. 87, pp. 330–337, C Jun. 2015, ISSN: 0008-6223. DOI: 10.1016/J.CARBON.2015.01.060.
- [75] X. Wu *et al.*, “Fiber-shaped organic electrochemical transistors for biochemical detections with high sensitivity and stability,” vol. 63, pp. 1281–1288, 9 2020. DOI: 10.1007/s11426-020-9779-1. [Online]. Available: <https://doi.org/10.1007/s11426-020-9779-1>.
- [76] M. M. Shulaker *et al.*, “Three-dimensional integration of nanotechnologies for computing and data storage on a single chip,” *Nature*, vol. 547, pp. 74–78, 7661 Jul. 2017, ISSN: 0028-0836. DOI: 10.1038/nature22994. [Online]. Available: <https://www.nature.com/articles/nature22994>.
- [77] S. Forel, L. Sacco, A. Castan, I. Florea, and C. S. Cojocaru, “Simple and rapid gas sensing using a single-walled carbon nanotube field-effect transistor-based logic inverter,” *Nanoscale Advances*, vol. 3, pp. 1582–1587, 6 2021, ISSN: 2516-0230. DOI: 10.1039/D0NA00811G. [Online]. Available: <http://xlink.rsc.org/?DOI=D0NA00811G>.
- [78] P. Salvo *et al.*, “Temperature- and ph-sensitive wearable materials for monitoring foot ulcers,” *International Journal of Nanomedicine*, vol. Volume 12, pp. 949–954, Jan. 2017, ISSN: 1178-2013. DOI: 10.2147/IJN.S121726. [Online]. Available: <https://www.dovepress.com/temperature-and-ph-sensitive-wearable-materials-for-monitoring-foot-ul-peer-reviewed-article-IJN>.
- [79] Y. Song *et al.*, “Additively manufacturable micro-mechanical logic gates,” *Nature Communications*, vol. 10, p. 882, 1 Feb. 2019, ISSN: 2041-1723. DOI: 10.1038/s41467-019-08678-0.
- [80] M. Rhee and M. A. Burns, “Microfluidic pneumatic logic circuits and digital pneumatic microprocessors for integrated microfluidic systems †,” 2009. DOI: 10.1039/b904354c. [Online]. Available: [www.rsc.org/loc](http://www.rsc.org/loc).

- [81] C Monroe, D. M. Meekhof, B. E. King, W. M. Itano, and D. J. Wineland, "Demonstration of a fundamental quantum logic gate," vol. 75, p. 25, 1995.
- [82] Q. Xu, Y. Sun, P. Yang, and Y. Dan, "Density of defect states retrieved from the hysteretic gate transfer characteristics of monolayer mos2 field effect transistors," *AIP Advances*, vol. 9, p. 015 230, 1 Jan. 2019, ISSN: 2158-3226. DOI: 10.1063/1.5082829. [Online]. Available: <https://pubs.aip.org/aip/adv/article/1069676>.
- [83] Y. J. Jo, K. Y. Kwon, Z. U. Khan, X. Crispin, and T. I. Kim, "Gelatin hydrogel-based organic electrochemical transistors and their integrated logic circuits," *ACS Applied Materials and Interfaces*, vol. 10, pp. 39 083–39 090, 45 Nov. 2018, ISSN: 19448252. DOI: 10.1021/ACSAMI.8B11362.
- [84] C. Y. Yang *et al.*, "Low-power/high-gain flexible complementary circuits based on printed organic electrochemical transistors," *Advanced Electronic Materials*, vol. 8, 3 Mar. 2022, ISSN: 2199160X. DOI: 10.1002/AELM.202100907.
- [85] A. Makhinia, K. Hübscher, V. Beni, and P. A. Ersman, "High performance organic electrochemical transistors and logic circuits manufactured via a combination of screen and aerosol jet printing techniques," *Advanced Materials Technologies*, p. 2 200 153, May 2022, ISSN: 2365-709X. DOI: 10.1002/ADMT.202200153. [Online]. Available: <https://onlinelibrary.wiley.com/doi/10.1002/admt.202200153>.
- [86] M. Nishinaka *et al.*, "High-transconductance organic electrochemical transistor fabricated on ultrathin films using spray coating," *Small Structures*, vol. 2, p. 2 000 088, 3 Mar. 2021, ISSN: 2688-4062. DOI: 10.1002/sstr.202000088.
- [87] D. Majak, "Fully 3d printed organic electrochemical transistors for biosensing applications," MSc thesis, University of Alberta, Edmonton, Canada, 2019.
- [88] M. Yamashita and M. Agu, "Geometrical correction factor for semiconductor resistivity measurements by four-point probe method," *Japanese Journal of Applied Physics*, vol. 23, pp. 1499–1504, 11 Nov. 1984, ISSN: 13474065. DOI: 10.1143/JJAP.23.1499/XML. [Online]. Available: <https://iopscience.iop.org/article/10.1143/JJAP.23.1499https://iopscience.iop.org/article/10.1143/JJAP.23.1499/meta>.
- [89] M. Procop and V.-D. Hodoroaba, "Original paper x-ray fluorescence as an additional analytical method for a scanning electron microscope," *Microchim Acta*, vol. 161, pp. 413–419, 2008. DOI: 10.1007/s00604-007-0854-4.
- [90] Y. S. Zhang and A. Khademhosseini, "Advances in engineering hydrogels," *Science*, vol. 356, 6337 May 2017, ISSN: 10959203. DOI: 10.1126/SCIENCE.AAF3627/ASSET/FF981CF9-F818-45D8-A693-CA10D4ABEE12/ASSETS/GRAPHIC/356\_AAF3627\_F5.JPEG. [Online]. Available: <https://www.science.org/doi/10.1126/science.aaf3627>.
- [91] N. A. Peppas and A. S. Hoffman, "Hydrogels," in Elsevier, Jan. 2020, pp. 153–166. DOI: 10.1016/B978-0-12-816137-1.00014-3. [Online]. Available: <https://linkinghub.elsevier.com/retrieve/pii/B9780128161371000143>.

- [92] B. Salahuddin, S. Wang, D. Sangian, S. Aziz, and Q. Gu, “Hybrid gelatin hydrogels in nanomedicine applications,” *ACS Applied Bio Materials*, vol. 4, pp. 2886–2906, 4 Apr. 2021, ISSN: 2576-6422. DOI: 10.1021/acsabm.0c01630. [Online]. Available: <https://pubs.acs.org/doi/10.1021/acsabm.0c01630>.
- [93] J. Bae *et al.*, “Tailored hydrogels for biosensor applications,” *Journal of Industrial and Engineering Chemistry*, vol. 89, pp. 1–12, Sep. 2020, ISSN: 1226086X. DOI: 10.1016/j.jiec.2020.05.001. [Online]. Available: <https://linkinghub.elsevier.com/retrieve/pii/S1226086X20302033>.
- [94] J. Hu *et al.*, “Multifunctional hydrogel hybrid-gated organic photoelectrochemical transistor for biosensing,” pp. 2 109 046–2 109 047, 2022. DOI: 10.1002/adfm.202109046. [Online]. Available: <https://onlinelibrary.wiley.com/doi/10.1002/adfm.202109046>.
- [95] Z. Lou *et al.*, “Ultrasensitive and ultraflexible e-skins with dual functionalities for wearable electronics,” *Nano Energy*, vol. 38, pp. 28–35, Aug. 2017, ISSN: 22112855. DOI: 10.1016/j.nanoen.2017.05.024. [Online]. Available: <https://linkinghub.elsevier.com/retrieve/pii/S2211285517302975>.
- [96] S. Nakata, T. Arie, S. Akita, and K. Takei, “Wearable, flexible, and multifunctional healthcare device with an isfet chemical sensor for simultaneous sweat ph and skin temperature monitoring,” *ACS Sensors*, vol. 2, pp. 443–448, 3 Mar. 2017, ISSN: 2379-3694. DOI: 10.1021/acssensors.7b00047. [Online]. Available: <https://pubs.acs.org/doi/10.1021/acssensors.7b00047>.
- [97] Y. Che, H. Chen, H. Gui, J. Liu, B. Liu, and C. Zhou, “Review of carbon nanotube nanoelectronics and macroelectronics,” *Semiconductor Science and Technology*, vol. 29, p. 073 001, 7 Jul. 2014, ISSN: 0268-1242. DOI: 10.1088/0268-1242/29/7/073001. [Online]. Available: <https://iopscience.iop.org/article/10.1088/0268-1242/29/7/073001>.
- [98] B. Kumanek and D. Janas, “Thermal conductivity of carbon nanotube networks: A review,” *Journal of Materials Science*, vol. 54, pp. 7397–7427, 10 May 2019, ISSN: 0022-2461. DOI: 10.1007/s10853-019-03368-0. [Online]. Available: <http://link.springer.com/10.1007/s10853-019-03368-0>.
- [99] J.-P. Salvetat *et al.*, “Mechanical properties of carbon nanotubes,” *Appl. Phys. A*, vol. 69, pp. 255–260, 1999. DOI: 10.1007/s003399900114.
- [100] E. N. Ganesh, “Single walled and multi walled carbon nanotube structure, synthesis and applications,” *International Journal of Innovative Technology and Exploring Engineering (IJITEE)*, p. 311, 2 2013.
- [101] N. J. Blasdel, E. K. Wujcik, J. E. Carletta, K.-S. Lee, and C. N. Monty, “Fabric nanocomposite resistance temperature detector,” *IEEE Sensors Journal*, vol. 15, pp. 300–306, 1 Jan. 2015, ISSN: 1530-437X. DOI: 10.1109/JSEN.2014.2341915. [Online]. Available: <http://ieeexplore.ieee.org/document/6862867/>.

- [102] A. Giuliani, M. Placidi, F. D. Francesco, and A. Pucci, “A new polystyrene-based ionomer/mwcnt nanocomposite for wearable skin temperature sensors,” *Reactive and Functional Polymers*, vol. 76, pp. 57–62, 1 Mar. 2014, ISSN: 13815148. DOI: 10.1016/j.reactfunctpolym.2014.01.008. [Online]. Available: <https://linkinghub.elsevier.com/retrieve/pii/S1381514814000194>.
- [103] K. S. Karimov, M. T. S. Chani, and F. A. Khalid, “Carbon nanotubes film based temperature sensors,” *Physica E: Low-Dimensional Systems and Nanostructures*, vol. 43, pp. 1701–1703, 9 Jul. 2011, ISSN: 13869477. DOI: 10.1016/J.PHYSE.2011.05.025.
- [104] H. Ezgin, E. Demir, S. Acar, and M. Özer, “Investigation of temperature-dependent electrical parameters in a schottky barrier diode with multi-walled carbon nanotube (mwcnt) interface,” *Materials Science in Semiconductor Processing*, vol. 147, p. 106 672, Aug. 2022, ISSN: 13698001. DOI: 10.1016/j.mssp.2022.106672. [Online]. Available: <https://linkinghub.elsevier.com/retrieve/pii/S1369800122002153>.
- [105] Alamusi *et al.*, “Temperature-dependent piezoresistivity in an mwcnt/epoxy nanocomposite temperature sensor with ultrahigh performance,” *Nanotechnology*, vol. 24, p. 455 501, 45 Nov. 2013, ISSN: 0957-4484. DOI: 10.1088/0957-4484/24/45/455501. [Online]. Available: <https://iopscience.iop.org/article/10.1088/0957-4484/24/45/455501>.
- [106] S. Maiti, R. Bera, S. K. Karan, S. Paria, A. De, and B. B. Khatua, “Pvc bead assisted selective dispersion of mwcnt for designing efficient electromagnetic interference shielding pvc/mwcnt nanocomposite with very low percolation threshold,” *Composites Part B: Engineering*, vol. 167, pp. 377–386, Jun. 2019, ISSN: 13598368. DOI: 10.1016/j.compositesb.2019.03.012. [Online]. Available: <https://linkinghub.elsevier.com/retrieve/pii/S1359836818319607>.
- [107] M. Mohiuddin and S. Hoa, “Temperature dependent electrical conductivity of cnt–peek composites,” *Composites Science and Technology*, vol. 72, pp. 21–27, 1 Dec. 2011, ISSN: 02663538. DOI: 10.1016/j.compscitech.2011.08.018. [Online]. Available: <https://linkinghub.elsevier.com/retrieve/pii/S0266353811003083>.
- [108] C. A. S. deLima, L. G. Amurin, N. R. Demarquette, and E. David, “Morphological and electric properties of block copolymer/carbon nanotubes nanocomposites obtained by different methods,” *IEEE*, Jun. 2016, pp. 588–591, ISBN: 978-1-4673-8706-4. DOI: 10.1109/EIC.2016.7548671. [Online]. Available: <http://ieeexplore.ieee.org/document/7548671/>.
- [109] S. Kuester, G. M. Barra, J. C. Ferreira, B. G. Soares, and N. R. Demarquette, “Electromagnetic interference shielding and electrical properties of nanocomposites based on poly (styrene-b-ethylene-ran-butylene-b-styrene) and carbon nanotubes,” *European Polymer Journal*, vol. 77, pp. 43–53, Apr. 2016, ISSN: 00143057. DOI: 10.1016/J.EURPOLYMJ.2016.02.020.

- [110] G. L. Goh, S. Agarwala, and W. Y. Yeong, "Aerosol-jet-printed preferentially aligned carbon nanotube twin-lines for printed electronics," *ACS Applied Materials and Interfaces*, vol. 11, pp. 43 719–43 730, 46 Nov. 2019, ISSN: 1944-8244. DOI: 10.1021/acsami.9b15060. [Online]. Available: <https://pubs.acs.org/doi/10.1021/acsami.9b15060>.
- [111] S. Lu, J. Zheng, J. A. Cardenas, N. X. Williams, Y.-C. Lin, and A. D. Franklin, "Uniform and stable aerosol jet printing of carbon nanotube thin-film transistors by ink temperature control," *Cite This: ACS Appl. Mater. Interfaces*, vol. 12, p. 43 089, 2020. DOI: 10.1021/acsami.0c12046. [Online]. Available: <https://dx.doi.org/10.1021/acsami.0c12046>.
- [112] N. Calisi, P. Salvo, B. Melai, C. Paoletti, A. Pucci, and F. D. Francesco, "Effects of thermal annealing on sebs/mwcnts temperature-sensitive nanocomposites for the measurement of skin temperature," *Materials Chemistry and Physics*, vol. 186, pp. 456–461, Jan. 2017, ISSN: 02540584. DOI: 10.1016/j.matchemphys.2016.11.018. [Online]. Available: <https://linkinghub.elsevier.com/retrieve/pii/S025405841630829X>.
- [113] G. Matzeu, A. Pucci, S. Savi, M. Romanelli, and F. D. Francesco, "A temperature sensor based on a mwcnt/sebs nanocomposite," *Sensors and Actuators A: Physical*, vol. 178, pp. 94–99, May 2012, ISSN: 09244247. DOI: 10.1016/j.sna.2012.02.043. [Online]. Available: <https://linkinghub.elsevier.com/retrieve/pii/S0924424712001562>.
- [114] C. Guo *et al.*, "Mechanical and thermal properties of multiwalled carbon-nanotube-reinforced al<sub>2</sub>o<sub>3</sub> nanocomposites," *Ceramics International*, vol. 46, pp. 17 449–17 460, 11 Aug. 2020, ISSN: 02728842. DOI: 10.1016/j.ceramint.2020.04.039. [Online]. Available: <https://linkinghub.elsevier.com/retrieve/pii/S0272884220309834>.
- [115] M. Kaseem, K. Hamad, and Y. G. Ko, "Fabrication and materials properties of polystyrene/carbon nanotube (ps/cnt) composites: A review," *European Polymer Journal*, vol. 79, pp. 36–62, Jun. 2016, ISSN: 00143057. DOI: 10.1016/j.eurpolymj.2016.04.011. [Online]. Available: <https://linkinghub.elsevier.com/retrieve/pii/S0014305716302518>.
- [116] N. Calisi *et al.*, "Factors affecting the dispersion of mwcnts in electrically conducting sebs nanocomposites," *European Polymer Journal*, vol. 49, pp. 1471–1478, 6 Jun. 2013, ISSN: 00143057. DOI: 10.1016/j.eurpolymj.2013.03.029. [Online]. Available: <https://linkinghub.elsevier.com/retrieve/pii/S0014305713001614>.
- [117] D. Mohanta, S. Patnaik, S. Sood, and N. Das, "Carbon nanotubes: Evaluation of toxicity at biointerfaces," *Journal of Pharmaceutical Analysis*, vol. 9, pp. 293–300, 5 Oct. 2019, ISSN: 20951779. DOI: 10.1016/j.jpha.2019.04.003. [Online]. Available: <https://linkinghub.elsevier.com/retrieve/pii/S2095177918305458>.

- [118] Y. Liu, Y. Zhao, B. Sun, and C. Chen, “Understanding the toxicity of carbon nanotubes,” *Accounts of Chemical Research*, vol. 46, pp. 702–713, 3 Mar. 2013, ISSN: 0001-4842. DOI: 10.1021/ar300028m. [Online]. Available: <https://pubs.acs.org/doi/10.1021/ar300028m>.
- [119] J. Dong and Q. Ma, “Advances in mechanisms and signaling pathways of carbon nanotube toxicity,” *Nanotoxicology*, vol. 9, pp. 658–676, 5 Jul. 2015, ISSN: 1743-5390. DOI: 10.3109/17435390.2015.1009187. [Online]. Available: <http://www.tandfonline.com/doi/full/10.3109/17435390.2015.1009187>.
- [120] R. Hayakawa, K. Honma, S. Nakaharai, K. Kanai, and Y. Wakayama, “Electrically reconfigurable organic logic gates: A promising perspective on a dual-gate antiambipolar transistor,” *Advanced Materials*, vol. 34, p. 2109491, 15 Apr. 2022, ISSN: 0935-9648. DOI: 10.1002/adma.202109491. [Online]. Available: <https://onlinelibrary.wiley.com/doi/10.1002/adma.202109491>.
- [121] J. C. Ribierre *et al.*, “Direct laser writing of complementary logic gates and lateral p-n diodes in a solution-processible monolithic organic semiconductor,” *Advanced Materials*, vol. 22, pp. 1722–1726, 15 Apr. 2010, ISSN: 09359648. DOI: 10.1002/adma.200903152. [Online]. Available: <https://onlinelibrary.wiley.com/doi/10.1002/adma.200903152>.
- [122] M. Hamsch, K. Reuter, H. Kempa, and A. Hübler, “Comparison of fully printed unipolar and complementary organic logic gates,” *Organic Electronics*, vol. 13, pp. 1989–1995, 10 Oct. 2012, ISSN: 15661199. DOI: 10.1016/j.orgel.2012.05.045. [Online]. Available: <https://linkinghub.elsevier.com/retrieve/pii/S1566119912002443>.
- [123] I. C. Kwak *et al.*, “Solid-state homojunction electrochemical transistors and logic gates on plastic,” *Advanced Functional Materials*, vol. 33, p. 2211740, 13 Mar. 2023, ISSN: 1616-301X. DOI: 10.1002/adfm.202211740. [Online]. Available: <https://onlinelibrary.wiley.com/doi/10.1002/adfm.202211740>.
- [124] A. Markova, S. Stržiteský, M. Weiter, and M. Vala, “Serial resistance effect on organic electrochemical transistors’ transconductance,” *IEEE Sensors Journal*, pp. 1–1, 2023, ISSN: 1530-437X. DOI: 10.1109/JSEN.2023.3296939. [Online]. Available: <https://ieeexplore.ieee.org/document/10192544/>.
- [125] Y. Fang *et al.*, “Coaxial fiber organic electrochemical transistor with high transconductance,” *Nano Research*, Apr. 2023, ISSN: 1998-0124. DOI: 10.1007/s12274-023-5722-y. [Online]. Available: <https://link.springer.com/10.1007/s12274-023-5722-y>.
- [126] D. A. Koutsouras, F. Torricelli, and P. W. Blom, “Submicron vertical channel organic electrochemical transistors with ultrahigh transconductance,” *Advanced Electronic Materials*, vol. 9, 2 Feb. 2023, ISSN: 2199-160X. DOI: 10.1002/aelm.202200868. [Online]. Available: <https://onlinelibrary.wiley.com/doi/10.1002/aelm.202200868>.

- [127] P. Dwivedi, R. Singh, and Y. S. Chauhan, "Crossing the nernst limit (59 mv/ph) of sensitivity through tunneling transistor-based biosensor," *IEEE Sensors Journal*, vol. 21, pp. 3233–3240, 3 Feb. 2021, ISSN: 1530-437X. DOI: 10.1109/JSEN.2020.3025975. [Online]. Available: <https://ieeexplore.ieee.org/document/9203890/>.
- [128] Z. Ni *et al.*, "Ambipolar conjugated polymers with ultrahigh balanced hole and electron mobility for printed organic complementary logic via a two-step c-h activation strategy," *Advanced Materials*, vol. 31, p. 1806010, 10 Mar. 2019, ISSN: 09359648. DOI: 10.1002/adma.201806010. [Online]. Available: <https://onlinelibrary.wiley.com/doi/10.1002/adma.201806010>.
- [129] J. Kwon, H. Matsui, W. Kim, S. Tokito, and S. Jung, "Static and dynamic response comparison of printed, single- and dual-gate 3-d complementary organic tft inverters," *IEEE Electron Device Letters*, vol. 40, pp. 1277–1280, 8 Aug. 2019, ISSN: 0741-3106. DOI: 10.1109/LED.2019.2922296. [Online]. Available: <https://ieeexplore.ieee.org/document/8736018/>.
- [130] G. Casula, S. Lai, L. Matino, F. Santoro, A. Bonfiglio, and P. Cosseddu, "Printed, low-voltage, all-organic transistors and complementary circuits on paper substrate," *Advanced Electronic Materials*, vol. 6, p. 1901027, 5 May 2020, ISSN: 2199-160X. DOI: 10.1002/aelm.201901027. [Online]. Available: <https://onlinelibrary.wiley.com/doi/10.1002/aelm.201901027>.
- [131] H. Yoo *et al.*, "Reconfigurable complementary logic circuits with ambipolar organic transistors open," *Nature Publishing Group*, 2016. DOI: 10.1038/srep35585. [Online]. Available: [www.nature.com/scientificreports](http://www.nature.com/scientificreports).
- [132] W. Huang *et al.*, "Vertical organic electrochemical transistors for complementary circuits," *Nature*, vol. 613, pp. 496–502, 7944 Jan. 2023, ISSN: 0028-0836. DOI: 10.1038/s41586-022-05592-2. [Online]. Available: <https://www.nature.com/articles/s41586-022-05592-2>.
- [133] J. Fan, S. S. Rezaie, M. Facchini-Rakovich, D. Gudi, C. Montemagno, and M. Gupta, "Tuning pedot:pss conductivity to obtain complementary organic electrochemical transistor," *Organic Electronics*, vol. 66, pp. 148–155, Mar. 2019, ISSN: 15661199. DOI: 10.1016/j.orgel.2018.12.013.

# Appendix A: Recipes and Procedures

## A.1 Nanocomposite Recipe and Preparation Procedure

1) Dissolve 0.5g SEBS (Sigma-Aldrich 200565-250G) in 100 mL of toluene in large jar.

2) Measure out 4 mg of CNT powder and place into clean vial.

3) Pipette 12 mL of toluene-SEBS solution out of jar and put into CNT powder vial. This yields a 15:1 ratio. To edit ratio, measure out a different amount of CNT rather than SEBS.

4) Sonicate for 60 minutes at full power - 110W/40 kHz.

5) Pour solution into 2, 1.5 mL eppendorf tubes (the centrifuge must be balanced). Centrifuge at 4000 rpm for 30 minutes.

6) Immediately drop centrifuged solution onto printed device. For a well size of 36 mm<sup>2</sup>, 6  $\mu$ L works best. When extracting, pipette from the top or middle of the tube as the agglomerates are found at the bottom.

7) Whenever creating a new device it is always best to repeat this procedure as reagglomeration can occur. The most time consuming part of the process is the sonication/centrifugation which must be done anyway when creating a new dispersion, thus is it best to just start over again.

## A.2 PEDOT:PSS Ink Recipe and Preparation Procedure

1) Preparation: retrieve 25 mL Erlenmeyer flask, aluminum foil, and stir bar. Cover flask with aluminum and drop stir bar. Clamp flask to the middle of the hot plate/stir station. Cover the top of the flask with parafilm.

2) Connect a 20G needle to a nitrogen source and turn the flow to a minimum. Verify flow of nitrogen by placing needle tip above a container filled with water.

3) Clamp the needle near the Erlenmeyer flask and penetrate the parafilm to set the conditions for an inert N<sub>2</sub> environment.

4) Extract GOPS using the balloon method - fill balloon/syringe contraption with nitrogen 3 times, then attach needle to it (23G) and puncture the seal. Using another needle connected to a ~ 1 mL syringe, draw 0.1 mL and put into a small eppendorf tube.

5) Gather the ingredients PEDOT:PSS (Clevios PH-1000), ethylene glycol (Sigma Aldrich), DBSA (Sigma Aldrich), and GOPS (Sigma Aldrich). The exact amounts depend on the recipe and are outlined in the table below. Turn on the stir at 350 rpm.

6) Draw each ingredient using a pipette and drop them into the vial after slightly lifting parafilm wrapping. When dropping, ensure that ingredient doesn't catch on the walls of the flask, especially for ingredients with quantities in the  $\mu\text{L}$  range.

7) When all ingredients are added, remove N<sub>2</sub> needle from the vial and replace parafilm covering with a fresh one.

8) Switch stir to 700 rpm and wait 20 minutes.

9) Transfer solution to a clean vial and sonicate for 30 minutes. If PEDOT:PSS solution is older than 1 month, sonicate for 1 hour.

10) Use a large nylon filter (1.5  $\mu\text{m}$ ) and syringe to filter the solution into a new clean vial.

11) Use a second smaller nylon filter ( $0.45\ \mu\text{m}$ ) and syringe to filter the solution into a new clean vial.

12) Transfer 1.5 mL of this solution to the aerosol jet printing vial. This can be directly printed.

13) Clean all vials and wrap remaining solution vial in aluminum foil. Store in  $4^{\circ}\text{C}$ .

Table A.1: Ingredient ratios for the two recipes A and B found in chapters 4 and 5, respectively. Recipe A results in a PEDOT:PSS film with a higher conductivity while recipe B results in a film with lower conductivity.

Recipe	Ingredient			
	PEDOT:PSS	Ethylene Glycol	DBSA	GOPS
Recipe A	5 mL	1.25 mL	$12.5\ \mu\text{L}$	$60\ \mu\text{L}$
Recipe B	5 mL	0.265 mL	$5\ \mu\text{L}$	$50\ \mu\text{L}$

### A.3 gNDI-Br<sub>2</sub> Ink Recipe and Preparation Procedure

1) Prepare a small 1.5 mL eppendorf tube. Fill it with 75 mg of synthesized NDI compound taken from the flask under vacuum. Weigh it directly in the eppendorf tube.

2) Gather ingredients: oxylene (Sigma Aldrich) and chloroform (Sigma Aldrich).

3) Extract 0.15 mL of chloroform using the balloon method outlined in A.2.

4) Pour 1.35 mL of oxylene and 0.15 mL of chloroform into the eppendorf tube containing NDI. This results in an oxylene to chloroform ratio of 9:1, which can be edited, but this is the most optimized ratio as of right now. Mix well.

5) Sonicate the mixture for 30 minutes.

6) The resulting 1.5 mL of ink can be directly poured into the aerosol jet printing vial.

7) Any remaining ink can be poured back into the flask under vacuum containing the synthesized NDI compound. The vacuum will evaporate the oxylene/chloroform and the compound should be dry enough to repeat the procedure if necessary after  $\sim$  2-3 days.

## A.4 GOx Functionalization Procedure

1) Preparation: Dissolve 1 w/v% CHIT solution (Sigma Aldrich, low molecular weight) in 1 v/v% acetic acid (Sigma Aldrich). Heat solution on hot plate at 60°C overnight, and store at 4°C. Also prepare 5 w/v% gelatin B (Sigma Aldrich) to PBS hydrogel and mix in the same fashion.

2) Mix GOx (Sigma Aldrich, from aspergillus niger) with 1xPBS solution in a concentration of 50 mg/mL in a small eppendorf tube. Sonicate for 10 minutes to fully dissolve.

3) Mix the GOx solution with CHIT solution at a 1:1 ratio to achieve a final concentration of 25 mg/mL.

4) Wrap the solution in aluminum foil and store overnight at 4°C.

5) First day of functionalization: drop cast 7  $\mu$ L of the GOx solution onto the 3mm x 3mm gate area. Do not allow any spread to the channel to avoid performance deterioration. Store device at 4°C overnight.

6) Second day of functionalization: drop cast 0.5  $\mu$ L of Nafion solution (Sigma Aldrich, 2.5%) on the functionalized area. Store the device at 4°C overnight.

7) Third day of functionalization: retrieve, reheat and stir the gelatin B hydrogel. Prepare eppendorf tube with gluteraldehyde (Sigma Aldrich, grade II), and prepare to drop gelatin B hydrogel into the tube to create a 1% gluteraldehyde mixture. Since cross linking happens within approximately 20 seconds, gelatin B must be mixed and immediately pipetted to be dropped onto the gate area. 4  $\mu$ L of hydrogel cross linked with GA to cover the gate area. The remaining hydrogel in the tube at this point is likely cross-linked - multiple devices will require multiple mixtures, or inhumanly fast

reflexes. Store devices at 4°C overnight.

8) Fourth day of functionalization: retrieve the devices and stick them to a piece of gel-pack. Stick the gel-pack to the bottom of a small petri dish. Fill the dish with PBS until the devices are fully covered. Store the devices at 4°C overnight.

9) Fifth day: the devices are ready to be tested. Take them out of the solution and wash them with DI water. Once tested, sink them in PBS solution and store them at 4°C until they are to be tested again. These devices can keep for approximately 3 weeks.

## A.5 Short Channel Printing Procedure

1) Preparation: firstly and most importantly, ensure there is exactly 1.5 mL of gold nanoparticle ink (UTDOTS, UTDAu40 TE) in the printing vial. Small amounts over or under this number result in unpredictable printing which complicates the procedure in step 5.

2) Printing design: ensure that the channel is being printed parallel to the width parameter of the channel, as shown in Figure A.1.

3) Design a short channel in the AutoCad program. The smallest channel length printed in this work resulted from a designed channel length of 60  $\mu\text{m}$ , which resulted in a final designed length of 50  $\mu\text{m}$  when the infill function was applied (with an infill of 10  $\mu\text{m}$ , optimized for the gold ink). This resulted in an actual channel length with a minimum feature size of 22  $\mu\text{m}$ , as shown in Figure 5.2 (c) in Chapter 5. With careful optimization, this may be shrunk further, as the advertised minimum feature size of the Optomec Aerosol Jet 5X 3D printer is allegedly 10  $\mu\text{m}$ .

4) When printing the design, make sure the first features printed are the two squares that make up the channel. This ensures a level of control of printing the ink at a certain wetness as outlined in step 5. To do this, fill in these squares first when using the infill function in AutoCad. This ensures the program will put these features first in the order of printing in the final script.

5) Before clicking "Run" after loading the printing file, ensure that the gold deposition is at the "sweet spot" between non-continuous and wet. This means that the line has just started to continuously print, but has not gotten too wet yet (i.e, when the line becomes very dark). This is the most difficult step and may take multiple attempts to perfect. It is recommended to also print the test lines on a throw-away substrate that is very close to the side of the substrate where the electrodes are to be printed. This minimizes the time between clicking "Run" and the printing of the electrodes, ensuring the deposition does not get too wet before then.

6) Clean the deposition tube between each print. This ensures consistent results when the process is restarted from step 5.

7) When printing is done, do not add more ink to the vial than absolutely necessary. Only add ink to the vial when the deposition becomes noticeably sparse. Too much ink in the vial complicates the procedure in step 5.

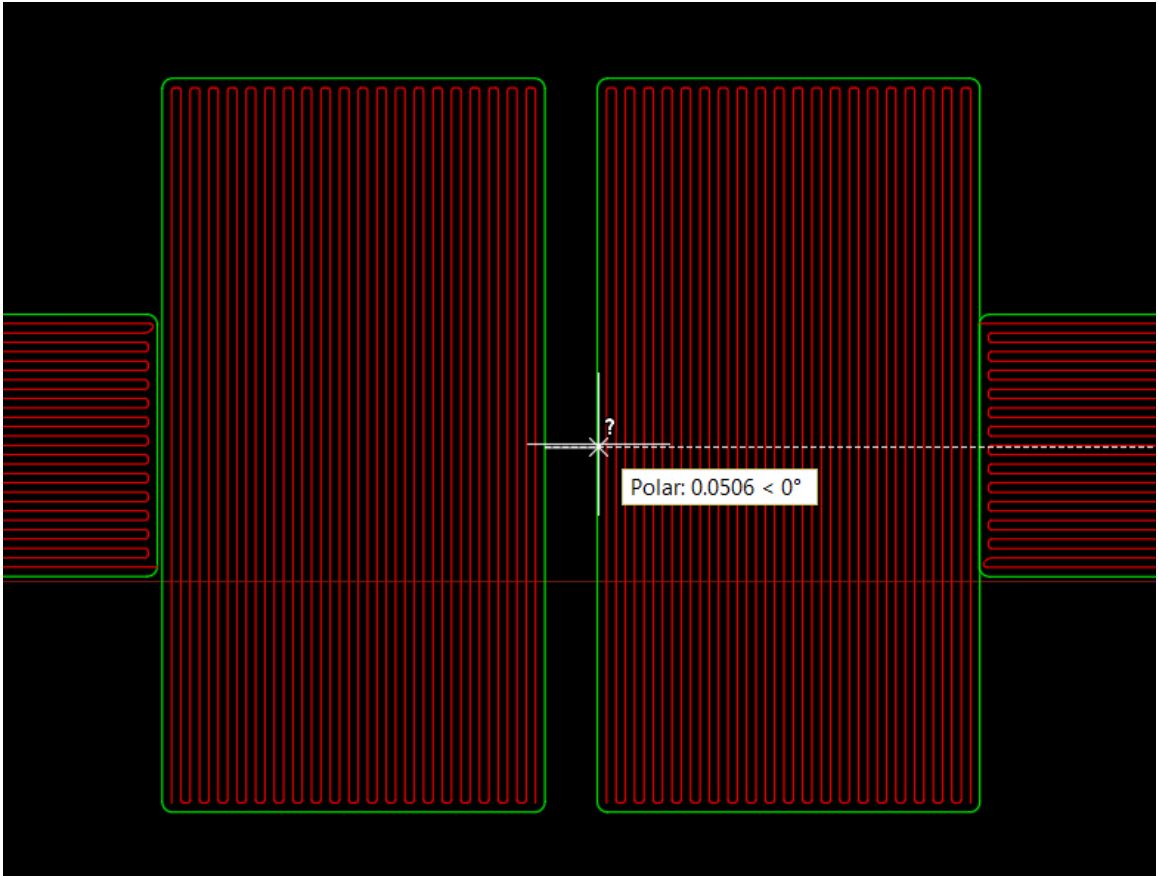


Figure A.1: Printing design for a channel with gold electrodes. The design has resulted in a printed channel with minimum feature size of  $22\ \mu\text{m}$ . The channel length measured in the middle indicates  $50\ \mu\text{m}$ .

# Appendix B: Ink Characterization

## B.1 PEDOT:PSS Ink Characterization

Table B.1: The relationship between number of printed layers, thickness, and resistance of printed PEDOT:PSS films.

Number of layers	Average thickness (nm)	Sheet Resistance ( $\Omega/\text{sq}$ )	Resistivity ( $\Omega\text{-cm}$ )
2	263.5	785.65	0.207
4	523.75	507.36	0.0266
6	739.75	343.32	0.0254
8	1011.25	384.37	0.0389
10	1237.5	324.93	0.0402

## B.2 Polyimide Ink Characterization

Table B.2: The relationship between printed layers and thickness of polyimide films.

Number of layers	Average thickness ( $\mu\text{m}$ )
4	1.38
8	2.83
12	4.82
16	6.76

Table B.3: Optimized parameters for polyimide ink printing.

Parameter	Value
Sheath Flow (ccm)	60
Atomizer Flow (ccm)	27
Bath Temperature (degC)	25
Platen Temperature (degC)	45
Bubbler	NO
Max atomizer current (A)	0.45
Line Speed (mm/s)	5
Tip size ( $\mu\text{m}$ )	200
Line Spacing ( $\mu\text{m}$ )	30
Curing Temperature (degC)	130
Curing Time (minutes)	90

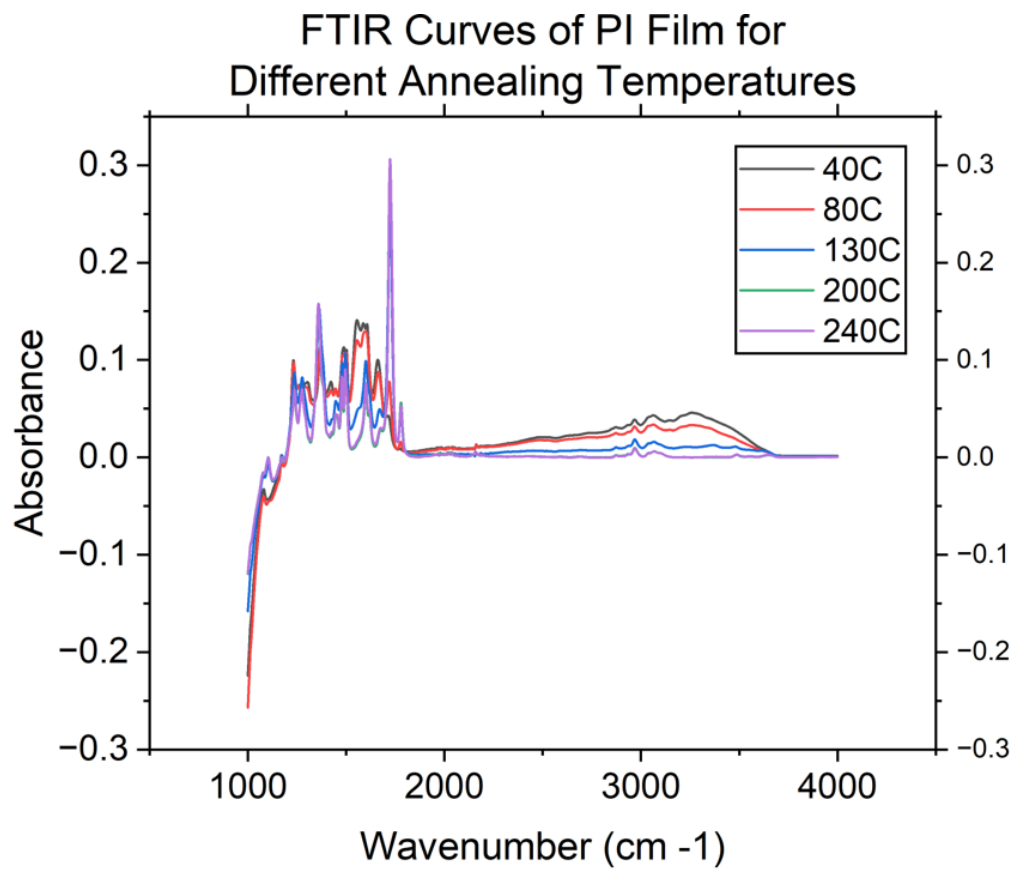


Figure B.1: FTIR curves of printed polyimide films after annealing at various temperatures for 1 hour and 30 minutes.

# Appendix C: Ion-Selective Membrane

An ion-selective membrane (ISM) was also developed and dropped as part of the work in Chapter 4, but was unsuccessful in terms of performance. An ion-selective membrane is meant to be permeable only to ions of a certain composition. The recipes, procedure and results are shown in this Appendix.

## C.1 Recipes and Procedure

1) Gather the ingredients: Na ionophore X (Sigma Aldrich, selectophore grade), lipophilic salt sodium tetrakis[3,5-bis(trifluoromethyl)phenyl] borate (Na-TFPB) (Sigma Aldrich, selectophore grade), polyvinyl chloride (Sigma Aldrich, selectophore grade), and bis(2-ethylehexyl) sebacate (BEHS) (Sigma Aldrich, selectophore grade).

2) Mix the ingredients in the desired ratio (attempted weights are outlined in Table C.1) in a clean vial. Dissolve all ingredients with a stir bar at 7000 rpm for 20 minutes in 660  $\mu\text{L}$  of tetrahydrofuran (THF). Do not vortex mix in an eppendorf tube as this does not lead to effective dissolution of components.

3) Drop 0.25  $\mu\text{L}$  of membrane solution over the channel material. It is recommended to print a polyimide well around the channel to contain the drop-cast.

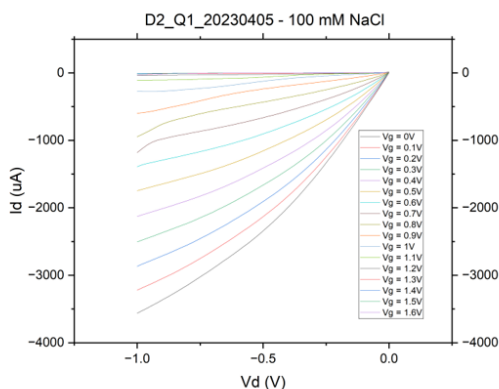
4) Store the device at room temperature overnight.

Table C.1: The multiple recipes attempted for the development of an ion-selective membrane.

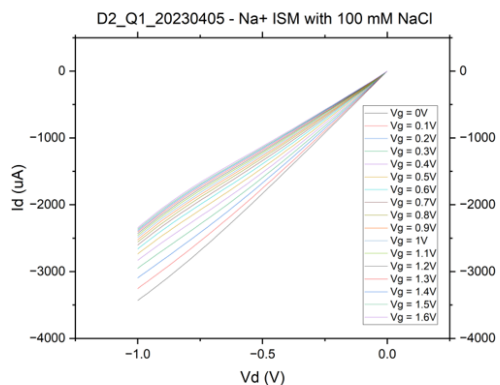
Recipe	Ingredient (% w/w)			
	Na Ionophore X	Na-TFPB	PVC	BEHS
A	1	0.55	33	65.45
B	10	0.55	24	65.45
B	10	5	20	65

## C.2 Results

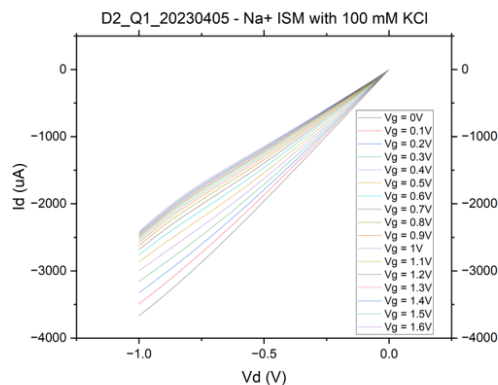
The curves in Figure C.1 show the performance of OECT devices in the form of  $I_D$ - $V_D$  curves before and after dropping of the ion-selective membrane (Recipe B). All recipes followed this same trend. The performance was slightly degraded as shown in Figure C.1 (b). When testing with NaCl before dropping, the OECT functions as expected. After the dropping of the membrane, the performance when dropping NaCl once again is degraded but the current levels are still affected by the gate voltage. This is likely due to the impermeability of the membrane due to the inclusion of PVC. However, when dropping KCl, the curves are roughly the same, indicating no selectivity towards Na<sup>+</sup> ions.



(a)



(b)



(c)

Figure C.1: (a)  $I_D$ - $V_D$  curves of a regular OECT with NaCl dropped on its channel. (b)  $I_D$ - $V_D$  curves of the same OECT with an Na<sup>+</sup> ISM dropped over its channel, with NaCl as the electrolyte. (c)  $I_D$ - $V_D$  curves of the same OECT with an ISM dropped over its channel, with KCl as the electrolyte.